UNIVERSITEIT VAN PRETORIA
UNIVERSITY OF PRETORIA
YUNIBESITHI YA PRETORIA
Denkleiers • Leading Minds • Dikgopolo tša Dihlalefi

UNIVERSITEIT VAN PRETORIA
UNIVERSITY OF PRETORIA
YUNIBESITHI YA PRETORIA
Denkleiers • Leading Minds • Dikgopolo tša Dihlalefi

RECOVERY AND SYNTHESIS OF POLYCATIONIC DIMETALS FROM ACID MINE DRAINAGE AND THEIR RESPECTIVE APPLICATION IN THE REMOVAL OF ARSENIC, CHROMIUM AND CONGO RED DYE FROM TOXIC INDUSTRIAL EFFLUENTS

By

KHATHUTSHELO LILITH MUEDI

A dissertation submitted in partial fulfilment of the requirements for the degree of

MASTER OF SCIENCE: APPLIED SCIENCE (ENVIRONMENTAL TECHNOLOGY)

Supervisor : Dr Hendrik Gideon Brink

Co-Supervisors : Dr Vhahangwele Masindi

Prof Johannes Phillipus Maree

Department of Chemical Engineering

School of Engineering

Faculty of Engineering, Built Environment and Information Technology

University of Pretoria

Pretoria

April 2020

Declaration

I, **KHATHUTSHELO LILITH MUEDI**, hereby declare that the work provided in this dissertation is to the best of my knowledge original (except where cited) has never been submitted for another degree at this or any other tertiary education institution.

Signature of candidate: 

This 05 day of FEBRUARY 2020

Dedication

I dedicate this Master's research project to my dearest late father, **Mr. Nyelisani Freddy Muedi**, and lovely beautiful mother, **Mrs. Thivhulawi Bernies Muedi** for having been my pillars of strength throughout my journey. You are the sweethearts of my heart.

Acknowledgements

First and foremost, I give thanks, glory and honour to Jehovah God for the life, grace, wisdom and mercy He has always granted me. To God be the glory. Now and Always.

I would like to express profound gratitude and sincere thanks to my supervisors **Dr. Hendrik Gideon Brink, Dr. Vhahangwele Masindi** and **Prof. Johannes Phillipus Maree** for their guidance, facilitation, supervision and most assistance through-out this project.

I would also like to give special thanks to **Ms Alette Devega** for the profound laboratory assistance.

I would also like to express my appreciation and thanks to the **Council of Industrial Research (CSIR)** and **Tshwane University of Technology (TUT)** for providing me with their laboratory spaces, equipment and sample analysis.

I also wish to extend my gratitude to my dearest siblings: **Livhuwani Tancred Muedi, Phathutshedzo Gareth Muedi, Edzani Elspeth Muedi** and **Murendeni Nkhangweleni Ivy Muedi** for giving me all forms of support to ensure this project becomes a success. I wouldn't have done it without you.

I also wish to convey my gratitude to my friends, research mates and colleagues for always giving me support and courage.

Lastly, I would to convey my profound gratitude and thanks to the **National Research Foundation (NRF)** South Africa for funding this project through the Innovation Masters Scholarship [grant ID number SFH160713177910], and **Department of Environment, Forestry and Fisheries (DEFF)** for providing financial support for this study.

Publications and Conference Proceedings

Journal Publications:

1. Masindi, V., Akinwekomi, V., Maree, J. P., & Muedi, K. L. (2017). Comparison of mine water neutralisation efficiencies of different alkaline generating agents. *Journal of Environmental Chemical Engineering*, 5(4), 3903-3913.

Conference Proceedings:

1. K. L. Muedi, H. G. Brink, V. Masindi & J. P. Maree. Removal of As(V) from aqueous solution using Poly-cationic/Di-metal/nano-composite recovered and synthesized from authentic acid mine drainage treatment process. *Chemical waste management.* Proceedings of the Fifth International Symposium on Green Chemistry, Sustainable Development and Circular Economy, 30 September – 03 October 2018, Skiathos Island, Greece.

2. Khathutshelo L. Muedi; Hendrik G. Brink; Vhahangwele Masindi; Johannes P. Maree Recovery and Synthesis of Al3+/Fe3+ Polycationic-Nanocomposites from Acid Mine Drainage Treatment Process and their Respective Application in the Removal of Arsenic and Chromium Ions from Polluted Water Resources. 11th ICARD International Mine Water Association (IMWA) Annual Conference, 10 September – 14 September 2018. Theme: “Risk to opportunity”, Pretoria South Africa.

3. Muedi, K.L.; Brink, H.G.; Masindi, V.; Maree, J.P. Recovery of Poly-cationic di-metal nanocomposite from natural acid mine drainage and respective application in As(V) removal. Poster presentation. Water Institute of Southern Africa (WISA) Biennial Conference and Exhibition, 24 June 2018 – 27 June 2018. Theme: “Breaking Boundaries, Connecting Ideas”, Cape Town, South Africa.

Table of Contents

List of Figures

List of Tables

Abstract

Title: Recovery of Fe-polymeric species from acid mine drainage and their respective applications in the removal of pollutants from wastewaters

Author: Khathutshelo Lilith Muedi

Supervisor: Dr Hendrik Gideon Brink (University of Pretoria)

Co – Supervisor: Dr Vhahangwele Masindi (Magalies Water)

Co – Supervisor: Prof Johannes Philippus Maree (ROC Water Technologies)

Water contamination is one of the leading challenges faced by the global community. This is due to the escalating population growth and anthropogenic activities which have led to water supply being inversely proportional to demand for fresh water. In this study, the recovery of Fe-polymeric species from authentic acid mine drainage and their respective applications in the removal of pollutants from wastewaters were explored. The synthesis of polycationic dimetal iron/aluminium nanocomposite (PDFe/Al nanocomposite) was executed through fractional precipitation followed by and processed through calcination and vibratory ball milling, while the efficiency of the material was determined through adsorption of arsenic (As(V)), chromium (Cr(VI)) and Congo red dye (CR) on a batch experimental set-up. Parameters optimised included: agitation time, adsorbent dosage, temperature, pH, and initial adsorbate concentration. Experimental results revealed that optimum conditions that are suitable for the removal of As(V) from an aqueous system are: 150 mg/L of As(V) concentration, 1 g adsorbent and 60 min equilibration time. As(V) removal was independent of pH and temperature. Cr(VI) was effectively removed at 50 mg/L initial Cr(VI) concentration, 3 g nanocomposite dosage, initial pH = 3 of solution, 180 min equilibration time and temperature = 45 ºC. Optimum conditions for removal for CR adsorption are: 100 mg/L initial CR concentration; 0.5 g PDFe/Al nanocomposite; 20 minutes agitation time; 3 – 8 initial CR pH; and temperature of 35 ºC. Under optimised conditions, As(V), Cr(VI) and CR showed >99,9%, >95% and >99%, respectively. The adsorption capacities (q_e) of As(V), Cr(VI) and CR were found to be 105 mg/g, 4.166 mg/g and 25 mg/g, respectively. Adsorption kinetics followed the pseudo-second-order as opposed to pseudo-first-order behaviour, therefore confirming chemisorption for all chemical species. Regeneration study of the material showed that the adsorbent can be reused more than four times

on the adsorption of As(V), Cr(VI) and CR. This study demonstrated that valorisation of waste material by recovering valuable di-metals and employing them to curtail the impact of problematic pollutants is feasible. As such, this double-edged study demonstrated the exceptional potential of the synthesised material to remove As(V), Cr(VI) and CR from aqueous system.

Key words: Acid mine drainage; Poly-cationic Di-metal Fe/Al nanocomposite Arsenic; Chromium; Congo Red dye; Precipitation; Adsorption; Kinetics; Regeneration

CHAPTER ONE

INTRODUCTION

1.0 Introduction

This chapter will introduce the background information, problem statement, aim and objectives of research study, hypothesis, research rationale, and the structure of the thesis.

1.1 Background Information

Water pollution is defined as the direct or indirect change in the physical, chemical or biological state of water which in turn makes it potentially harmful to human health, organisms and the environment at large, as well as making it less fit for any beneficial purpose (Act No 36 of 1998). Water quality, on the other hand, as defined in the National Water Act (Act 36 of 1998), refers to the physical, chemical, biological and radiological characteristics of the water. Such characteristics aid in determining the water's condition relative to one or many purposes it is required for, such as consumption or for the environment (Act No 36 of 1998, Diersing, 2009, Khatri and Tyagi, 2015). Although it can be stated that no water is actually pure nor clean due to the presence of few concentrations of gases and minerals, as well as quantities of life, anthropogenic activities, however, have been reported to be the most common sources of water pollution as compared to natural sources (Goel, 2006). Activities such as mining, power generation, industrialisation, material production in factories and agricultural production are some of the anthropogenic activities which have been noted to pose significant impacts on the quality and quantity of surface and ground water resources (Khatri and Tyagi, 2015).

The economy of South Africa is backed by, amongst others, mining and industrialisation. Despite the benefits from the sectors, they have been noted to impose devastating impacts to the environment and its sustainability. Mining introduces heavy metals which then impact on human health, aquatic organisms and the environment as a whole, of which the major environmental implication is the formation of acid mine drainage. Arsenic, chromium and dyes are pollutants, amongst others, are important species for different industrial uses. Arsenic is important for wood

preservation and insecticides production; while chromium is crucial in steel and alloy production and pigmentation. Congo red dye is mostly used in textile industries for impartation of colour on materials, as well as testing of amyloidosis (Sasmal et al., 2017, Ziane et al., 2018, Henke, 2009, Lepora, 2005). While these species have outstanding benefits, they however pose high-level risk to human health and the environment as a whole; hence regarded as prime pollutants. The discharge of arsenic, chromium and Congo red dye to the waterways leads to serious environmental impacts which in turn affect aquatic life and other living organisms on secondary and tertiary exposure. Moreover, these pollutants also alter the chemistry of the environment when they enter the various compartments as they are difficult to degrade (Mahmoud et al., 2018). Impacts can vary from health to environmental related, such as reduction of the physiological metabolism, mortality, cancer, mutations and bioaccumulation (Ratnaike, 2003, Shahid et al., 2017, Singh and Kalamdhad, 2011).

The escalating world population has resulted in a higher demand for freshwater than the supply thereof to society (DWF, 2004). This continuous population growth continues to mount pressure on researchers, scientists, and other affected parties to find sustainable methods to protect and conserve limited water resources for the benefits of current and future generations. As a result of very high demand for clean water and severe environmental impacts caused by arsenic, chromium and Congo red dye impairs their suitability for use.

Arsenic is a naturally-occurring metalloid with high toxicity and oxidation states of -3 (arsine), 0 (arsenic), +3 (arsenite) and +5 (arsenate), of which the prime states are +3 and +5 (Nazari et al., 2017). Arsenic is present in different compartments of the environment such as water, land and air. Being a constituent in approximately 200 mineral species, arsenic is associated with mineral deposits including sulphide-bearing rocks, with the most common parent rock being arsenopyrite ($FeAsS_2$). Arsenic is transfer through various carriers or pathways such as drinking water, contaminated food, air, industries, cigarettes and occupational environment, and this makes it a notable risk factor to biota (Chung et al., 2014). Exposure of biota to arsenic causes cancer, reduction of plant metabolism, mutations and mortality. Overally, As has detrimental impacts on human health, aquatic life, ecosystems and environment as a whole (Edelstein and Ben-Hur, 2018).

Chromium is a geochemical metal and 21st most abundant element on earth and its crust. It is also present in mineral soils, rocks and fresh water (Nriagu and Nieboer, 1988). Chromium has a number of oxidation states but the most reported stable forms are hexavalent chromium (Cr^{+6}) and trivalent chromium (Cr^{3+}). Many countries have declared chromium as a priority pollutant because of the level of toxicity it poses to human health and environment. The use of sewage sludge introduces Cr into water sources and soil, which in turn accumulates in plant, animal and human systems through food chain accumulation (Hamilton et al., 2018). Air and industries also serve as pathways of chromium to other spheres of the environment. Different studies have reported several effects of chromium on biota such as mutations, lung cancer, alteration of cell structures, kidney dysfunction, ulcers, birth deficiency and decrease of reproduction (Fernández et al., 2018, Jobby et al., 2018).

Congo red dye is an anionic dye which is prepared and synthesised by coupling naphthionic acid bis-diazotised benzidine; thereafter the mixture is salted out using sodium chloride to form red disodium salt i.e. Congo red dye (Chattopadhyay, 2011). Congo red dye is widely used in textile, leather tanning, printing, plastics, rubber, paper and pulp industries. During dyeing and finishing processes, effluents are discharged into aqueous systems, thereby posing significant risk to living organisms (Naseem et al., 2018). Water pollution by CR causes acute and chronic effects on aquatic life and human health, such as mutations, cancer, respiratory infections, tumours, heart diseases, eye and skin irritations (Zahir et al., 2017, Chawla et al., 2017).

In light of the above, research continues to explore various treatment technologies. Some of the studied wastewater treatment technologies include ion exchange, adsorption precipitation, reverse osmosis and coagulation, of which adsorption is the widely preferred and used due to its cost effectiveness and easy operation (Fernández et al., 2018, Naseem et al., 2018, Singh et al., 2015). There are studies which have reported on the removal of arsenic, chromium and Congo red dye via adsorption using aluminium and iron-based materials due to high affinity of Fe/Al to such pollutants (Cortés-Arriagada and Toro-Labbé, 2016, Mahapatra et al., 2013, Zhu et al., 2018). He et al. (2017), Mikhaylov et al. (2018), and Hosseini Asl et al. (2017) have used Fe/Al hydroxide, Al/Fe oxide-oxyhydroxide sorbent loaded on fly ash, and hydrous Fe-oxide/Al-hydroxide composite, respectively, to remove chromium from water. Maji et al. (2018), Wang et al. (2018) and Meng et al. (2018) reported the use of grapheme oxide@Fe-Al oxide composite,

FeOOH/γ-Al_2O_3 granules, and Fe/Al bimetallic material, respectively, on the removal of arsenic from water. Mahapatra et al. (2013), Zhu et al. (2011) and Cai et al. (2012) have reported on the use of Fe-oxide-Al nanocomposites, magnetic cellulose/Fe_3O_4/activated carbon composite, and γ-Al_2O_3, respectively, for Congo red dye removal from water. Documented studies have used commercial reagents for the removal of prime pollutants from water but have never beneficiated Acid mine drainage (AMD) to reduce its invasion on the environment. This study will be the first to beneficiate authentic/ real AMD by recovering valuable materials and use them to remove pollutants of prime concern from aqueous systems.

Wastewater treatment technologies need to be feasible and affordable. The global economy is already facing serious financial challenge with remediation of contaminated water resources, and therefore cost-effective techniques need to be invented (Biswas et al., 2014). This study, therefore, uses natural adsorbents for removal of arsenic, chromium and Congo red dye from water instead of commercial or synthetic materials. Although there are studies which have reported the use of aluminium and/or iron-based adsorbents for the removal of arsenic, chromium and Congo red dye from water, no study has reported on the recovery of a pollutant from wastewater and use it to beneficiate on the removal of other pollutants. This study focused on the recovery and synthesis of polycationic dimetallic Fe/Al nanocomposites and used them to remove arsenic, chromium and Congo red dye from water.

1.2 Problem statement

South Africa is experiencing an increase in the demand for fresh water due to the startling population growth and continuous pollution of underground and surface water resources resulting from anthropogenic activities (Masindi and Duncker, 2016). During mining and post mining, pyrite is exposed to oxidizing agents. Iron hydroxide and sulphuric acid are toxic chemical species to living organisms when introduced into both surface and underground water resources. This deteriorates the natural form of the water bodies and its ability to foster life (Chuncai et al., 2014). Arsenic, chromium and Congo red dye have several industrial applications; however, they can cause detrimental impacts to human health, ecosystems, soil and the environment as a whole on exposure. Arsenic has been reported to cause hyperpigmentation,

keratosis, cancer and vascular diseases (Mohammed Abdul et al., 2015). Chromium has been reported to cause mutations, lung cancer, alteration of cell structures, kidney dysfunction, ulcers, birth deficiency and decrease of reproduction (Fernández et al., 2018, Jobby et al., 2018). Congo red dye has been reported to cause respiratory infections, tumours, heart diseases, eye and skin irritations (Zahir et al., 2017, Chawla et al., 2017). These pollutants are hazardous and of prime concern because they leach into natural and engineered water bodies, thereby deteriorating water quality. As such, hazardous pollutants need to be removed from wastewater prior discharge to the environment (Ko et al., 2017).

1.3 Objectives

1.3.1 Main objective

The overall aim of this study was to recover and synthesize polycationic/di-metallic/nanocomposite from authentic acid mine drainage (AMD) and explore its application on the removal of As(V), Cr(VI) and CR dye from aqueous solution.

1.3.2 Specific objectives

To achieve the main objective, the following specific objectives were pursued and they are:

- To employ optimum conditions to recover Fe/Al cations from Acid Mine Drainage (AMD) and determine their levels in feed and product water.
- To use different pre-treatment techniques on the resultant sludge to enhance its reactivity and synthesize a polycationic/di-metallic nanocomposite.
- To optimize the operational conditions that are suitable for removal of arsenic, chromium and Congo red dye from aqueous solution.
- To characterize the synthesized nanocomposite before and after reacting with arsenic, chromium and Congo red dye-rich wastewaters.
- To determine the mechanisms that govern the removal of arsenic, chromium and Congo red dye from wastewater using different mathematical models and elucidate the chemistry thereof.
- To compare the quality of product water with different water quality guidelines, specifications, and standards.

- To evaluate the optimum conditions that are suitable for regeneration of the adsorbent and determine feasible cycles.

1.4 Hypothesis

Poly-cationic di-metallic Fe/Al can be recovered from acid mine drainage and be used for the synthesis of Al/Fe poly-cationic/ di-metallic nanocomposite for removal of arsenic, chromium and Congo red dye from aqueous systems.

1.5 Research rationale

The continuous growth of world population and water contamination persist to make demand for clean water surpass supply. As a result, wastewater needs to be treated prior release to the environment to restore water supply and protect the environment. Some technologies for wastewater treatment generate secondary pollution. For example, a technology which uses limestone to treat acid mine drainage (AMD) involves formation of gypsum which could be carrier of hazardous heavy metals. On disposal, toxic heavy metals leach into groundwater aquifers, hence creating a secondary problem. In order to address the issue of secondary pollution, technologies are focusing on value recovery and valorisation of materials from wastewater. This also involves circular economy in the process as materials are recycled and reused.

Wastewater treatment has become an issue of prime concern around the world. This is because traditional technologies have some shortfalls which include generation of secondary solid sludge which becomes a problem on disposal, high operational cost, utilisation of greater land and resources methods; hence green methods need to be developed. The 6th Sustainable Development Goal (SDG) outlines the target for achieving universal and equitable access to safe and affordable drinking water for all. In order to achieve this goal, circular economy approach should be adopted amidst wastewater treatment process. This will help address the problem of landfill overfilling by waste materials which can also be recycled and re-used for beneficiation. Wastewater treatment technologies need to be developed to address such issues; hence researchers need to come with ways to conserve water resources and the environment as a whole for current and future generations. This study recovered valuable materials from acid mine

drainage and utilise them to remove pollutants from other industrial effluents. The approach used for this study was in line with circular economy, and minimised the production of huge volumes of secondary sludge.

1.6 Structure of Thesis

This thesis is comprised of eight chapters which unfold as follows:

CHAPTER ONE: Introduction to the purpose of the study.

CHAPTER TWO: Concise literature review about acid mine drainage, arsenic, chromium and Congo red dye, and their environmental implications, as well as remediation technologies.

CHAPTER THREE: Materials and methods adopted to achieve the objectives of this study

CHAPTER FOUR: Adsorbent Material Synthesis and Characterisation

CHAPTER FIVE: Removal of Arsenic (As(V)) from aqueous solution

CHAPTER SIX: Removal of Chromium (Cr(VI)) from aqueous solution

CHAPTER SEVEN: Removal of Congo Red dye (CR) from aqueous solution

CHAPTER EIGHT: Conclusions and Recommendations

References

Act No 36 of 1998. National Water Act. *In:* FORESTRY, D. O. W. A. A. (ed.). Republic of South Africa: Government Gazette.

BISWAS, A. K., TORTAJADA, C. & IZQUIERDO, R. 2014. *Water Quality Management: Present Situations, Challenges and Future Perspectives*, Taylor & Francis.

CAI, W., HU, Y., CHEN, J., ZHANG, G. & XIA, T. 2012. Synthesis of nanorod-like mesoporous γ-Al2O3 with enhanced affinity towards Congo red removal: Effects of anions and structure-directing agents. *CrystEngComm,* 14**,** 972-977.

CHATTOPADHYAY, D. P. 2011. 4 - Chemistry of dyeing. *In:* CLARK, M. (ed.) *Handbook of Textile and Industrial Dyeing.* Woodhead Publishing.

CHAWLA, S., UPPAL, H., YADAV, M., BAHADUR, N. & SINGH, N. 2017. Zinc peroxide nanomaterial as an adsorbent for removal of Congo red dye from waste water. *Ecotoxicology and Environmental Safety,* 135**,** 68-74.

CHUNCAI, Z., GUIJIAN, L., TING, F., RUOYU, S. & DUN, W. 2014. Leaching characteristic and environmental implication of rejection rocks from Huainan Coalfield, Anhui Province, China. *Journal of Geochemical Exploration,* 143**,** 54-61.

CHUNG, J.-Y., YU, S.-D. & HONG, Y.-S. 2014. Environmental Source of Arsenic Exposure. *J Prev Med Public Health,* 47**,** 253-257.

CORTÉS-ARRIAGADA, D. & TORO-LABBÉ, A. 2016. Aluminum and iron doped graphene for adsorption of methylated arsenic pollutants. *Applied Surface Science,* 386**,** 84-95.

DIERSING, N. 2009. Water Quality: Frequently Asked Questions. *In:* SANCTUARY, F. B. N. M. (ed.). Key West, FL.

DWF 2004. National Water Resource Strategy. First Edition ed.

EDELSTEIN, M. & BEN-HUR, M. 2018. Heavy metals and metalloids: Sources, risks and strategies to reduce their accumulation in horticultural crops. *Scientia Horticulturae*.

FERNÁNDEZ, P. M., VIÑARTA, S. C., BERNAL, A. R., CRUZ, E. L. & FIGUEROA, L. I. C. 2018. Bioremediation strategies for chromium removal: Current research, scale-up approach and future perspectives. *Chemosphere,* 208**,** 139-148.

GOEL, P. K. 2006. *Water Pollution: Causes, Effects and Control*, New Age International.

HAMILTON, E. M., YOUNG, S. D., BAILEY, E. H. & WATTS, M. J. 2018. Chromium speciation in foodstuffs: A review. *Food Chemistry,* 250**,** 105-112.

HE, X., QIU, X. & CHEN, J. 2017. Preparation of Fe(II)–Al layered double hydroxides: Application to the adsorption/reduction of chromium. *Colloids and Surfaces A: Physicochemical and Engineering Aspects,* 516**,** 362-374.

HENKE, K. 2009. *Arsenic: Environmental Chemistry, Health Threats and Waste Treatment*, Wiley.

HOSSEINI ASL, S. M., MASOMI, M., HOSSEINI, M., JAVADIAN, H., RUIZ, M. & SASTRE, A. M. 2017. Synthesis of hydrous iron oxide/aluminum hydroxide composite loaded on coal fly ash as an effective mesoporous and low-cost sorbent for Cr(VI) sorption: Fuzzy logic modeling. *Process Safety and Environmental Protection,* 107**,** 153-167.

JOBBY, R., JHA, P., YADAV, A. K. & DESAI, N. 2018. Biosorption and biotransformation of hexavalent chromium [Cr(VI)]: A comprehensive review. *Chemosphere,* 207**,** 255-266.

KHATRI, N. & TYAGI, S. 2015. Influences of natural and anthropogenic factors on surface and groundwater quality in rural and urban areas. *Frontiers in Life Science,* 8**,** 23-39.

KO, D., LEE, J. S., PATEL, H. A., JAKOBSEN, M. H., HWANG, Y., YAVUZ, C. T., HANSEN, H. C. B. & ANDERSEN, H. R. 2017. Selective removal of heavy metal ions by disulfide linked polymer networks. *Journal of Hazardous Materials,* 332**,** 140-148.

LEPORA, N. 2005. *Chromium*, Marshall Cavendish Benchmark.

MAHAPATRA, A., MISHRA, B. G. & HOTA, G. 2013. Adsorptive removal of Congo red dye from wastewater by mixed iron oxide–alumina nanocomposites. *Ceramics International,* 39**,** 5443-5451.

MAHMOUD, M. E., ABDOU, A. E. H., SHEHATA, A. K., HEADER, H. M. A. & HAMED, E. A. 2018. Sustainable super fast adsorptive removal of Congo red dye from water by a novel technique based on microwave-enforced sorption process. *Journal of Industrial and Engineering Chemistry,* 57**,** 28-36.

MAJI, S., GHOSH, A., GUPTA, K., GHOSH, A., GHORAI, U., SANTRA, A., SASIKUMAR, P. & GHOSH, U. C. 2018. Efficiency evaluation of arsenic(III) adsorption of novel graphene oxide@iron-aluminium oxide composite for the contaminated water purification. *Separation and Purification Technology,* 197**,** 388-400.

MASINDI, V. & DUNCKER, L. 2016. *State of Water and Sanitation in South Africa*.

MENG, C., MAO, Q., LUO, L., ZHANG, J., WEI, J., YANG, Y., TAN, M., PENG, Q., TANG, L. & ZHOU, Y. 2018. Performance and mechanism of As(III) removal from water using Fe-Al bimetallic material. *Separation and Purification Technology,* 191**,** 314-321.

MIKHAYLOV, V. I., MASLENNIKOVA, T. P., KRIVOSHAPKINA, E. F., TROPNIKOV, E. M. & KRIVOSHAPKIN, P. V. 2018. Express Al/Fe oxide–oxyhydroxide sorbent systems for Cr(VI) removal from aqueous solutions. *Chemical Engineering Journal,* 350**,** 344-355.

MOHAMMED ABDUL, K. S., JAYASINGHE, S. S., CHANDANA, E. P. S., JAYASUMANA, C. & DE SILVA, P. M. C. S. 2015. Arsenic and human health effects: A review. *Environmental Toxicology and Pharmacology,* 40**,** 828-846.

NASEEM, K., FAROOQI, Z. H., BEGUM, R. & IRFAN, A. 2018. Removal of Congo red dye from aqueous medium by its catalytic reduction using sodium borohydride in the presence of various inorganic nano-catalysts: A review. *Journal of Cleaner Production,* 187**,** 296-307.

NAZARI, A. M., RADZINSKI, R. & GHAHREMAN, A. 2017. Review of arsenic metallurgy: Treatment of arsenical minerals and the immobilization of arsenic. *Hydrometallurgy,* 174**,** 258-281.

NRIAGU, J. O. & NIEBOER, E. 1988. *Chromium in the Natural and Human Environments*, Wiley.

RATNAIKE, R. N. 2003. Acute and chronic arsenic toxicity. *Postgraduate Medical Journal,* 79**,** 391.

SASMAL, D., MAITY, J., KOLYA, H. & TRIPATHY, T. 2017. Study of congo red dye removal from its aqueous solution using sulfated acrylamide and N, N- dimethyl acrylamide grafted amylopectin. *Journal of Water Process Engineering,* 18**,** 7-19.

SHAHID, M., SHAMSHAD, S., RAFIQ, M., KHALID, S., BIBI, I., NIAZI, N. K., DUMAT, C. & RASHID, M. I. 2017. Chromium speciation, bioavailability, uptake, toxicity and detoxification in soil-plant system: A review. *Chemosphere,* 178**,** 513-533.

SINGH, D. J. & KALAMDHAD, A. 2011. *Effects of Heavy Metals on Soil, Plants, Human Health and Aquatic Life*.

SINGH, R., SINGH, S., PARIHAR, P., SINGH, V. P. & PRASAD, S. M. 2015. Arsenic contamination, consequences and remediation techniques: A review. *Ecotoxicology and Environmental Safety,* 112**,** 247-270.

WANG, Z., SHEN, X., JING, M. & LI, C. 2018. Enhanced arsenic removal from drinking water by FeOOH/γ-Al2O3 granules. *Journal of Alloys and Compounds,* 735**,** 1620-1628.

ZAHIR, A., ASLAM, Z., KAMAL, M. S., AHMAD, W., ABBAS, A. & SHAWABKEH, R. A. 2017. Development of novel cross-linked chitosan for the removal of anionic Congo red dye. *Journal of Molecular Liquids,* 244**,** 211-218.

ZHU, H. Y., FU, Y. Q., JIANG, R., JIANG, J. H., XIAO, L., ZENG, G. M., ZHAO, S. L. & WANG, Y. 2011. Adsorption removal of congo red onto magnetic cellulose/Fe3O4/activated carbon composite: Equilibrium, kinetic and thermodynamic studies. *Chemical Engineering Journal,* 173**,** 494-502.

ZHU, L., FU, F. & TANG, B. 2018. Coexistence or aggression? Insight into the influence of phosphate on Cr(VI) adsorption onto aluminum-substituted ferrihydrite. *Chemosphere,* 212**,** 408-417.

ZIANE, S., BESSAHA, F., MAROUF-KHELIFA, K. & KHELIFA, A. 2018. Single and binary adsorption of reactive black 5 and Congo red on modified dolomite: Performance and mechanism. *Journal of Molecular Liquids,* 249**,** 1245-1253.

CHAPTER TWO

LITERATURE REVIEW

2.0 Introduction

This chapter seeks to review water pollution sources and the respective treatment technologies and the water crisis in South Africa. It also explains the chemistry of acid mine drainage (AMD) and chemical species and materials found in it. Environmental contamination by arsenic, chromium and Congo red dye are briefly explained with their associated health implications, as well as how they are removed from water. Water regulations and requirements in South Africa are also explained in this chapter.

2.1 Water pollution

Water pollution is defined as the direct or indirect change in the physical, chemical and/or biological properties of a water body, that making it less suitable for the any beneficial purpose for which it could be expected to be used, and making it potentially harmful to human health and the environment as a whole (National Water Act, 1998). The change in physical, chemical or biological properties of the water resource may be due to the presence of a toxic chemical species or biological agents which may have exceeded the natural concentrations of water constituents, hence posing a threat to human health and other forms of life (Petrisor, 2017).

2.1.1 Types of water pollution

Water pollution has been divided into different categories according to the properties which get affected and altered, as well as the sources of pollution involved. Physical pollution, chemical pollution and biological pollution are categories reported in literature (Goel, 2006).

2.1.1.1 Physical pollution

Physical pollution of water affects its physical properties which include colour, taste, odour, turbidity and density. Water is a substance which is known to be colourless and tasteless. When water has colour and taste, it could mean that there is foreign matter which has entered the

resource, therefore being a threat to human health and organisms if the pollutant is toxic. The presence of colour prevents sunlight from penetrating into an aquatic system, thus impacting on the metabolism of aquatic plants and animals. Introduction of colour to water is mostly as a result of dyes, and this leads to making the appearance of water unappealing (Jivendra, 1995, Sharma and Kaur, 1994). Heated industrial effluents also affect the density, viscosity and thermal properties of water and this can cause mortality of delicate aquatic organisms as a result of insufficient dissolved oxygen for survival, which would have been depleted by biological organisms for their respirational purposes (Jivendra, 1995).

2.1.1.2 Chemical pollution

Chemical pollution of water affects the pH, acidity, alkalinity, concentration of dissolved oxygen and other gases in water. Organic and inorganic compounds, such as acids, alkalis, dissolved organic and inorganic compounds, and suspended organic and inorganic compounds, are chemical pollutants which cause water pollution. Organic compounds contain fats, carbohydrates and proteins, whereas inorganic compounds can be chloramines, free chlorine, soluble sulphides and heavy metals such as arsenic (As), chromium (Cr), iron (Fe), copper (Cu), lead (Pb) and zinc (Zn) (Weiner and Matthews, 2003). Although some chemical pollutants are biodegradable, there are some which are non-biodegradable and therefore persist in aquatic environment. Insecticides, pesticides, fungicides, herbicides and bactericides are examples of non-biodegradable compounds which persist in the environment for an extended period. Most chemical pollutants accumulate in the food chain and affect all trophic levels, thus posing a serious threat to all living organisms. Agricultural and industrial activities are the major sources of chemical pollution of water (Jivendra, 1995, Petrisor, 2017, Sharma and Kaur, 1994).

2.1.1.3 Biological pollution

Biological pollution of water is related to the introduction and presence of exogenous species in water resources. Common biological pollutants are minute living organisms such ass bacteria, viruses, fungi, protozoa, worms, helminths and algae which multiply in water bodies, and end up posing a threat to human health and aquatic life. Domestic sewage, untreated human and animal waste, and industrial waste are some of the carriers of biological pollutants which are released, intentionally or unintentionally, into waterways (Helmer and Hespanhol, 2002). When humans

and animals are exposed to biological pollutants, they react different and contract a number of waterborne diseases such as diarrhoea, typhoid, cholera and bacillary dysentery which can threaten the population of living organisms (Jivendra, 1995, Petrisor, 2017, Weiner and Matthews, 2003).

2.1.2 Sources of water pollution

Pollution of water results from different sources which are categorised as point sources and non-point sources. The reason for grouping the sources of water pollution is because of the type of source and channel through which pollutants flow before entering a water resource. Sources of water pollution release different kinds of waste into water resources, which in turn affect the water quality and detrimentally impact on human health, livestock, animals, aquatic organisms and the environment as a whole (Nesaratnam, 2014, Weiner and Matthews, 2003).

2.1.2.1 Point sources

Point sources of water pollution are sources which are area-based and can be traced. In most cases, large pipes are connected and channelled to a certain area where waste is discharged. An advantage of point sources is that they can be monitored and managed whenever is a problem is observed. Various forms of waste are released in large quantities into waterways (Nesaratnam, 2014). The waste can be heavy metals, organic compounds, suspended solids, untreated sewage or other toxic species. Examples of point sources of water pollution, but not limited to, include paper and pulp milling industries, sewage treatment plants, manufacturing factories, oil refineries and power plants.

2.1.2.2 Non – point sources

Sources of water pollution which cannot be located or pinpointed, and involve multiple discharge sources are called non-point sources. These sources are also called diffuse sources because the pollutants become spread over a wide area, therefore making it difficult to provide clarity on the origin or exact source of pollution (Nesaratnam, 2014). During rainfall or precipitation, natural and man-made pollutants are carried away by water and deposited into different water bodies, such as rivers, lakes, oceans and groundwater, through surface runoff or underground seepage. The control and management of non-point sources of water pollution remains a serious challenge

due to the difficulty in tracing and identifying the sources (EPA, 2017). Examples of non-point sources of water, amongst others, are urban runoff and storm drainage, agricultural land runoff, acid mine drainage from abandoned mines, deposition of air pollutants from atmosphere onto water resources, and erosion from construction sites. A brief summary of sources of water pollution is illustrated in Figure 2.1.

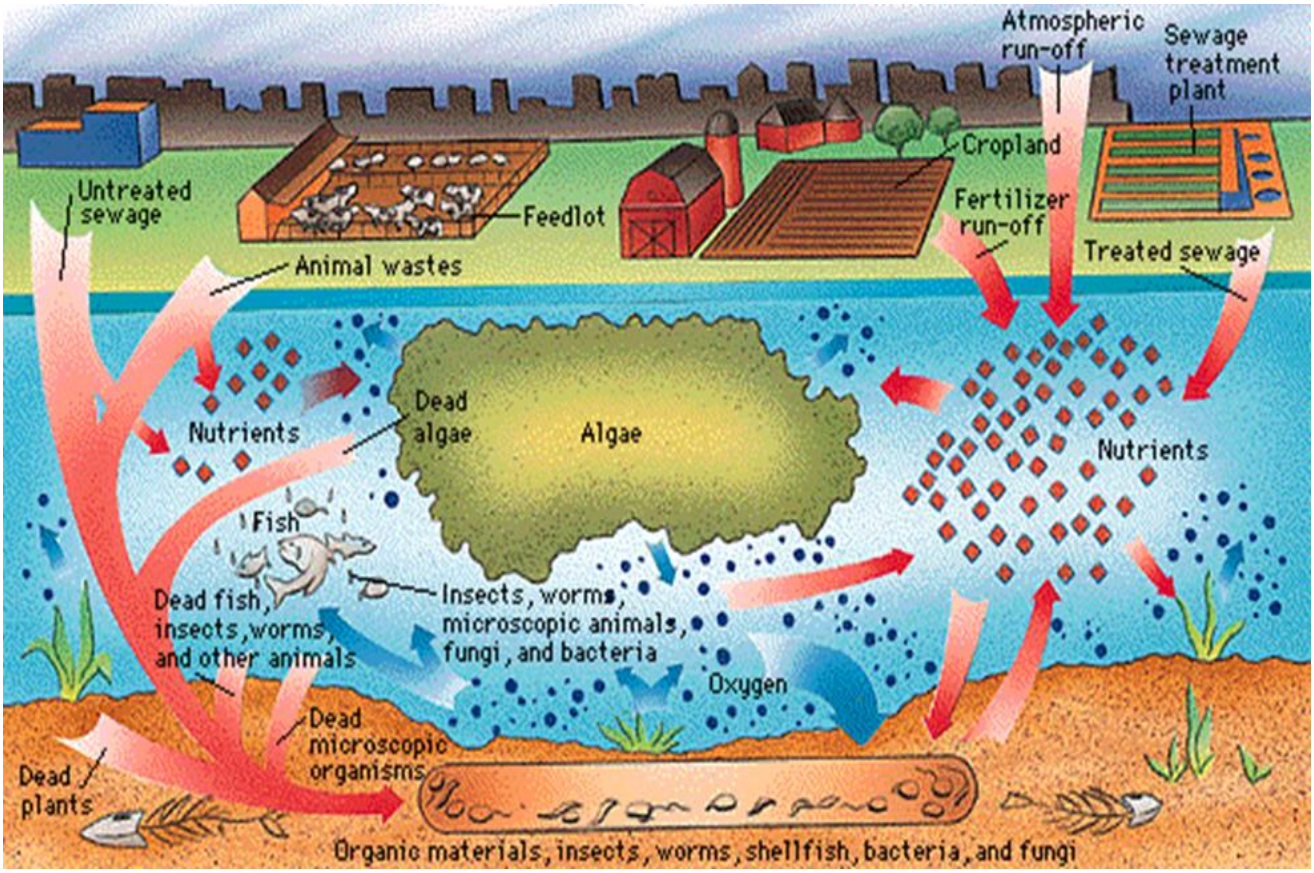

Figure 2.1: Sources of water pollution (Earthian, 2011)

As stated in Section 24 of The Constitution of South Africa, every person has the right to an environment which is not harmful to their health or wellbeing and to have the environment protected from pollution or degradation for the benefit of present and future generations (Bill of Rights, 1996).

2.2 Water shedding in South Africa

South Africa is facing a water crisis which has led to drought in some areas. This has put a burden on major sectors which make significant contributions to the country as well as the global economy. Such sectors which drive the economic growth also make use great amounts of water in order to keep running. The sectors include agriculture, urban use, mining and industrial use, rural use and power generation. Agriculture uses approximately 60% of the available water in the country, with the other 40% shared by the other industries (Thopil and Pouris, 2016). South Africa is experiencing a massive water scarcity which is due to natural causes and anthropogenic activities such as climate change and water pollution, respectively. This has, in turn, harshly impacted on the availability of water resources around the country. A report on dam levels by the Department of Water and Sanitation (2018) indicated that Western Cape has the lowest dam levels of 25.5% in the country due to the severe drought which has struck the region. However, Gauteng, Mpumalanga and Northern Cape have been observed to maintain 92.8%, 77.9% and 67.9%, respectively.

The climate of South Africa ranges from desert and semi-desert in the western region to sub-humid along the eastern coastal areas of the country. Due to the topography and poor rainfall distribution across the country, water availability is unevenly distributed. South Africa's water resources are primarily fed by rain water which has been recorded to be at about 490 mm per annum, thus making it half of the world's average rainfall, with 21% of the country receiving less than 200 mm of rain per year. Approximately 8% of the South Africa's land area has been found to provide about 50% of the run-off, of which 9% ends up in the rivers and 4% recharging the groundwater aquifers (WWF-SA, 2013). Rivers such as the Orange River, Limpopo River, Vaal River and Tugela River are some of the major rivers in South Africa with great drainage areas. A report by the then Department of Water Affairs reported that Limpopo, Komati, Pongola and Orange Rivers are the major contributors to nearly 70% of South Africa's gross domestic product (GDP). South Africa is poorly enriched with groundwater due to the underground hard rock formations which, although abundant in valuable minerals, do not contain any major groundwater aquifers which can significantly be utilized on a national scale (DWF, 2004).

The demand for freshwater is directly related to population growth, however, the need for freshwater is far exceeding the availability of water resources (DWF, 2004). Climate change

continues to be a key player in the impact of South Africa's scarce water resources, together with the poor management and pollution of these limited water resources (CSIR, 2017). This has recently put a serious burden on government as a feasible and urgent long-term solution is needed to address this very problem. According to BusinessTech (2018), the Inter-Ministerial Task Team on Drought and Water Scarcity declared that the drought and water crisis looming in the country has become a national state of disaster. This shows that the country may be headed for a potential crisis which might eventually destroy its economy if global warming continues to follow its projected trajectory due to the continuous practice of anthropogenic activities which detrimentally impact on water resources. Water plays a pivotal role in economic growth and social development, hence it is important to protect and preserve it for current and future generations. Figure 2.2 shows water resource areas in South Africa.

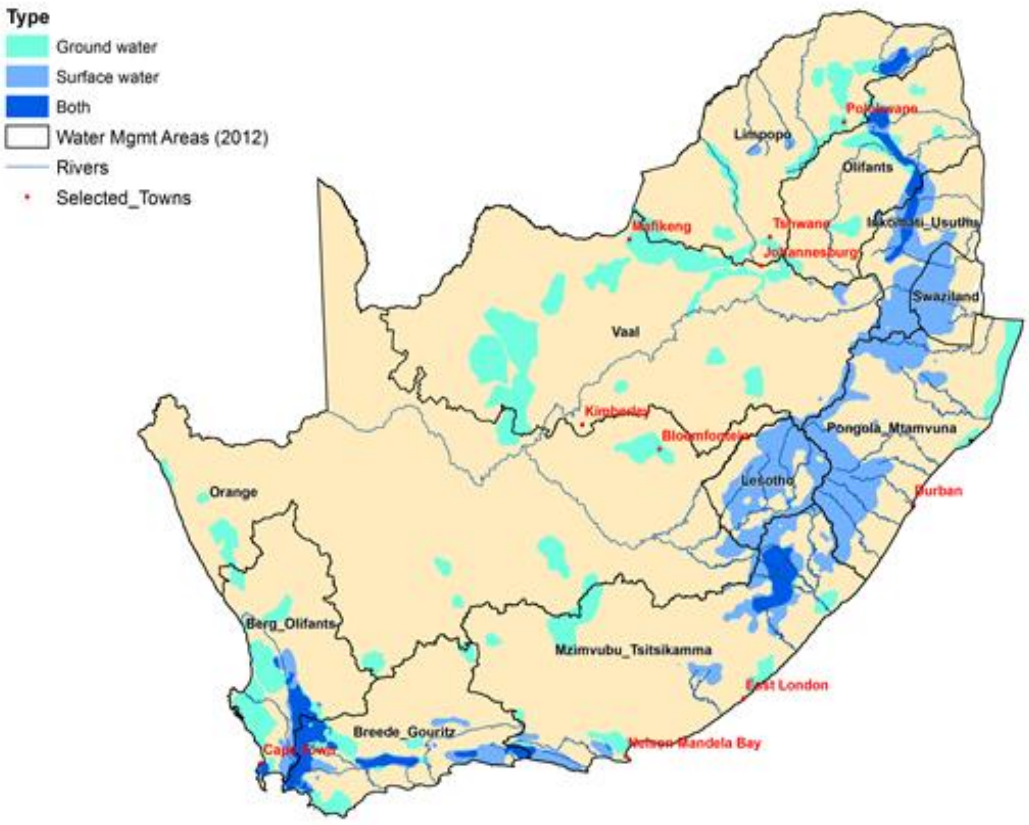

Figure 2.2: South Africa's water source areas (CSIR, 2017)

2.3 Acid mine drainage

Acid mine drainage (AMD) can be briefly described as the product which is formed when sulphide-bearing minerals, such as pyrite (FeS_2), react with water and oxygen, thus releasing sulphuric acid and dissolved heavy metals There are different types of mine drainages, namely: Acid mine drainage, Neutral mine drainage, saline mine drainage and basic mine drainage. Mine drainage continues to receive considerable attention as one of the most significant environmental challenges faced by the mining industry across the world. This is mainly due to the damage they pose to the environment due to elevated concentrations of heavy metals, sulphate, trace metals and pH. Although this is the case, the mining sector keeps expanding as more minerals are exploited for the growth and development of the global economy (INAP, 2012).

Mining activities (both open cut and underground) involve the excavation of large quantities of rock to obtain the target minerals within. During the exploitation of mineral resources, the hard rock (e.g. gold) or soft rock (e.g. coal) is exposed to air and, typically, water. During mining, water can be present in the form of surface runoff and groundwater that is used for cooling, dust mitigation and lubrication. Madzivire et al. (2011) documented that mine water that is formed from the tailings can be acidic, neutral or alkaline depending on the geology that is being exploited during the mining activity. Table 1 shows a list of sulphide bearing materials and their composition.

Table 1: Sulphide bearing materials and their composition (Simate and Ndlovu, 2014)

Mineral ore	Composition	Mineral ore	Composition	Mineral ore	Composition
Pyrite	FeS_2	**Molybdenite**	MoS_2	**Covellite**	CuS
Marcasite	FeS_2	**Millerite**	NiS	**Chalcopyrite**	$CuFeS_2$
Pyrrhotite	Fe_xS_x	**Gelena**	PbS	**Arsenopyrite**	FeAsS
Chalcocite	Cu_2S	**Sphalerite**	ZnS	**Cinnabar**	HgS
Argentite	Ag_2S	**Bismuthitite**	Bi_2S_3		

2.3.1 Formation of mine drainage

2.3.1.1 Acid mine drainage

Acid mine drainage (AMD) is by far, amongst other mine drainage types, the heart of the paramount challenges in the mining industry in the world and is one of the most important water pollution problems ever encountered. AMD is particularly common amongst hard-rock mines (e.g.: iron ore, lead, gold), but can also occur at soft-rock mines (e.g.: coal). This acidic mine drainage is generated when sulphide minerals are exposed to water and oxygen (air) as a result of mining activities that disturbed the underlying geology. The presence of oxygen influences the oxidation reaction where pyrite is exposed to enough electrons. During pyrite oxidation, water promotes the mobilisation of the acid (sulphuric acid) which is formed as water manoeuvres through and over the surfaces of acid bearing rock. Temperature is also an influential factor in AMD formation. AMD is characterized by a number of parameters which include very low pH, high total dissolved solids (TDS), high sulphate ion concentration (SO_4^{2-}) – contributing to high salinity, and high levels of heavy metals – including iron (Fe), aluminium (Al) and manganese (Mn) – contributing to high conductivity. Other toxic metals such as zinc (Zn), copper (Cu), magnesium (Mg), calcium (Ca) are also found in AMD, yet in low concentrations. Formation of AMD also releases other pollutants which are detrimental to the environment (Simate and Ndlovu, 2014, Sheoran and Sheoran, 2006).

The chemistry of AMD formation can be best illustrated by Equations 2.1 – 2.4 (INAP, 2012, Masindi, 2016, Masindi et al., 2018)

Reaction equation 2.1: When pyrite is exposed to air, it gets oxidised, and when water is present, it then decomposes to components which are water-soluble; hence mobility of acid is promoted. Equation 1 below shows the general reaction of pyrite oxidation (FeS_2) and formation of aqueous sulphuric acid.

$$4FeS_2 + 15O_2 + 14H_2O \xrightarrow{\text{bacteria}} 4Fe(OH)_3 + 8SO_4^{2-} + 16H^+ \qquad [2.1]$$

(pyrite) (oxygen) (water) (iron hydroxide) (aqueous sulphuric acid)

The above reaction can be briefly illustrated by the following equations which explain step by step.

Reaction equation 2.2: When pyrite is initially exposed to air and water, it gets oxidised and ferrous ion is formed together with sulphuric acid.

$$2FeS_2 + 7O_2 + 2H_2O \rightarrow 2Fe^{2+} + 4SO_4^{2-} + 4H^+ \quad [2.2]$$

Reaction equation 2.3: When there is sufficient oxygen dissolved in the water or when the water is in sufficient contact with oxygen in the atmosphere, further oxidation occurs where ferrous iron (Fe^{2+}) is oxidised to ferric ion (Fe^{3+})

$$4Fe^{2+} + 4H^+ + O_2 \rightarrow 4Fe^{3+} + 2H_2O \quad [2.3]$$

Reaction equation 2.4: After the formation of the ferric iron, hydrolysis occurs due to the continuous exposure of the ferric iron to water. The precipitate formed is iron hydroxide. Ferric hydroxide precipitates from water in equilibrium with atmospheric oxygen and with pH above 3.3.

$$4Fe^{3+} + 12H_2O \rightarrow 4Fe(OH)_3 + 12H^+ \quad [2.4]$$

Reaction equation 2.5: Sulphide oxidation can be accelerated with the formation of aqueous ferric iron (Fe^{3+}) in the presence of fresh iron sulphide.

$$FeS_2 + 14Fe^{3+} + 8H_2O \rightarrow 15Fe^{2+} + 2SO_4^{2-} + 16H^+ \quad [2.5]$$

The cycle of reactions 3 and 4 continue indefinitely when ferrous iron is produced [equation 5] and with the presence of sufficient dissolved oxygen. The absence of dissolved oxygen leads to completion of equation 5. The water will show elevated levels of ferrous iron after it has been sufficiently catalysed by bacteria such as *Thiobacillus ferrooxidans, ferrobacillus sulphooxidans* and *T. thiooxidans* (Younger et al., 2002, Strosnider et al., 2013).

Geological materials which contain iron sulphides and situated below the water table make the sulphide materials to remain stable and not become oxidised due to the limited oxygen. Yet, where the geologic materials are exposed to air, the potential for oxidation to occur is much high

and water is able to transport the acidity together with other pollutants dissolved in the mine drainage (Pozo-Antonio et al., 2014).

2.3.1.2 Neutral mine drainage

As stated earlier, not all mine drainage is acidic. In AMD, the principal ions are SO_4^{2-}, Fe, Mn and Al, while in neutral mine drainage (NMD), SO_4^{2-} and HCO^{3-} are the major anions, with Ca, Mg and Na being in high concentrations compared to the most common Fe, Al and Mn. Circum-neutral mine drainage is generally characterised by elevated concentrations of metal ions such as Zn, Cd, and Cu as these elements remain soluble over a wide pH range – with Zn elevating up to 179 mg/L in coal mine leachates. Generally, NMD contains low to moderate concentrations of metals but may have elevated content of Cd, Mn, Sb, Zn, As and Se. The concentrations of these metal ions in NMD usually exceed the water quality standards in the receiving water bodies, thus posing a threat to humans and ecosystems (Madzivire et al., 2011, Nordstrom et al., 2015, Pope et al., 2010).

The chemistry of NMD involves the neutralisation of acidity formed by pyrite oxidation. This occurs in the presence of naturally occurring alkaline materials, such as limestone, dolomite, magnesite and ankerite which naturally neutralize acidity formed in reaction equation [2.1]. The most common neutralising material is $CaCO_3$ and the chemistry is illustrated by reaction equation [2.6].

$$CaCO_3 + 2H^+ \leftrightarrow Ca^{2+} + CO_2 + H_2O \qquad [2.6]$$

The H_2O produced is neutral with a pH of ±7. Neutral mine drainage is also observed in location where the weathering on mine wastes occurs with an acid generation potential exceeding the carbonate-based neutralising potential (Jurjovec et al., 2002) and this makes neutral pH conditions to continue until the carbonate mineral is exhausted.

2.3.1.3 Saline mine drainage

Oceanographers define salinity with reference to seawater and dilution, and also on either conductivity or chlorinity. Literature has stated sodium to be in low concentrations in mine water, but it has been found that mines which are situated in coastal areas commonly have high

sodium chloride content. Some areas have rocks which contain sodium–calcium-chloride, and this also contributes to the salinity of mine drainage. Underground coal mines also discharge drainage which is rich in alkali and halogen elements, thus making the mine drainage to be alkaline itself. Saline Mine Drainage contains high levels of calcium and magnesium ions. This mine water also contains low concentration of metals but may still have moderate level of Fe and sulphate (Nordstrom et al., 2015).

2.3.1.4 Basic mine drainage

The basic mine drainage is a rare type of mine drainage and has a pH value of 9. Research has documented a number of factors which contribute to making mine drainage basic. Such factors include evolution of groundwater to a sodium bicarbonate type through ion exchange, sulphate reduction, calcite precipitation for exchange of protons for alkalis with removal of bicarbonate, and low permeability rock with abundant feldspars that can react in a closed system (Nordstrom et al., 2015). Azzie (2002) also revealed the basic state of mine drainage from a coal mine in Vryheid, South Africa.

2.4 Summary of mine drainages

Section 2.3 elaborated on the different types of mine drainages and their principal characteristics. Figure 2.3 provides a summary of characteristics of each type of mine drainage.

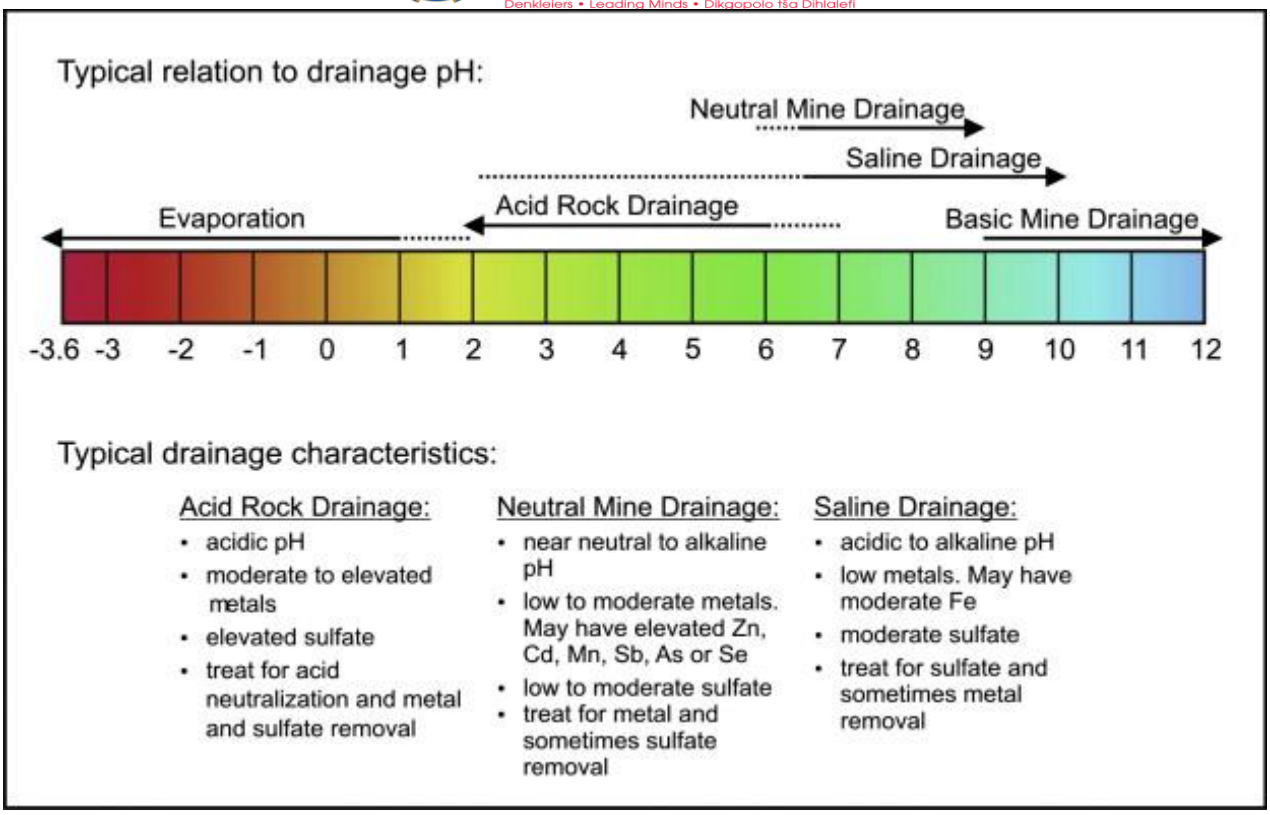

Figure 2.3: Characteristics of the different types of mine drainage (Nordstrom et al., 2015)

2.5 Comparison of AMD treatment technologies in South Africa

The rapid population growth, increasing pressure on water treatment plants, increasing water pollution and demand for fresh water has led to on-going development of wastewater treatment technologies in South Africa. These technologies include those used for AMD treatment. This is, moreover, influenced by the continuous mining activity across the country. Some of the technologies produce sludge which can be processed to raw-materials and valuable by-products. Table 2 below summaries some of the treatment technologies developed in South Africa.

Table 2: AMD treatment technologies in South Africa (DWA, 2010)

Technology	Running Cost	Potential Income	Operation Process
Lime treatment	R5.50/m^3	R5.50/m^3	Precipitation and adsorption
Alkali Barium Calcium (CSIR-ABC)	R4.04/m^3	R0.70/m^3	Precipitation and adsorption
Magnesium Barium Alkali (TUT/CSIR MBA)	R2.22/m^3	R5.58/m^3	Precipitation and adsorption
EARTH	R12.95/m^3	R10.70/m^3	Ion-exchange
BioSURE	R3.80/m^3	R0.00/m^3	Adsorption
SAVMIN (Mintek)	R11.30/m^3	R3.84/m^3	Precipitation
HiPRO (Key Plan)	R9.12/m^3	R3.35/m^3	Reverse Osmosis
ARRO	R12.79/m^3	R4.29/m^3	Reverse Osmosis
Paques Thiopaq	R8.73./m^3	R5.70/m^3	Sulphate removal
CSIRosure	R8.73/m^3	R6.12/m^3	Sulphate removal

2.6 Challenges with mine water treatment technologies

Different technologies have been developed for AMD treatment but cost, handling procedures and generation of secondary sludge which is toxic and harmful and requires special disposal facilities which are costly to maintain have been another problem. This, consequently, has led to the implementation of strict environmental regulations. A summary of comparison between active and passive treatment technologies is shown in Table 3 below.

Table 3: Comparison between passive and active treatment technologies (Jamil et al., 2013)

Method	Active	Passive
Cost	High	Low
Labour requirement	High	Small
Treatment area	Small	Large
Metal recovery	Easy	Difficult
Control	Good	Poor
Predictability	Good	Poor

2.7 Recovery of metals and other resources from acid mine drainage

Different methods have been used to recover metals from acid mine drainage. These methods also make it possible to recover other valuable resources from the contaminated mine water. Resources which are recovered from AMD include: Metal sulphides (e.g. FeS_2 and CuFeS), metals hydroxides (e.g. Fe hydroxides and Al hydroxides), gypsum, Schwertmannite [$(Fe_8O_8(OH)_6SO_4.nH_2O$], Jarosite [$(NaKH_3O^+)Fe_3(SO_4)_2(OH)_6$], Zinc ferrite, Sulphuric acid, sulphur and Rare earth metals (Kefeni et al., 2017).

However, the recovery of metals and other resources depend on the operational conditions, including temperature and time interval, of the different treatment methods and the nature of mine drainage which is treated (e.g. acidic, neutral, alkaline or basic). Most importantly, the resource which is most targeted for recovery is water ((Buzzia et al., 2013) Table 4 shows a summary of products obtained from mine drainage treatment processes

Table 4: Recovery of valuable products from mine drainage treatment processes (2012)

No	Useful products obtained from treatment process
1	Metals recovery
2	Supplements for mine land rehabilitation and revegetation, such as $CaSO_4 .2H_2O$
3	Alkali recovery, such as $CaCO_3$
4	Building and construction related materials, such as gypsum

5	Beneficial use of brine in the cultivation of halophilic organisms, such as algae containing high ß-carotenes and other nutritional supplements
6	Recovery of saleable products, such as sulphur and magnesium salts
7	Agricultural fertilizer
8	Supplement in cement manufacturing
9	Gravel from sludge
10	Metal adsorbents in used industrial wastewater treatment
11	Pigments
12	Clean water

2.8 Recovery of valuables from AMD

2.8.1 Hematite

Hematite is a type of iron oxide pigments which is brown-reddish in colour, and having a chemical formula of α-Fe_2O_3, and contains approximately of 70% of iron. It crystallizes in the corundum structure with oxygen ions in a hexagonal close packed framework. The magnetic moments of the Fe^{3+} ions are ferro-magnetically coupled within specific c-planes, but antiferromagnetically coupled between the planes. As a result of that, it was declared to be paramagnetic. Hematite occurs in many forms including micaceous, massive, crystalline, botryoidal, fibrous and oolitic. Figure 2.4 shows the crystal structure of hematite.

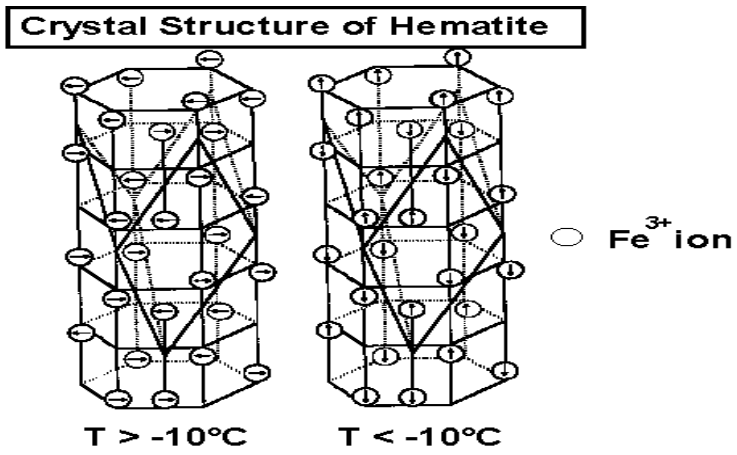

Figure 2.4: Crystal structure of hematite

Hematite occurs naturally and is mined in many parts of the world. Due to its great abundance, hematite is one of the most important ores of iron and has been used for many applications. Different studies have documented the various methods used in the production of hematite. Such methods include precipitation and calcination in the presence of alkaline generating agents. The economic importance of hematite is its utilisation in paints, facial and body decorations.

2.8.2 Goethite

Goethite is a yellow-red-brown iron oxide pigment with a chemical formula α-Fe(O)OH. It is a hydrated ferric oxide compound, and has been found to be most common in soils and other low temperature environments. Hydrated ferric iron consist of ferric iron and has hardness ranging from 5 – 5.5. The yellow iron oxide pigment has been used in many applications such as paints, inks, rubber, cosmetics, roll papers and plastics. This is mainly because it is non-toxic, chemically stable, weather resistant, strong in tinting and cheap (Zhang et al., 2014). Moreover, the production of black iron oxide and red iron oxide pigments also involves the yellow pigment as a raw material, depending on the processes and conditions involved. There are various methods used to produce the yellow pigment and they include precipitation, aniline process, the Pennimanzoph Process and the air oxidation process Fe^{2+} (ferrous) ion to Fe^{3+} (ferric) ion (Larese-Casanova et al., 2010). The Pennimanzoph Process and the air oxidation process are the most frequently used in the production of hydrated ferric oxide. Zhang et al (2014) reported the effectiveness of an integration of bipolar membrane electrodialysis (BMED) with the air oxidation process to produce yellow iron oxide pigments. Figure 2.5 shows the crystal structure of goethite.

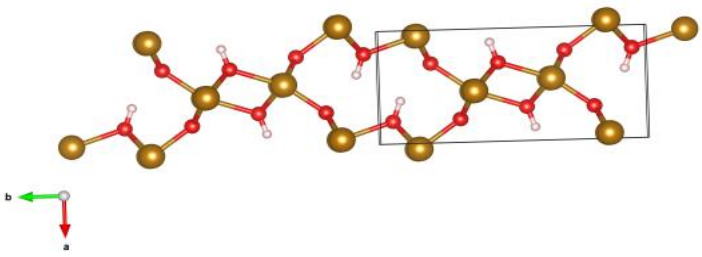

Figure 2.5: Crystal structure of goethite with gold atoms = iron, red atoms=oxygen and pink atoms=hydrogen

2.8.3 Magnetite

Magnetite is one of the oxides of iron with a chemical formula Fe_3O_4 or $FeO.Fe_2O_3$ and is black-grey in colour. It possesses an inverse spinel structure with Fe(III) ions distributed randomly between octahedral and tetrahedral sites, and Fe(II) ions in octahedral sites (Sulistyaningsih et al., 2017), with opaque crystals. A study by Tajabadi and Khosroshahi (2012) showed that the particle size of magnetite increases with the increase alkalinity of medium, but decreases with an increase in temperature and synthesis time. Magnetite is a ferromagnetic mineral, thus making it attracted to magnets and also carries the ability of becoming a permanent magnet itself (Wasilewski and Günther, 1999). Figure 2.6 shows the spinel structure of magnetite.

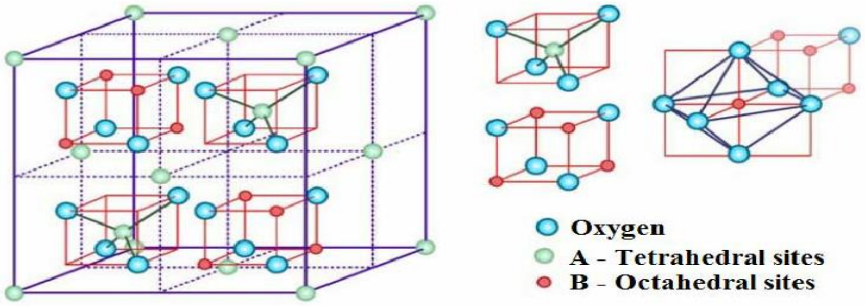

Figure 2.6: Spinel structure of magnetite (Ristanović et al., 2015)

Different methods are used to synthesise and recover magnetite, and they include co-precipitation (Mahmed et al., 2011; Khalil, 2015; Yu et al., 2017) and precipitation (Šutkaa et al., 2014). However, Yu et al (2017) stated that experimental conditions such as pH, stirring rate, reaction temperature, ferrous ion concentration and reaction time play a role in the recovery of magnetite. Magnetite has been used for various applications such as drug carrier, cancer therapy, drug release, heavy metal adsorbent and proton exchange membrane. The advantage of using magnetite is that it is non-toxic and can be easily separated from a solution by an external magnet (Sulistyaningsih et al., 2017), hence making magnetite to become an important material in many industries.

2.9 Arsenic

Arsenic is the 33rd chemical element in the periodic table with an atomic mass of 74.9216 a.m.u. It is a toxic metalloid which has different allotropes appearing in different colours, such as grey, yellow and black, with grey being the most common. Amongst other elements found in the

earth's crust, arsenic is the twentieth most abundant element with approximately 200 kinds of minerals. It cycles through compartments and systems of the environment, namely hydrosphere, atmosphere, lithosphere and biosphere. Although arsenic naturally exists in the environment, its concentration can be elevated by certain natural processes and anthropogenic activities (Hao et al., 2015, Parascandola, 2012).

Arsenic (As) is one of the most toxic chemical species in the history of metals and a global health risk concern. It is naturally ubiquitous and occurs in nature in various states such as $-3, 0, +3$ and $+5$ (Mohammed Abdul et al., 2015). Arsenic compounds are commonly classified in three major categories, namely inorganic, organic and arsine gas, which also relate to their toxicity level. Studies have reported that inorganic arsenic compounds are more poisonous than organic arsenic compounds because the rate at which inorganic arsenic is absorbed is higher than that of organic arsenic. Other factors which influence the toxicity of arsenic compounds include the oxidation state, solubility, physical state, purity and the rates of absorption and elimination. Arsine gas is the most toxic form of arsenic and elemental arsenic is the least toxic form of arsenic (ATSDR, 2009, Hughes et al., 2011). Equation 2.7 shows the toxicity level with respect to the type of arsenic.

$$\text{Arsine gas}(AsH_3) > \text{Inorganic}\ (As^{3+}) > \text{Organic}\ (As^{3+}) > \text{Inorganic}\ (As^{5+}) > \text{Organic}\ (As^{5+}) > \text{Elemental arsenic}\ (As^{0}) \quad [2.7]$$

Arsenic (As) is found in nature at certain levels or concentrations. Although arsenic is a natural species which is released via natural processes, different studies have document it is also released in the environment as result of anthropogenic or man-made activities (Sarkar and Paul, 2016). Arsenic is ubiquitous in the environment and there are various natural processes which release it to different compartments of the environment, including water, land, air and living systems. The content of arsenic varies from one natural source to another. The earth's crust contains arsenic which is concentrated between 1.5 – 2 ppm. Amongst other elements found in the earth's crust, arsenic is the twentieth most abundant element with approximately 200 mineral forms (NRC, 1977). Many studies have documented many arsenic-containing mineral ores, but the most common is arsenopyrite (FeAsS) which contains sulphur and readily oxidises to arsenic trioxide and arsenate state at a later stage. Arsenic has also been found in igneous and

sedimentary rocks at higher concentrations than the content found in coal, sandstones and shales. The highest arsenic concentration in sediments ever reported was 2 100 mg/L in the Red Sea (Danielsson et al., 1980, R. Kaplan et al., 1969, Assembly of Life Sciences, 1977). Arsenic is also released from the geosphere to water, land and atmosphere through volcanic eruptions (Henke, 2009). Depending on the geographic area and geologic history of the soil, very elevated concentrations of arsenic have been reported in a number of regions. Arsenic content between 0.1 – 40 mg/L (Colbourn et al., 1975) was discovered in virgin soils, and the highest reported concentration in soils covering sulphide ores being 8 000 mg/L. Organic matter binds with arsenic in soil and this becomes an environmental issue of concern because organic matter gets oxidised and when plants absorb nutrients from soil, the available arsenic gets absorbed too (NRC, 1977). Groundwater in different regions has been found to have arsenic as a result of mineralogical characteristics of the underlying aquifer and its arsenic content (Sarkar and Paul, 2016). A wide range of arsenic concentration in oceanic water has been reported to be between 0.15 – 8 µg/L (Chappell et al., 2001, Nriagu et al., 2007, Sarkar and Paul, 2016).

Arsenic has been declared a pollutant of prime concern and serious interventions are required to curtail the impacts of this pollutant. Although arsenic has several industrial uses, such as agricultural chemicals, glass manufacturing and electronics. Exposure can cause detrimental impacts to the human health, ecosystems, soil, and the environment (Edelstein and Ben-Hur, 2018). Arsenic can be taken up by plants, consumed by animals and humans, and translocate to a food chain via bio-magnification and bio-accumulation. This results in the reduction of the physiological metabolism and potential death of living organisms (Singh and Kalamdhad, 2011). Arsenic can cause acute and long term effects such as diarrhoea, vomiting, abdominal pain, cancer, pulmonary, cardiovascular disease, and cancer (Ratnaike, 2003).

2.10 Chromium

Chromium ore is one of the leading minerals making a significant contribution towards growth and development of global economy. The importance of chromium in society has recently made some countries which do not have chrome resources to import chromium resources from chromium-rich states. South Africa possesses approximately 70 per cent of the global chromium resources, from which China receives about 90 per cent as imports for its industrial use and

production (Creamer, 2017). A report by the US Geological Survey detailed that South Africa and Kazakhstan are the world's largest producers of chromium with approximately 95 per cent of chromium resources in the world (Papp, 2017). The astonishing abundance was also reported by various studies, where they documented that about 68 per cent of the world's reserves' chromite ores is concentrated in the Republic of South Africa (Brown, 2002, Howat, 1986).

The production and manufacturing of chromium-containing materials and products continue to grow in order to boost the global market and economy. Chromium is a crucial ingredient in chemical production, metallurgical industries, and refractories and foundries (Dhal et al., 2013). Natural sources, such as water, soil, plants, animals, rocks, volcanic eruptions and minerals, and anthropogenic activities, such as mining, tanning, and manufacturing of paints, plastics, ceramics, glass, salts, dyes and dietary supplements release chromium to different spheres of the environment at different concentrations. In nature, chromium is normally or commonly found as the stable trivalent [Cr(III)] chromium (Santonen et al., 2009). There are approximately forty (40) minerals that contain chromium. Amongst those minerals, chromite [$FeCr_2O_4$ or $[(Fe, Mg, Al)Cr_2O_4]$ is the most common and important in industries because of the valuable products which are manufactured using it (Nriagu and Nieboer, 1988).

Chromium is a valuable metal but also a toxic chemical component. It is the seventh and 21st most abundant element on earth and in the earth's crust, respectively (Nriagu and Nieboer, 1988). A number of oxidation states of chromium have been reported in literature, but the common ad most stable are elemental chromium (Cr^0), trivalent chromium (Cr^{3+}) and hexavalent chromium (Cr^{6+}), of which Cr^{6+} is the most toxic (Shanker et al., 2005, Tuteja and Gill, 2012). The states vary in properties and degree of toxicity towards human health and other living organisms. Nevertheless, contamination of water by chromium directs detrimental impacts to human health through bioaccumulation or food chain contamination, animals, aquatic organisms and the environment at large (Shahid et al., 2017). This, therefore, triggers the importance of developing cheap but effective treatment and remediation technologies for chromium-contaminated water resources.

2.11 Congo red dye

Congo red dye (CR) is one of the common dyes used in different industries for a number of purposes. It is an organic anionic dye with molecular formula and molecular weight of $C_{32}H_{22}N_6Na_2O_6S_2$ and 696.664 g/mol. It is a diazo dye with two nitrogen atoms linked to each other as terminal functional groups. When in a basic aqueous system, it is red, whereas in acidic aqueous systems, it turns blue. Water contamination by CR has been reported, in most cases, to be adversely affecting the quality and aesthetic nature of water of the receiving streams because of, but not limited to, eutrophication (Shaban et al., 2017). Food, rubber, plastics, cosmetics, pharmaceuticals, textiles dyeing and printing industries not only use large amounts of water, but also release great volumes of CR-contaminated water.

Although important in industries, CR has been reported to be highly poisonous and carcinogenic, hence the need for efficient and cost-effective of CR-contaminated water. Different studies have reported on the different removal techniques of CR from water. Adsorption (Zahir et al., 2017, Aliabadi and Mahmoodi, 2018), catalytic reduction, bio-reduction (Chakraborty et al., 2013), ultrasound degradation, photocatalytic reduction, microwave enforced sorption (Mahmoud et al., 2018), nanofiltration (Hairom et al., 2015) and bio-sorption are some of the studies removal techniques of CR from water.

2.12 Conclusions

From the literature survey, a variety of areas of concern were identified which relate to the main focus of this study. A number of different treatment technologies for AMD were described and it was noted that valuable products or minerals have not been recovered from natural AMD using sodium-based reagents and used to treat other contaminated water streams. The technologies discussed in this chapter, however showed the problems with cost factor, large footprint, etc., which makes them not be good choices for mine water treatment. This study, therefore, focuses on recovery of iron and aluminium from natural or authentic acid mine water and explore their effectiveness in treating As, Cr and CR contaminated water.

References

2012. INAP: The International Network for Acid Prevention. *Global Acid Rock Drainage Guide* [Online]. Available: http://www.gardguide.com/index.php?title=Chapter_7 [Accessed June 09].

ALIABADI, R. S. & MAHMOODI, N. O. 2018. Synthesis and characterization of polypyrrole, polyaniline nanoparticles and their nanocomposite for removal of azo dyes; sunset yellow and Congo red. *Journal of Cleaner Production,* 179**,** 235-245.

ASSEMBLY OF LIFE SCIENCES 1977. *Arsenic*, National Academy of Sciences.

ATSDR. 2009. *Arsenic Toxicity*

What is Arsenic? [Online]. Available: https://www.atsdr.cdc.gov/csem/csem.asp?csem=1&po=4 [Accessed].

AZZIE, B. 2002. *Coal mine waters in South Africa: Their geochemistry,quality and classification.* University of Cape Town, South Africa.

BILL OF RIGHTS 1996. Constitution of the Republic of South Africa. *In:* GOVERNMENT, S. A. (ed.).

BROWN, C. E. 2002. *World Energy Resources*, Springer Berlin Heidelberg.

BUZZIA, D. C., VIEGASB, L. S., RODRIGUESC, M. A. S., BERNARDESB, A. M. & TENÓRIOA, J. A. S. 2013. Water recovery from acid mine drainage by electrodialysis. *Minerals Engineering,* 40**,** 82-89.

CHAKRABORTY, S., BASAK, B., DUTTA, S., BHUNIA, B. & DEY, A. 2013. Decolorization and biodegradation of congo red dye by a novel white rot fungus Alternaria alternata CMERI F6. *Bioresource Technology,* 147**,** 662-666.

CHAPPELL, W. R., ABERNATHY, C. O. & CALDERON, R. L. 2001. *Arsenic Exposure and Health Effects IV*, Elsevier Science.

COLBOURN, P., ALLOWAY, B. J. & THORNTON, I. 1975. Arsenic and heavy metals in soils associated with regional geochemical anomalies in South-West England. *Science of The Total Environment,* 4**,** 359-363.

CREAMER, M. 2017. South Africa crucial to global chrome supply, Chromium 2017 hears. *Creamer Media's Engineering News*, 2017-11-10.

CSIR 2017. Protecting South Africa's Strategic Water Source Areas. *In:* TSEDU, T. (ed.).

DANIELSSON, L.-G., DYRSSEN, D. & GRANÉLI, A. 1980. Chemical investigations of Atlantis II and discovery brines in the Red Sea. *Geochimica et Cosmochimica Acta,* 44**,** 2051-2065.

DHAL, B., THATOI, H. N., DAS, N. N. & PANDEY, B. D. 2013. Chemical and microbial remediation of hexavalent chromium from contaminated soil and mining/metallurgical solid waste: A review. *Journal of Hazardous Materials,* 250-251**,** 272-291.

DWA 2010. Mine Water Management in the Witwatersrand Gold Fields with special emphasis on Acid Mine Drainage.

DWF 2004. National Water Resource Strategy. First Edition ed.

EARTHIAN 2011. What a pollution!

EDELSTEIN, M. & BEN-HUR, M. 2018. Heavy metals and metalloids: Sources, risks and strategies to reduce their accumulation in horticultural crops. *Scientia Horticulturae*.

EPA. 2017. *Polluted Runoff: Nonpoint Source Pollution* [Online]. United States Environmental Protection Agency. Available: https://www.epa.gov [Accessed 2018-03-23].

GOEL, P. K. 2006. *Water Pollution: Causes, Effects and Control*, New Age International.

HAIROM, N. H. H., MOHAMMAD, A. W. & KADHUM, A. A. H. 2015. Influence of zinc oxide nanoparticles in the nanofiltration of hazardous Congo red dyes. *Chemical Engineering Journal,* 260**,** 907-915.

HAO, J., HAN, M.-J., HAN, S., MENG, X., SU, T.-L. & WANG, Q. K. 2015. SERS detection of arsenic in water: A review. *Journal of Environmental Sciences,* 36**,** 152-162.

HELMER, R. & HESPANHOL, I. 2002. *Water Pollution Control: A Guide to the Use of Water Quality Management Principles*, CRC Press.

HENKE, K. 2009. *Arsenic: Environmental Chemistry, Health Threats and Waste Treatment*, Wiley.

HOWAT, D. D. 1986. Chromium in South Africa. *Journal of the South African Institute of Mining and Metallurgy,* 86**,** 37-50.

HUGHES, M. F., BECK, B. D., CHEN, Y., LEWIS, A. S. & THOMAS, D. J. 2011. Arsenic Exposure and Toxicology: A Historical Perspective. *Toxicological Sciences,* 123**,** 305-332.

INAP. 2012. *The Global Acid Rock Drainage Guide* [Online]. Available: http://www.gardguide.com/index.php?title=Summary#Formation_of_Acid_Rock_Drainage [Accessed 12 September 2019].

JIVENDRA 1995. *Water pollution management,* New Delhi, A.P.H. Pub. Corp.

JURJOVEC, J., PTACEK, C. J. & BLOWES, D. W. 2002. Acid neutralization mechanisms and metal release in mine tailings: a laboratory column experiment. *Geochimica et Cosmochimica Acta,* 66**,** 1511-1523.

KEFENI, K. K., MSAGATI, T. A. M. & MAMBA, B. B. 2017. Acid mine drainage: Prevention, treatment options, and resource recovery: A review. *Journal of Cleaner Production,* 151**,** 475–493.

MADZIVIRE, G., GITARI, W. M., VADAPALLI, V. R. K., OJUMU, T. V. & PETRIK, L. F. 2011. Fate of sulphate removed during the treatment of circumneutral mine water and acid mine drainage with coal fly ash: Modelling and experimental approach. *Minerals Engineering,* 24**,** 1467-1477.

MAHMOUD, M. E., ABDOU, A. E. H., SHEHATA, A. K., HEADER, H. M. A. & HAMED, E. A. 2018. Sustainable super fast adsorptive removal of Congo red dye from water by a novel technique based on microwave-enforced sorption process. *Journal of Industrial and Engineering Chemistry,* 57**,** 28-36.

MASINDI, V. 2016. A novel technology for neutralizing acidity and attenuating toxic chemical species from acid mine drainage using cryptocrystalline magnesite tailings. *Journal of Water Process Engineering,* 10**,** 67-77.

MASINDI, V., OSMAN, M. S., MBHELE, R. N. & RIKHOTSO, R. 2018. Fate of pollutants post treatment of acid mine drainage with basic oxygen furnace slag: Validation of experimental results with a geochemical model. *Journal of Cleaner Production,* 172**,** 2899-2909.

MOHAMMED ABDUL, K. S., JAYASINGHE, S. S., CHANDANA, E. P. S., JAYASUMANA, C. & DE SILVA, P. M. C. S. 2015. Arsenic and human health effects: A review. *Environmental Toxicology and Pharmacology,* 40**,** 828-846.

NATIONAL WATER ACT 1998. National Water Act: Act No. 36 of 1998. *In:* GOVERNMENT, S. A. (ed.).

NESARATNAM, S. T. 2014. *Water Pollution Control*, Wiley.

NORDSTROM, D. K., BLOWES, D. W. & PTACEK, C. J. 2015. Hydrogeochemistry and microbiology of mine drainage: An update. *Applied Geochemistry,* 57**,** 3-16.

NRC 1977. *Arsenic: Medical and Biological Effects of Environmental Pollutants,* Washington, DC, The National Academies Press.

NRIAGU, J. O., BHATTACHARYA, P., MUKHERJEE, A. B., BUNDSCHUH, J., ZEVENHOVEN, R. & LOEPPERT, R. H. 2007. Arsenic in soil and groundwater: an overview. *Trace Metals and other Contaminants in the Environment.* Elsevier.

NRIAGU, J. O. & NIEBOER, E. 1988. *Chromium in the Natural and Human Environments*, Wiley.

PAPP, J. F. 2017. Mineral Commodity Summaries. U.S. Geological Survey.

PARASCANDOLA, J. 2012. *King of poisons : a history of arsenic,* Washington, D.C., Potomac Books.

PETRISOR, I. 2017. *What is water pollution?* [Online]. Available: www.environmentalpollutioncenters.org/water [Accessed 2018-03-22].

POPE, J., NEWMAN, N., CRAW, D., TRUMM, D. & RAIT, R. 2010. Factors that influence coal mine drainage chemistry West Coast, South Island, New Zealand. *New Zealand Journal of Geology and Geophysics,* 53**,** 115-128.

POZO-ANTONIO, S., PUENTE-LUNA, I., LAGÜELA-LÓPEZ, S. & VEIGA-RÍOS, M. 2014. Techniques to correct and prevent acid mine drainage: A review. *Scientific Electronic Library Online (SciELO).*

R. KAPLAN, I., E. SWEENEY, R. & NISSENBAUM, A. 1969. *Sulfur Isotope Studies on Red Sea Geothermal Brines and Sediments*.

RATNAIKE, R. N. 2003. Acute and chronic arsenic toxicity. *Postgraduate Medical Journal,* 79**,** 391.

SANTONEN, T., ORGANIZATION, W. H., PROGRAMME, U. N. E., ORGANISATION, I. L., CHEMICALS, I.-O. P. F. T. S. M. O. & SAFETY, I. P. O. C. 2009. *Inorganic Chromium(III) Compounds*, World Health Organization.

SARKAR, A. & PAUL, B. 2016. The global menace of arsenic and its conventional remediation - A critical review. *Chemosphere,* 158**,** 37-49.

SHABAN, M., ABUKHADRA, M. R., HAMD, A., AMIN, R. R. & ABDEL KHALEK, A. 2017. Photocatalytic removal of Congo red dye using MCM-48/Ni2O3 composite synthesized based on silica gel extracted from rice husk ash; fabrication and application. *Journal of Environmental Management,* 204**,** 189-199.

SHAHID, M., SHAMSHAD, S., RAFIQ, M., KHALID, S., BIBI, I., NIAZI, N. K., DUMAT, C. & RASHID, M. I. 2017. Chromium speciation, bioavailability, uptake, toxicity and detoxification in soil-plant system: A review. *Chemosphere,* 178**,** 513-533.

SHANKER, A. K., CERVANTES, C., LOZA-TAVERA, H. & AVUDAINAYAGAM, S. 2005. Chromium toxicity in plants. *Environment International,* 31**,** 739-753.

SHARMA, B. K. & KAUR, H. 1994. *Water pollution,* Meerut, Krishna Prakashan Mandir.

SHEORAN, A. S. & SHEORAN, V. 2006. Heavy metal removal mechanism of acid mine drainage in wetlands: A critical review. *Minerals Engineering,* 19**,** 105-116.

SIMATE, G. S. & NDLOVU, S. 2014. Acid mine drainage: Challenges and opportunities. *Journal of Environmental Chemical Engineeering***,** 1785-1803.

SINGH, D. J. & KALAMDHAD, A. 2011. *Effects of Heavy Metals on Soil, Plants, Human Health and Aquatic Life*.

STROSNIDER, W. H. J., NAIRN, R. W., PEER, R. A. M. & WINFREY, B. K. 2013. Passive co-treatment of Zn-rich acid mine drainage and raw municipal wastewater. *Journal of Geochemical Exploration,* 125**,** 110-116.

THOPIL, G. A. & POURIS, A. 2016. A 20 year forecast of water usage in electricity generation for South Africa amidst water scarce conditions. *Renewable and Sustainable Energy Reviews,* 62**,** 1106-1121.

TUTEJA, N. & GILL, S. S. 2012. *Crop Improvement Under Adverse Conditions*, Springer New York.

WEINER, R. F. & MATTHEWS, R. 2003. Updated verison of Environmental Engineering. *Environmental Engineering (Fourth Edition).* Burlington: Butterworth-Heinemann.

WWF-SA 2013. An Introduction to South Africa's Water Source Areas.

YOUNGER, P. L., BANWART, S. A. & HEDIN, R. S. 2002. *Mine Water: Hydrology, Pollution, Remediation*, Springer Netherlands.

ZAHIR, A., ASLAM, Z., KAMAL, M. S., AHMAD, W., ABBAS, A. & SHAWABKEH, R. A. 2017. Development of novel cross-linked chitosan for the removal of anionic Congo red dye. *Journal of Molecular Liquids,* 244**,** 211-218.

CHAPTER THREE

MATERIALS AND METHODS

3.0 Introduction

This chapter unpacks the materials and methods used to synthesise the adsorbent and to remove As(V), Cr(VI) and CR from aqueous solution.

3.1 Sampling and stock solution preparation

Raw Fe-rich acid mine drainage (AMD) was collected from a Coal Mine in Witbank located in Mpumalanga Province, South Africa. Caustic soda (NaOH) was purchased from Merck (Pty) Ltd. Sodium arsenate dibasic heptahydrate was purchased from Fluka Analytical which was used to prepare As(V) stock solution. Potassium dichromate salt ($K_2Cr_2O_7$) and Congo red dye (CR) were purchased from Sigma-Aldrich, which were used to prepare Cr(VI) and CR stock solutions, respectively. All chemicals used were of analytical grade and were used as received without any further purification. Reaction vessels (glassware) were thoroughly and carefully cleaned with deionized water before every use, and all solutions were prepared with ultra-pure water (18.2 MΩ-cm). Table 5 illustrates the characterisation results for authentic AMD collected from the mine.

Table 5: Chemical composition of raw authentic AMD

Parameter	**Raw AMD**
pH	2.3 ± 0.2
Acidity (mg/L CaCO3)	8133 ± 0.5
Alkalinity (mg/L CaCO3)	<5,0 ± 0
Aluminium (mg/L Al)	280 ± 2
Calcium (mg/L Ca)	337 ± 1.5

Electrical Conductivity (mS/m)	5470 ± 3
Iron (mg/L Fe)	1818 ± 4
Magnesium (mg/L Mg)	273 ± 0.6
Manganese (mg/L Mn)	75 ± 0.9
Potassium (mg/L K)	60 ± 0.5
Sodium (mg/L Na)	30 ± 0.5
Sulphate (mg/L SO4)	80000 ± 10
Total Dissolved Solids	135560 ± 0.5
Total Hardness (mg/L)	1965 ± 0.5

3.2 Recovery and synthesis of PDFe/Al nanocomposite from AMD

A specific volume of authentic AMD was reacted with a dosage of NaOH to increase the pH for precipitation of iron and aluminium via selective and fractional precipitation. Polycationic di-metal Fe/Al (PDFe/Al) nanocomposite was recovered and synthesised under standard conditions of temperature (298 K) and pressure (1 atm).

The mixture was then agitated for 60 minutes at room temperature measured to be ±24 ºC. The resultant mixture was subjected to heat for 120 minutes for agglomeration of the particles. After heating, the flask was left for cooling at room temperature. After cooling, filtration was done via vacuum filtration using Whatman® Grade 40 ash-less filter paper. The sludge was then dried under room temperature. Post drying, the recovered and synthesized Polycationic Dimetallic Fe/Al (PDFe/Al) nanocomposites were calcined at 100 ºC and vibratory-ball-milled to a fine powder at a speed of 700 rpm to enhance their reactivity. After milling, the sample was sieved through a 32 µm particle size sieve to attain uniform particle sizes. The samples were kept safe in a plastic zip-lock bag until use. The supernatant was taken for water quality characterization and to determine the fate of pollutants in feed water.

3.3 Characterization of aqueous samples

The pH levels of aqueous solutions before and after chemical reactions were determined using a Thermo Scientific™ Orion 3 Star portable pH meter. Electrical conductivity (EC), total dissolved solids (TDS) and salinity were determined using a Mettler Toledo FiveGo EC/TDS/Salinity/Temperature portable multi meter. Metal ions and sulphate concentrations in aqueous samples and solutions were analysed using AAS and ICP-MS (7500ce, Agilent, Alpharetta, GA, USA), and IC (850 professional IC Metrohm, Herisau, Switzerland), respectively. For CR, the colour removal was analysed by measuring the absorbance with a UV/Vis spectrophotometer at ƛ max = 614 nm.

3.4 Characterization of feed and recovered materials

3.4.1 Mineralogical composition analysis

Mineralogical composition of nanocomposites before and after adsorption was determined through X-ray diffraction patterns (XRD) which were obtained from a PANalytical X'Pert Pro powder diffractometer using Cu-Kα radiation with X'Celerator detector. A step size of 0.02° and scan speed of 0.03° per second were used to conduct XRD patterns taken at high angles of 2θ ≈ 10 - 90°. A back loading preparation method was used to prepare samples for the feed material and products. X'Pert Highscore plus software was used to identify phases in the materials, with the relative phase amounts (mass%) estimated by Rietveld quantitative analysis which is a powerful method for determining the quantities of crystalline and amorphous components in multiphase mixtures (Hillier et al., 2013).

3.4.2 Functional group analysis

For determination of functional groups in nanocomposites before and after adsorption, the measurement of lattice vibrations of the PDFe/Al nanocomposites was performed by using attenuated total reflection Fourier transform infrared spectroscopy (ATR-FTIR). A Perkin-Elmer Spectrum 100 Fourier Transform Infrared Spectrometer (FTIR) equipped with a Perkin-Elmer Precisely Universal Attenuated Total Reflectance (ATR) sampling accessory equipped with a diamond crystal was used to record the infrared spectra at room temperature. The instrument was connected to a PC which used Spectrum software to control the instrument and to record the

spectra. The powdered sample was placed on the crystal and a force was applied to ensure proper contact between the sample and the crystal. The spectral study was extended over the range 4000–400 cm^{-1}, experimental set-up and analytical methods 41 with a resolution of 4 cm-1 and 32 accumulations. Spectrum 100 software (Perkin Elmer) was used to analyse the spectra.

3.4.3 Morphological analysis

To determine surface morphologies and size distribution of the nanocomposites before and after adsorption, a JEOL JSM7500 microscope was used to collect high-vacuum scanning electron micrographs (SEM images). Samples were dispersed on a carbon tape and sputter-coated with a thin, conductive layer of gold using an Emitech K950X sputter coater, with the acceleration voltage being 2.00 kV. Energy Dispersive X-Ray Analysis (EDX), also referred to as EDS, is an x-ray technique used to evaluate the elemental/compound composition of materials. The EDX system used was attached to an SEM instrument (FIB-SEM, Auriga from Carl Zeiss), where the imaging capability of the microscope identified the specimen of interest. EDS makes use of the X-ray spectrum emitted by a solid sample bombarded with a focused beam of electrons to obtain a localized chemical analysis. X-ray intensities are measured by counting photons and the precision obtainable is limited by statistical error. For major elements, it is not always difficult to obtain a precision (defined as 2σ) of better than ± 1% (relative), but the overall analytical accuracy is commonly nearer to 2%, due to, but not limited to, uncertainties in the composition of the standards and errors in the various corrections that need to be applied to the raw data. A Horiba LA-950 particle size analyser with a detection range of 0.01 to 3000 µm was used to conduct the analysis of particle size. The Horiba LA-950 particle size analyser uses the laser diffraction method to measure size distributions. In the laser diffraction (LD) method, the detection and analysis of the angular distribution of dispersed light produced by a laser beam passing through a dilute dispersion of particles are directly related to their size. The Mie scattering theory used allows the conversion from the distribution of intensity (scattered light energy) to volume measurements to be carried out.

3.4.4 Surface area and porosity analysis

To determine the surface area and porosity of nanocomposites before and after adsorption, Brunauer-Emmett-Teller (BET) technique was used. Surface areas of synthesised

nanocomposites and product sludge were analysed using a sample degassing system (Micromeritics Tri-Star II, Surface area and porosity, Poretech CC, USA). BET was equipped with micromeritics VacPrep 061 for determination of specific surface areas and porosity of feed and sludge product materials by using liquid nitrogen of temperature -195.800˚C or 77.35K as an analysis bath. The absolute pressure measurement range for the instrument is 0 to 50 mmHg with a resolution within 0.05 mm Hg, accuracy within 0.5% and linearity within 0.25% of full scale. Prior to analysis, the samples were degassed to remove moisture adsorbed to the particle surfaces at a temperature of 100°C for 20 hours in a degassing system in conjunction with vacuum in the Micromeritics Tri-Star II VacPrep 061 sample preparation device, Poretech CC, USA. A helium gas pycnometer (AccuPyc II 1340) from Micromeritics was used to measure the densities of the samples at a controlled room temperature of 25°C. This analytical technique uses a gas displacement method to measure the volume accurately. Instrument analysis reproducibility is typically within ± 0.01% of the nominal full-scale cell chamber volume, with accuracy within 0.03% of reading, plus 0.03% of sample capacity. Helium gas was used as the displacement medium for this study.

3.4.5 Thermal stability analysis

To determine the thermal stability of the nanocomposite materials before and after adsorption, a thermogravimetric analysis (TGA) equioment was used (TGA Q500, TA instrument). The equipment was operated under atmospheric air with a flow rate of 50 mL/min and a heating rate of 10˚C/min.

3.4.6 Compound composition analysis

For determination of compound composition of the nanocomposites before and after adsorption, X-ray fluorescence (XRF) (Thermo Fisher ARL-9400 XP+ Sequential XRF with WinXRF software) was used. A sample was weighed as 3g in a crucible and degassed for 24 hours to remove any humidity and volatile compounds. Thereafter, it was weighed to check the weight loss. After mass evaluation, compound composition was determined using the software.

3.5 Optimization of adsorption experiment parameters

All adsorption experiments were conducted on magnetic stirrers and thermal orbital shaker/incubator in 250 mL Erlenmeyer glass flasks at agitation speed of 250 rpm. A batch experimental approach was adopted for the adsorption of As(V), Cr(VI) and CR dye onto PDFe/Al nanocomposite (adsorbent) where effects of initial concentration, initial pH, dosage of the adsorbent, agitation time and temperature were studied. All the experiments were carried out in triplicates and the data was reported as mean. A summary of the studied experimental parameters is shown in Table 6.

Table 6: Summary of studied parameters for adsorption study

Experiment	Initial As(V) concentration (mg/L)	Initial pH of solution	Dosage of PDFe/Al nanocomposite (g)	Agitation time (min)	Temperature (º C)
Arsenate (As^{5+})					
1	1; 5; 10; 20; 30; 40; 50; 100; 150; 200; 250; 300; 350; 400	7 – 8	1	90	25
2	10	2, 3, 4, 5, 6, 7, 8, 9, 10 (±0.2)	1	90	25
3	10	7 – 8	0.1; 0.5; 1; 2; 3; 4; 5 (±0.0005)	90	25
4	10	7 – 8	1	10; 30; 60; 90; 120; 180; 240; 300	25
5	10	7 – 8	1	90	25; 35; 45; 55; 65
Hexavalent Chromium (Cr^{6+})					
1	1; 5; 10; 20; 30; 40; 50; 100; 150; 200; 250; 300; 350; 400	4 – 5	3	90	25
2	10	2, 3, 4, 5, 6, 7, 8, 9, 10 (±0.2)	3	90	25

3	10	4 – 5	0.1; 0.5; 1; 2; 3; 4; 5 (±0.0005)	90	25
4	10	4 – 5	3	10; 30; 60; 90; 120; 180; 240; 300	25
5	10	4 – 5	3	90	25; 35; 45; 55; 65
Congo Red dye					
1	1; 5; 10; 20; 30; 40; 50; 100; 150; 200 250; 300; 350; 400	6 – 7	1	30	25
2	10	2, 3, 4, 5, 6, 7, 8, 9, 10 (±0.2)	1	30	25
3	10	6 – 7	0.1; 0.5; 1; 2; 3; 4; 5 (±0.0005)	30	25
4	10	6 – 7	1	1; 5; 10; 15; 20; 25; 30; 40; 50; 60	25
5	10	6 – 7	1	30	25; 35; 45; 55; 65

3.5.1 Effect of agitation time

To investigate the effect of agitation time, volumes of 250 mL of 10 mg/L As(V), Cr(VI) and CR were pipetted into conical flasks into which 1 g of the adsorbent sample was added. The mixtures were then agitated under room temperature at different time intervals as indicated in Table 6 at a speed of 250 rpm. Concentrations of As(V), Cr(VI) and CR, before and after agitation, were measured as indicated in 3.3.

3.5.2 Effect of dosage

To investigate the effect of adsorbent dosage, volumes of 250 mL of 10 mg/L As(V), Cr(VI) and CR were pipetted into conical flasks and varying masses (0.1 - 5 g) of the adsorbent were added into individual flasks. The mixtures were agitated using a shaker for an optimum time of 90, 240 and 30 mins for As(V), Cr(VI) and CR, respectively, at 250 rpm under room temperature. Concentrations of As(V), Cr(VI) and CR, before and after agitation, were measured as indicated in 3.3.

3.5.3 Effect of solution pH

To investigate the effect of pH, volumes of 250 mL of 10 mg/L As(V), Cr(VI) and CR were pipetted into conical flasks and the pH of the solution was adjusted from 1 – 10, optimum dosage of adsorbent was added into each flask, as per desired pH. The mixtures were agitated using a shaker at optimum established at 250 rpm under room temperature. Concentrations of As(V), Cr(VI) and CR, before and after agitation, were measured as indicated in 3.3.

3.5.4 Effect of temperature

To investigate the effect of temperature, volumes of 250 mL of 10 mg/L As(V), Cr(VI) and CR were pipetted into conical flasks and solution temperature was adjusted from 25 – 65 °C and optimum dosage of adsorbent was added into each flask. The mixtures were agitated at optimum established time at 250 rpm. Concentrations of As(V), Cr(VI) and CR, before and after agitation, were measured as indicated in 3.3.

3.5.5 Effect of species concentration

To investigate the effects of adsorbate concentration on reaction kinetics, several dilutions were made from the simulated adsorbate stock solutions. The capacity of the adsorbent to remove the adsorbate ions from aqueous solution were then assessed by measuring As(V), Cr(VI) and CR concentrations. Solutions of varying concentrations as indicated in Table 6 were prepared and optimum dosages of adsorbent were added to each sample container. The mixtures were agitated at optimum established time at 250 rpm under room temperature. Concentrations of As(V), Cr(VI) and CR, before and after agitation, were measured as indicated in 3.3.

3.6 Adsorption at optimized conditions

Arsenic, chromium and Congo red effluents emanating from gold, chrome and printing company, respectively, were treated at established optimized conditions in order to assess the effectiveness of synthesized PDFe/Al nanocomposite. The final concentrations were determined as described previously. After agitating PDFe/Al nanocomposite with the effluents, the resultant residues were characterized to gain an insight into the fates of chemical species of PDFe/Al nanocomposite.

3.7 Desorption and regeneration studies

To study the regeneration of the PDFe/Al nanocomposite, a method described by Kumari et al. (2006) was applied. A batch experiment was conducted where optimum dosage of PDFe/Al nanocomposite was agitated with 250 mL of maximum concentration in a 250 mL Erlenmeyer flask for optimum agitation time. After equilibration, the residue was separated from the supernatant via centrifugation. The recovered residue material was then washed five times with 250 mL ultra-pure water to remove excess adsorbate ions, and then dried. Thereafter, the dried sample was mixed with 250 mL of 0.1 M HNO_3 under room temperature. The resultant HNO_3 extract was collected and analysed for adsorbate ions. The regeneration efficiency was determined using equation 3.1.

$$\text{Regeneration efficiency} = \frac{C_{des}}{C_{ads}} \times 100 \qquad (3.1)$$

Where; C_{des} is the concentration of adsorbate ions in the desorption eluent (mg/L); C_{ads} is the concentration of adsorbate ions adsorbed by PDFe/Al nanocomposite (mg/L).

3.8 Determination of Point of Zero Charge (PZC)

In studying and determining the point of zero charge (PZC) of the adsorbent (PDFe/Al nanocomposite), a method described by Smičiklas et al. (2000) was adopted and applied. A volume of 50 mL of 0.1 M KNO_3 solution was transferred into individual flasks. The initial pH values of the solutions were adjusted to 2 – 10 using 0.1 M HNO_3 and NaOH. Thereafter, 0.1 g of PDFe/Al nanocomposite was added into each flask and the mixtures were left allowed to equilibrate for 24 h at ± 25 ºC. The PDFe/Al nanocomposite suspensions were then separated from the solutions, and the final pH values were recorded. The difference between initial and final pH (pH_f) values ($\Delta pH = pH_i - pH_f$) was plotted against pH_i. The point of intersection of the resulting curve with abscissa, at which $\Delta pH=0$, was taken as the point of zero charge.

3.9 Mathematical modelling

3.9.1 Modelling of adsorbate removal and adsorption capacity

The adsorption capacity of PDFe/Al nanocomposite and percentage removal of As(V), Cr(VI) and CR from aqueous solution was evaluated by equations 3.2 and 3.3 respectively.

$$q_e = \frac{(C_0 - C_e).V}{m} \quad (3.2)$$

$$\% \text{ Removal} = \frac{C_0 - C_e}{C_0} \times 100 \quad (3.3)$$

Where; q_e is the amount of adsorbate adsorbed on PDFe/Al nanocomposite (mg/g); C_0 is the initial adsorbate concentration (mg/L); C_e is the equilibrium adsorbate concentration (mg/L); V is the volume of the solution (mL); m is the mass of PDFe/Al nanocomposite (g)

3.9.2 Adsorption Kinetics

Adsorption kinetics was evaluated using pseudo-first-order, second order kinetics and Intraparticle diffusion model by Weber Morris (Tran et al., 2017, Ho et al., 2005, Ho and McKay, 1999, Ho et al., 2000).

3.9.2.1 Pseudo-first-order kinetic

A Lagergren pseudo first order kinetic model is a well-known model that is used to describe mechanisms of metal species adsorption by an adsorbent. It can be written as follows (Lagergren, 1898):

$$\log(q_e - q_t) = -\frac{k_1 t}{2.303} + \log q_e \qquad (3.4)$$

Where k_1 (min^{-1}) is the pseudo-first-order adsorption rate coefficient and q_e and q_t are the values of the amount adsorbed per unit mass at equilibrium and at time t, respectively. A plot of $\log(q_e - q_t)$ versus t determines the values of k_1 and q_e.

3.9.2.2 Pseudo-second-order kinetic

Pseudo-second-order kinetic model is another kinetic model that is widely used to describe the adsorption mechanism from an aqueous solution. The linearized form of the pseudo-second-order rate equation can be written as follows (Ho and McKay, 1999):

$$\frac{t}{q_t} = \frac{t}{q_e} + \frac{1}{k_2 q_e^2} \qquad (3.5)$$

Where k_2 [g (mg min^{-1})] is the pseudo-second-order adsorption rate coefficient and q_e and q_t are the values of the amount adsorbed per unit mass at equilibrium and at time t, respectively. A plot of $\frac{t}{q_t}$ versus t determines the values of k_2 and q_e.

3.9.2.3 Intra-particle diffusion model

Pollutants adsorption may also be governed by diffusional processes as well as kinetics between the adsorbent and adsorbate. In diffusion studies, the rate is often expressed in terms of the square root time as denoted below (Weber and Morris, 1963):

$$q_t = k_{id}t^{1/2} + C_i \quad (3.6)$$

Where k_{id} (mgg^{-1} $min^{-1/2}$) is the Intra-particle diffusion coefficient (slope of the plot of q_t versus $t^{1/2}$) and C_i is the Intraparticle diffusion rate constant. Parameters were calculated to determine whether film diffusion or Intra-particle diffusion is the rate limiting step. The model suggests if the sorption mechanism is via Intra-particle diffusion when a plot of q_t versus $t^{1/2}$ will be linear; and Intraparticle diffusion is the sole rate-limiting step when such a plot passes through the origin. When the sorption process is controlled by more than one mechanism, then a plot of q_t versus $t^{1/2}$ will be multi-linear (Tran et al., 2017, Weber and Morris, 1963).

3.10 Adsorption isotherms and thermodynamics

Adsorption isotherms were evaluated using the most popular models and they include: Langmuir and Freundlich adsorption isotherms (Tran et al., 2017, Lima, 2015).

3.10.1 Langmuir adsorption isotherm

The most important model of monolayer adsorption was developed by Langmuir. This isotherm may be denoted by the undermentioned equation:

$$q_e = \frac{Q_0 b C_e}{1+bC_e} \quad (3.7)$$

The constant Q_0 and b are characteristics of the Langmuir equation and can be determined from a linearized form of equation 7. The Langmuir isotherm is valid for monolayer sorption due to a surface with finite number of identical sites and can be expressed in the following linear form (Langmuir, 1916):

$$\frac{Ce}{q_e} = \frac{1}{Q_0 b} + \frac{Ce}{Q_m} \quad (3.8)$$

The essential characteristics of the Langmuir isotherm can be expressed in terms of a dimensionless constant separation factor or equilibrium parameter, R_L, which can be determined by the following equation:

$$R_L = \frac{1}{1+bC_o} \quad (3.9)$$

Where, Ce = equilibrium concentration (mg L^{-1}), qe = amount adsorbed at equilibrium (mg g^{-1}), q_m = Langmuir constants related to adsorption capacity (mg g^{-1}) and b = Langmuir constants related to energy of adsorption (L mg^{-1}). A plot of Ce versus Ce/Qe should be linear if the data conforms to the Langmuir isotherm. The value of Qm is determined from the slope and the intercept of the plot. It is used to derive the maximum adsorption capacity and b is determined from the original equation and represents the degree of adsorption.

3.10.2 Freundlich adsorption isotherm

The Freundlich adsorption isotherm describes the heterogeneous surface energy by multilayer adsorption. The Freundlich isotherm is formulated as follows:

$$q_e = kC_e^{1/n} \quad (3.10)$$

The equation may be linearized by taking the logarithm of both sides of the equation and can be expressed in linear form as follows (Freundlich, 1906):

$$\log q_e = n \log C_e + \log k_f \quad (3.11)$$

Where Ce = equilibrium concentration (mg L^{-1}), q_e = amount adsorbed at equilibrium (mg g^{-1}), K = Partition Coefficient (mg g^{-1}) and n = degree of adsorption. A linear plot of log Ce versus log q_e indicates whether the data is described by the Freundlich isotherm. The value of K implies that the energy of adsorption on a homogeneous surface is independent of surface coverage, and n is an adsorption constant which reveals the rate at which adsorption is taking place.

3.11 Thermodynamics

In order to fully understand the nature of adsorption, the thermodynamic parameters such as free energy change (ΔG) can be calculated. It is possible to estimate these thermodynamic parameters for adsorption reaction by considering the equilibrium constant under the experimental conditions. The Gibbs free energy change of adsorption was calculated using the following equation:

$$\Delta G^{\circ} = -RT \ln K_c \quad (3.12)$$

Where, R is gas constant (8.314 J mg^{-1} K^{-1}), T is temperature in Kelvin and Kc is the equilibrium constant. The negative ΔG° value indicates that the sorption process is spontaneous in nature, whereas the positive value indicates that the reaction is non-spontaneous.

Percentage removal and adsorption capacity of CR by calcined cryptocrystalline magnesite/Ca-bentonite clay nanocomposite were evaluated using equations (3.1) and (3.2)

$$\text{Percentage removal (\%)} = \left(\frac{C_i - C_e}{C_i}\right) \times 100 \quad (3.13)$$

$$\text{Adsorption capacity } (q_e) = \frac{(C_i - C_e)V}{m} \quad (3.14)$$

Where: C_i = initial CR concentration, Ce = equilibrium CR concentration, V = volume of solution; m = mass of the feedstock.

References

FREUNDLICH, H. 1906. Over the adsorption in solution. *Zeitschrift fur Physikalische Chemie,* 57**,** 385-470.

HILLIER, S., MARWA, E. & RISE, C. 2013. On the mechanism of exfoliation of "vermiculite" clay minerals. *Clay Miner,* 48**,** 563-582.

HO, Y. S., CHIU, W. T. & WANG, C. C. 2005. Regression analysis for the sorption isotherms of basic dyes on sugarcane dust. *Bioresource Technology,* 96**,** 1285-1291.

HO, Y. S. & MCKAY, G. 1999. Pseudo-second order model for sorption processes. *Process Biochemistry,* 34**,** 451-465.

HO, Y. S., NG, J. C. Y. & MCKAY, G. 2000. Kinetics of pollutant sorption by biosorbents: Review. *Separation and Purification Methods,* 29**,** 189-232.

KUMARI, P., SHARMA, P., SRIVASTAVA, S. & SRIVASTAVA, M. M. 2006. Biosorption studies on shelled Moringa oleifera Lamarck seed powder: Removal and recovery of arsenic from aqueous system. *International Journal of Mineral Processing,* 78**,** 131-139.

LAGERGREN, S. 1898. About the theory of so-called adsorption of soluble substances. *Handlingar,* 24**,** 1-39.

LANGMUIR, I. 1916. The constitution and fundamental properties of solids and liquids. Part I. Solids. *The Journal of the American Chemical Society,* 38**,** 2221-2295.

LIMA, E. C. A., M.A. MACHADO, F.M. 2015. Kinetic and equilibrium models of adsorption. *In:* BERGMANN, C. P. M., F.M. (ed.) *Carbon nanomaterials as adsorbents for environmental and biological applications.* Switzerland: Springer International publishing.

SMIČIKLAS, I. D., MILONJIĆ, S. K., PFENDT, P. & RAIČEVIĆ, S. 2000. The point of zero charge and sorption of cadmium (II) and strontium (II) ions on synthetic hydroxyapatite. *Separation and Purification Technology,* 18**,** 185-194.

TRAN, H. N., YOU, S.-J., HOSSEINI-BANDEGHARAEI, A. & CHAO, H.-P. 2017. Mistakes and inconsistencies regarding adsorption of contaminants from aqueous solutions: A critical review. *Water Research,* 120**,** 88-116.

WEBER, W. J. & MORRIS, J. C. 1963. Kinetics of adsorption on carbon from solution. *J. Sanit. Eng. Div. Am. Soc. Civ. Eng.,* 89**,** 31-59.

CHAPTER FOUR

ADSORBENT MATERIAL SYNTHESIS AND CHARACTERISATION

4.0 Introduction

This chapter seeks to outline the processes involved in the synthesis of the adsorbent (PDFe/Al nanocomposite). It also provided the general characterization of the synthesized raw material such as XRD, XRF, SEM, BET, TGA and FTIR.

4.1 Synthesis and recovery of PDFe/Al nanocomposite from authentic AMD

During selective precipitation, as outlined in 3.2, polycationic di-metal Fe/Al nanocomposite was formed. Sodium hydroxide exchanges OH^- ions with Fe^{3+} /Al^{3+}, thereby forming $Fe/Al(OH)_3$.

The experimental value was E^0_{exp} = + 0.940 V. This value is in agreement with the Pourbaix (stability) diagrams of iron and aluminium (Figure 4.1). Moreover, $Fe(OH)_3$ and $Al(OH)_3$ commence to precipitate at pH > 2.

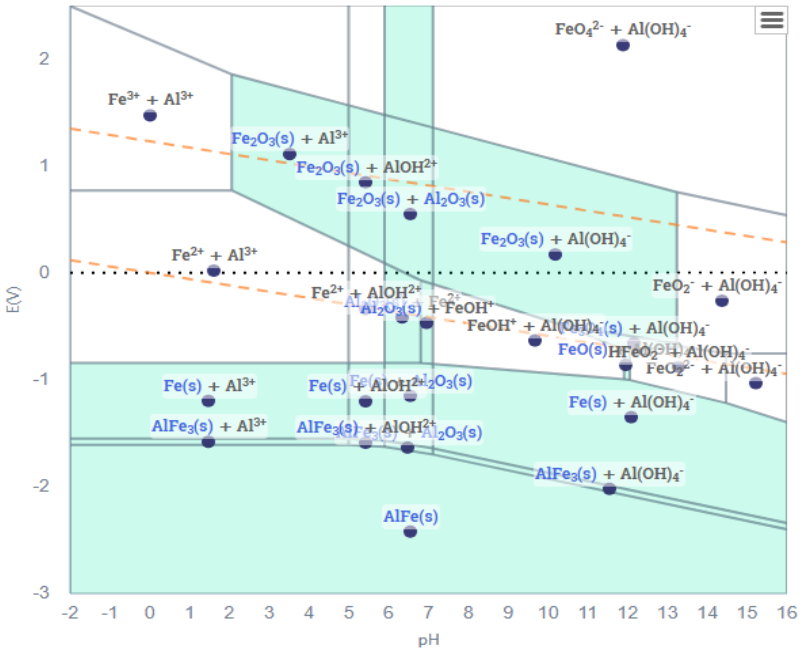

Figure 4.1: Combined Iron and aluminium Pourbaix (stability) diagrams (Persson et al., 2012)

Relationship between temperature and time during the synthesis of PDFe/Al from authentic AMD is shown in Figure 4.2.

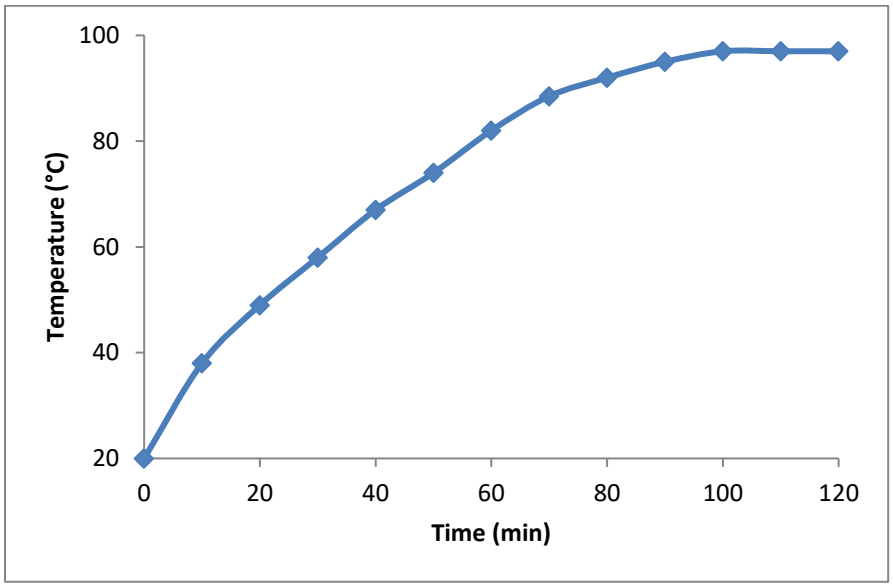

Figure 4.2: Relationship between temperature and time during the synthesis of PDFe/Al nanocomposite from authentic AMD

From Figure 4.2, it can be seen that molecules and particles in AMD slowly gain kinetic energy between 20 ºC and 75 ºC. A decrease in the heating rate is however observed after 80ºC, which means that though the number of collisions increases, the rate of temperature increase starts to slow down. As particles continue absorbing heat with time when temperature increases in the system, they start moving faster and kinetic energy increases, thus could be denoting an endothermic reaction as more heat is absorbed by the particles. The rate at which particles collide increased and led to coagulation of small particles which formed agglomerates of poly-cationic di-metal nanocomposites with high surface area and pore volume. This was due to the precipitation of metal cations during neutralisation of acid mine drainage. This behaviour is also in agreement with the Le Chatelier's principle and Collision theory because the reaction favoured the formation of products. After drying of the recovered material at room temperature, the product was calcined and ball milled.

Several studies show that iron oxide and aluminium oxide are mostly synthesised from synthetic chemicals. Pehlivan et al. (2019) used synthetic aluminium nitrate nonahydrate and iron nitrate nonahydrate to synthesise Al_2O_3 and Fe_2O_3 through solution combustion. Braga et al. (2010)

synthesised aluminium oxide/iron oxide by mixing chitosan and iron and aluminium hydroxides through dissolution and continuous stirring. Hübner et al. (2017) synthesised aluminium/iron oxide/hydroxide nanothermite compounds via co-precipitation of synthetic iron (III) chloride hexahydrate in the presence of spherical aluminium nanoparticles (Al/Al_2O_3).

4.2 Characterization of raw materials

4.2.1 Functional groups

Fourier Transform Infrared Spectrometer (FTIR) was used to determine the functional groups of raw PDFe/Al nanocomposite as shown figure 4.3.

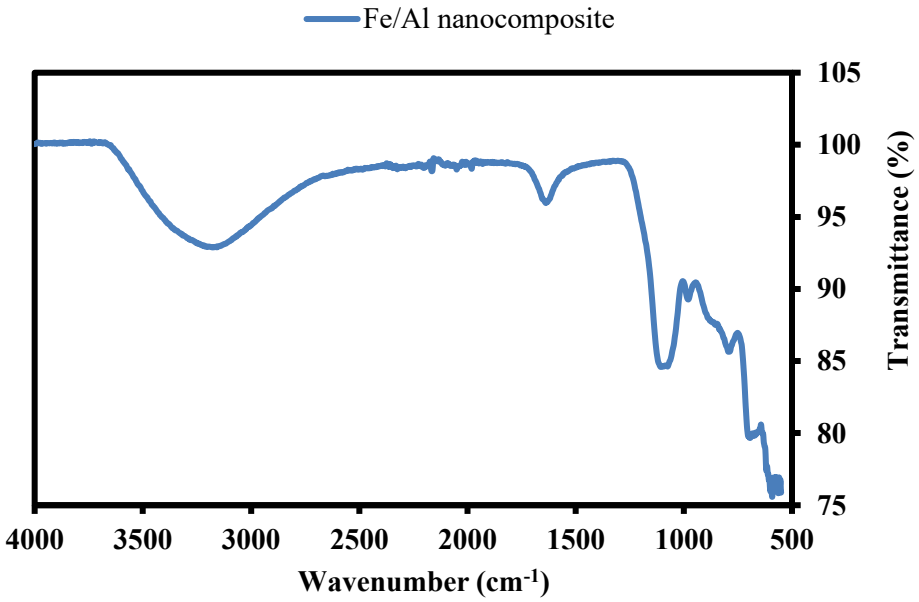

Figure 4.3: Functional groups of raw PDFe/Al nanocomposite

From figure 4.3, the bands of raw PDFe/Al nanocomposite are shown. The bands between 4000 –3500 cm^{-1} can be an illustration of the high stretching of O-H for the two bands. The adsorption band at 1668 cm^{-1} could be an indication of the stretching of HOH which further increased at 1113 cm^{-1}. Functional groups are summarised in table 7.

Table 7: Functional groups and their respective wavenumbers in PDFe/Al nanocomposite

Functional group	Wavenumber (cm^{-1})	Reference
O-H	4000 –3500	(Bordoloi, Nath, Gogoi, & Dutta, 2013)
HOH	1668	(Bordoloi, Nath, Gogoi, & Dutta, 2013)
	1113	(Bordoloi, Nath, Gogoi, & Dutta, 2013)

4.2.2 Mineralogical composition

X-ray diffraction (XRD) patterns for the synthesized raw PDFe/Al nanocomposite are shown in Figure 4.4.

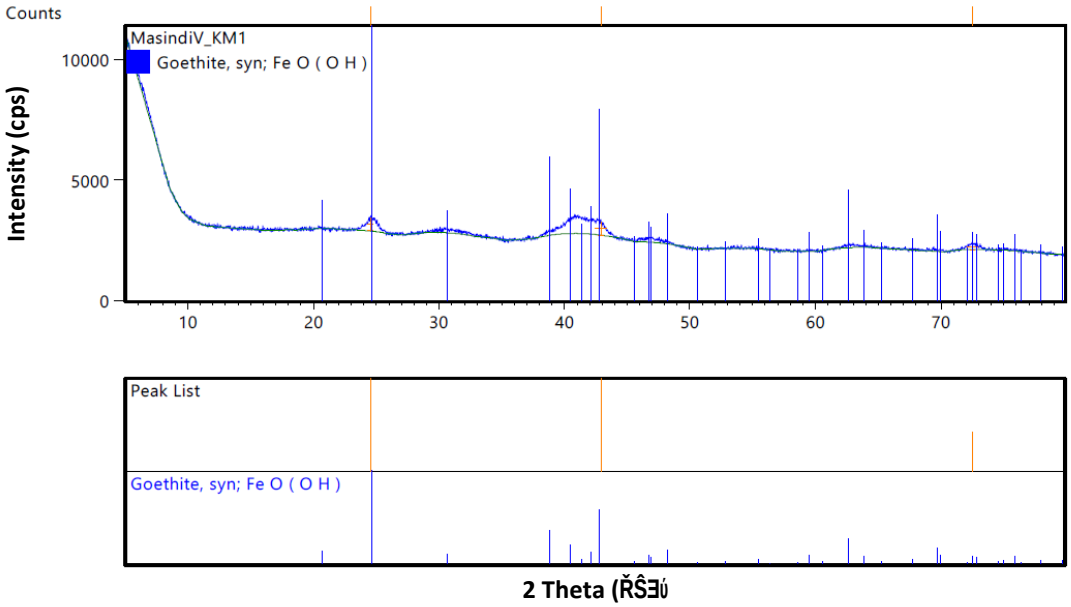

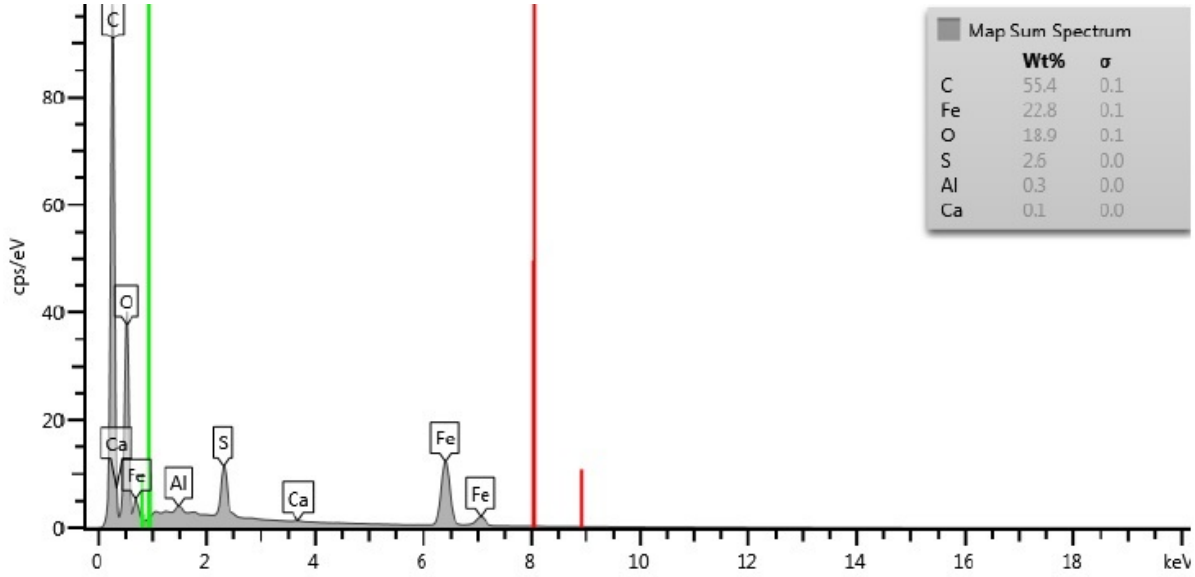

Figure 4.4: X-ray diffraction (XRD) patterns for the synthesized PDFe/Al nanocomposite

From figure 4.4, it can be noted that the recovered and synthesised PDFe/Al nanocomposite is showing the presence of goethite FeO(OH) as the dominant species, with clear peaks showing the crystalline nature of the material, as well as a bit of amorphous. These XRD results show significant crystalline phases which could have been formed at the surface sites. Iron and aluminium are shown to be present in the raw material.

4.2.3 Compound composition

X-ray fluorescence (XRF) was used to determine the compound composition of raw PDFe/Al nanocomposite. Table 8 shows the results for compound composition of XRF characterisation.

Table 8: Compound composition of raw PDFe/Al nanocomposite

Compound	Certified	Analysed	PDFe/Al Nanocomposite
SiO_2	**99.6**	99.70	0.16
TiO_2	**0.01**	0.00	<0,01
Al_2O_3	**0.05**	0.01	1.15
Fe_2O_3	**0.05**	0.01	58.80
MnO	**0.01**	0.00	0.05
MgO	**0.05**	0.01	0.23

CaO	**0.01**	0.01	0.17
Na_2O	**0.05**	0.02	0.38
K_2O	**0.01**	0.01	<0,01
P_2O_5	**0**	0.03	<0,01
Cr_2O_3	**0**	0.00	<0,01
NiO	**0**	0.01	<0,01
ZrO_2	**0**	0.01	<0,01
SO_3	**0**	0.00	0.38
WO_3	**0**	0.00	0.03
CuO	**0**	0.00	<0,01
Co_3O_4	**0**	0.00	0.03
SrO	**0**	0.00	<0,01
LOI	**0**	0.10	38.60
Total	**100**	**99.94**	**99.98**

As shown in table 8, iron is the most dominant species in the synthesised PDFe/Al nanocomposite, followed by aluminium. The other components, such as Si and SO_3 are impurities which resulted from the co-precipitation and co-adsorption process from acid mine drainage (Masindi et al., 2018).

4.2.4 Morphology

Scanning Electron Micrographs (SEM-EDX) was used to determine the morphology of raw PDFe/Al nanocomposite as illustrated in Figure 4.5.

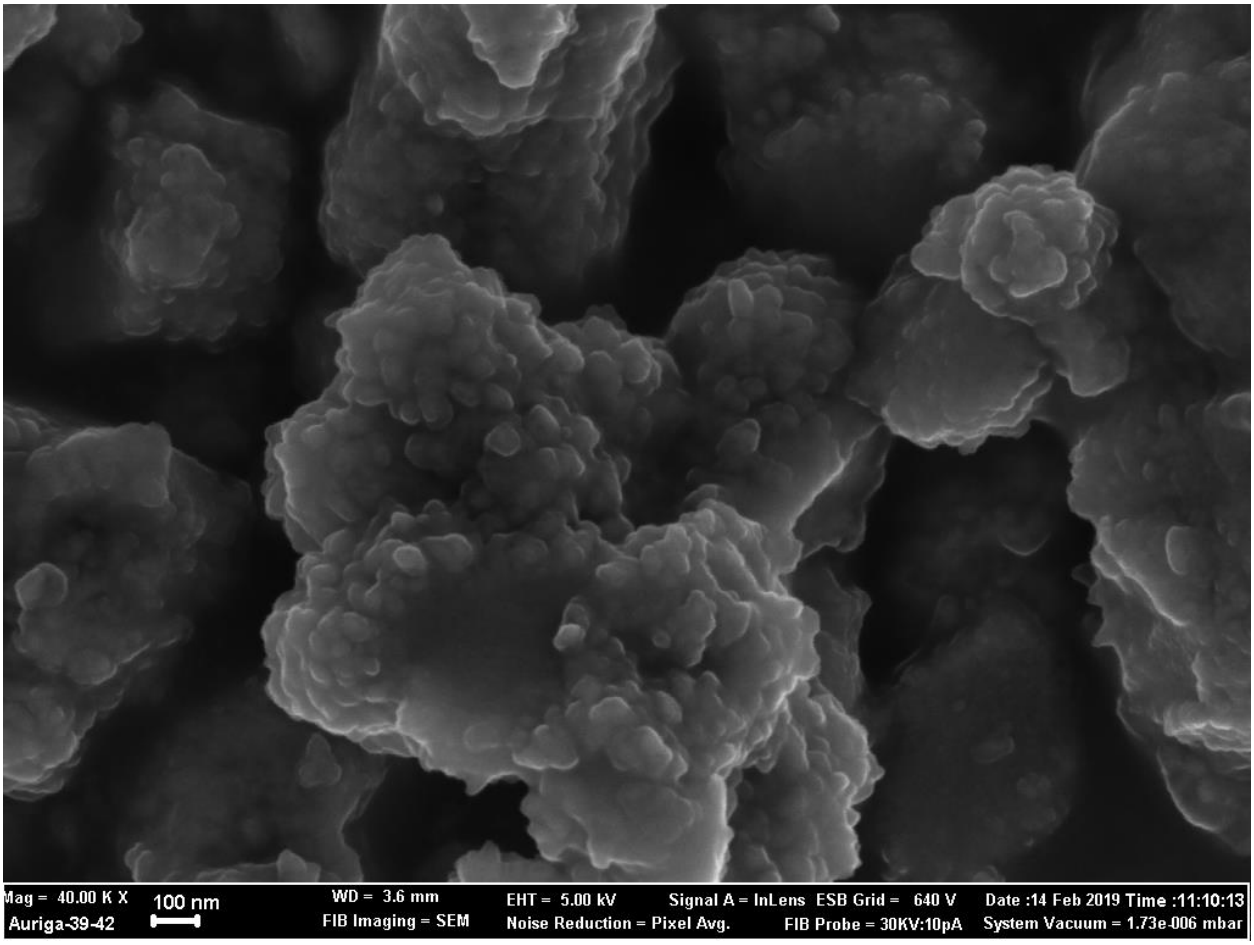

Figure 4.5: SEM images for the raw synthesized PDFe/Al nanocomposite

Figure 4.5 shows the visual structure of PDFe/Al nanocomposite. The materials have non-uniform shapes with uneven distribution of irregular agglomerates. The light structures could be an indication of the presence of aluminium hydroxide and the dark structures show the presence of ferric hydroxide.

4.2.5 EDX Mapping

The mapping of PDFe/Al nanocomposite was done to determine the relative distribution of elements on the adsorbent surface as shown in figure 4.6.

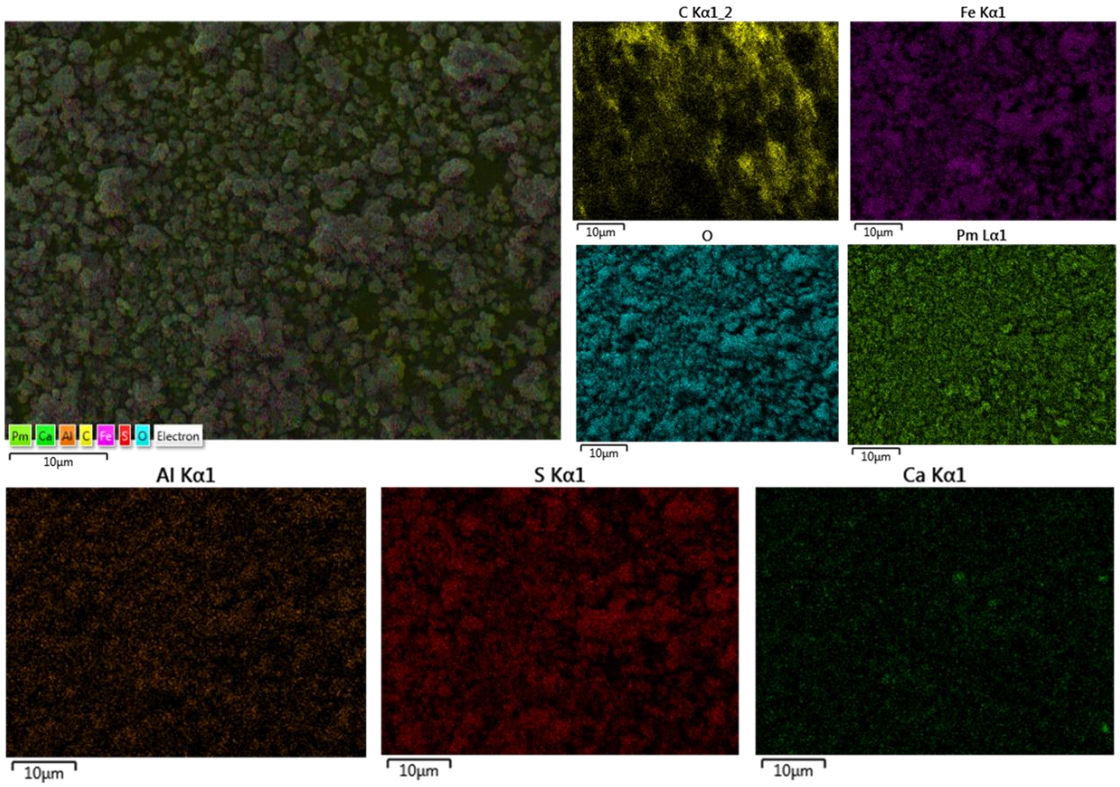

Figure 4.6: Mapping of raw PDFe/Al nanocomposite

As shown in Figure 4.6, Fe and Al are present in the synthesised PDFe/Al nanocomposite in a uniform and even distribution which shows dominance. The presence of S and Ca are some of the impurities from AMD. The presence of O shows the oxide part of the adsorbent. From the main structure (top left), reflections of Fe and Al are observed.

4.2.6 Thermal analysis

Thermo Gravimetric Analyser (TGA) was used to evaluate the thermal stability of raw PDFe/Al nanocomposite as illustrated in Figure 4.7.

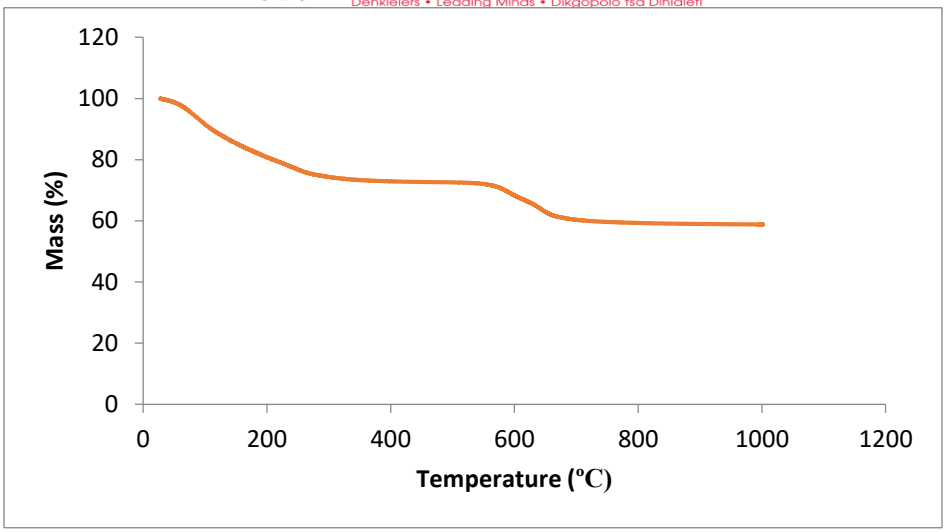

Figure 4.7: Thermal stability of raw PDFe/Al nanocomposite

From figure 4.7, the thermal stability of raw PDFe/Al nanocomposite is observed. After 100 ºC, the compound starts losing a lot of moisture. This can mean that the OH group is removed from the material. The declining trends could be an indication of decomposition of the materials. (Wei et al., 2016) also reported a temperature of 150 ºC as being the maximum temperature before the state of Fe/Al interface could change as further heating changes the chemical structure of the material.

4.6.7 Surface area and porosity

Brunauer-Emmet-Teller (BET) was used to characterise the surface area, pore size and pore volume of raw PDFe/Al nanocomposite as illustrated in Table 9.

Table 9: BET characterisation of raw PDFe/Al nanocomposite

Sample	BET surface area (m^2/g)	Pore volume (cm^3/g)	Pore size (nm)
PDFe/Al nanocomposite	24.6275	0.042334	8.58545

Table 9 shows the surface area, pore size and pore volume of PDFe/Al nanocomposite. The synthesised PDFe/Al nanocomposite has pore size of 8.58545 nm which can be proof that the material is a mesoporous nanocomposite material as its pore size falls within the range of 2 – 50 nm (IUPAC, 1997). Some studies (Jeong et al., 2007, Han et al., 2016) have reported on low

surface areas for Fe_2O_3 and Al_2O_3 to be 5.05 and 0.50 m^2/g, and 0.55 and 2.35 m^2/g, respectively. The materials were also reported to be mesoporous (Jeong et al., 2007). However, some studies (He et al., 2017, Chitrakar et al., 2011) reported high surface areas of Fe-Al materials of 47 – 134 m^2/g.

4.7 Conclusions

The synthesised PDFe/Al nanocomposite showed unique characteristics, physical and chemical properties. For a material which was synthesised from natural AMD, this shows that natural sources can provide very useful resources or adsorbents for wastewater treatment. Characterisation of the adsorbent showed that Fe is more dominant than Al.

References

BRAGA, T. P., VASCONCELOS, I. F., SASAKI, J. M., FABRIS, J. D., DE OLIVEIRA, D. Q. L. & VALENTINI, A. 2010. Magnetic composites based on hybrid spheres of aluminum oxide and superparamagnetic nanoparticles of iron oxides. *Journal of Magnetism and Magnetic Materials,* 322**,** 633-637.

CHITRAKAR, R., MAKITA, Y., SONODA, A. & HIROTSU, T. 2011. Fe–Al layered double hydroxides in bromate reduction: Synthesis and reactivity. *Journal of Colloid and Interface Science,* 354**,** 798-803.

HAN, W., FU, F., CHENG, Z., TANG, B. & WU, S. 2016. Studies on the optimum conditions using acid-washed zero-valent iron/aluminum mixtures in permeable reactive barriers for the removal of different heavy metal ions from wastewater. *Journal of Hazardous Materials,* 302**,** 437-446.

HE, X., QIU, X. & CHEN, J. 2017. Preparation of Fe(II)–Al layered double hydroxides: Application to the adsorption/reduction of chromium. *Colloids and Surfaces A: Physicochemical and Engineering Aspects,* 516**,** 362-374.

HÜBNER, J., KLAUMÜNZER, M., COMET, M., MARTIN, C., VIDAL, L., SCHÄFER, M., KRYSCHI, C. & SPITZER, D. 2017. Insights into combustion mechanisms of variable aluminum-based iron oxide/-hydroxide nanothermites. *Combustion and Flame,* 184**,** 186-194.

IUPAC. 1997. *Compendium of Chemical Terminology, 2nd ed.* [Online]. Oxford: Blackwell Scientific Publications. Available: http://goldbook.iupac.org [Accessed 2018-03-19].

JEONG, Y., FAN, M., SINGH, S., CHUANG, C.-L., SAHA, B. & HANS VAN LEEUWEN, J. 2007. Evaluation of iron oxide and aluminum oxide as potential arsenic(V) adsorbents. *Chemical Engineering and Processing: Process Intensification,* 46**,** 1030-1039.

PEHLIVAN, M., SIMSEK, S., OZBEK, S. & OZBEK, B. 2019. An extensive study on the synthesis of iron based magnetic aluminium oxide nanocomposites by solution combustion method. *Journal of Materials Research and Technology,* 8**,** 1746-1760.

PERSSON, K. A., WALDWICK, B., LAZIC, P. & CEDER, G. 2012. Prediction of solid-aqueous equilibria: Scheme to combine first-principles calculations of solids with experimental aqueous states. *Physical Review B,* 85.

WEI, Y., SHAO, W., MA, Z., CHEN, Z. & LU, W. 2016. Preparation and thermal stability of an atomically sharp Fe/Al interface. *Materials Letters,* 185**,** 537-540.

CHAPTER FIVE

As(V) ADSORPTION STUDY: RESULTS AND DISCUSSION

5.0 Introduction

This chapter focuses on the evaluation of the efficiency of recovered and synthesised poly-cationic dimetallic Fe/Al nanocomposite on the removal of arsenic (As(V)) from industrial effluents: Evaluation of adsorption kinetics, reaction equilibrium and mechanisms.

5.1 Optimization of adsorption parameters

5.1.1 Effect of initial concentration

The highest As(V) concentration which can be removed from water using PDFe/Al nanocomposite was evaluated, where solutions of different As(V) concentrations (Table 6) were used. The other parameters were fixed, so as to determine the influence of As(V) concentration on the adsorption alone. Figure 5.1 shows the relationship between final As(V) concentration and the studied initial As(V) concentrations.

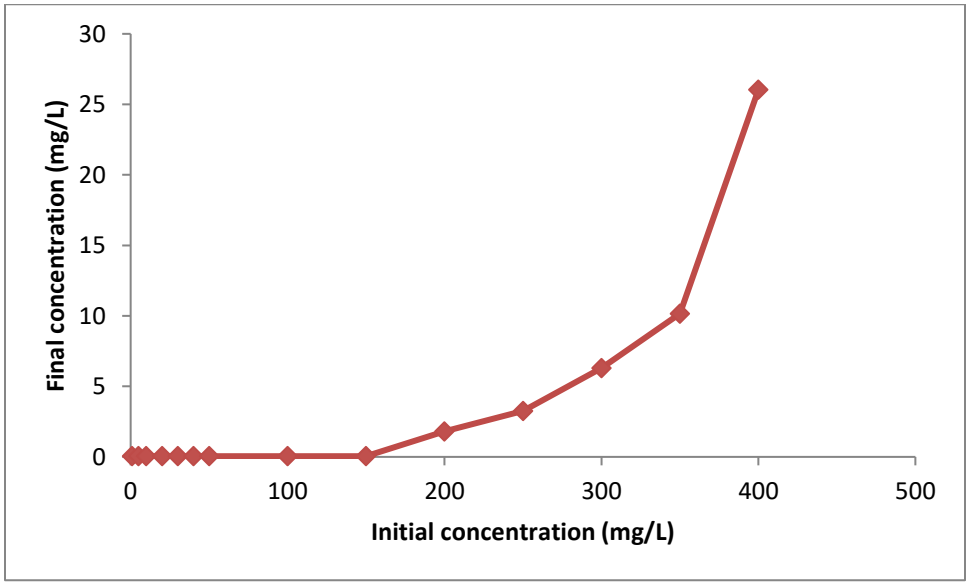

Figure 5.1: Effect of initial As(V) concentration on the removal of As(V)

As shown in figure 5.1, effective complete removal of As(V) from solution by the PDFe/Al nanocomposite was observed for all initial As(V) concentrations up to 150 mg/L. Only at a concentration of 200 mg/L was any As(V) measured in solution, however this concentration was only approximately 1.8 mg/L, implying a removal of 99.1 ± 0.05 %. This implies saturation of the adsorbent was observed at values in excess of 150 mg/L, i.e. the adsorbent did not have enough spaces left to accommodate more As(V) ions. When an adsorbent is saturated with the adsorbate, the rest of the oxyanions, As(V) in this study, are left in solution, hence the decrease in the percentage removal. It can, therefore, be concluded that an initial As(V) concentration of between 150 mg/L to 200 mg/L of initial As(V) concentration, for this study, is the maximum concentration PDFe/Al nanocomposite can accommodate. (Mostafa et al., 2011) reported the optimum concentration being less or equal to 10 mg/L. This study in comparison, demonstrated exceptionally capacity for As(V) adsorption.

5.1.2 Effect of adsorbent dosage

A range of PDFe/Al nanocomposite dosage listed in Table 6 was considered in order to determine the amount of adsorbent which can be used to obtain the highest percentage removal of As(V) from water. Figure 5.2 illustrates the effect of dosage on the removal of As(V).

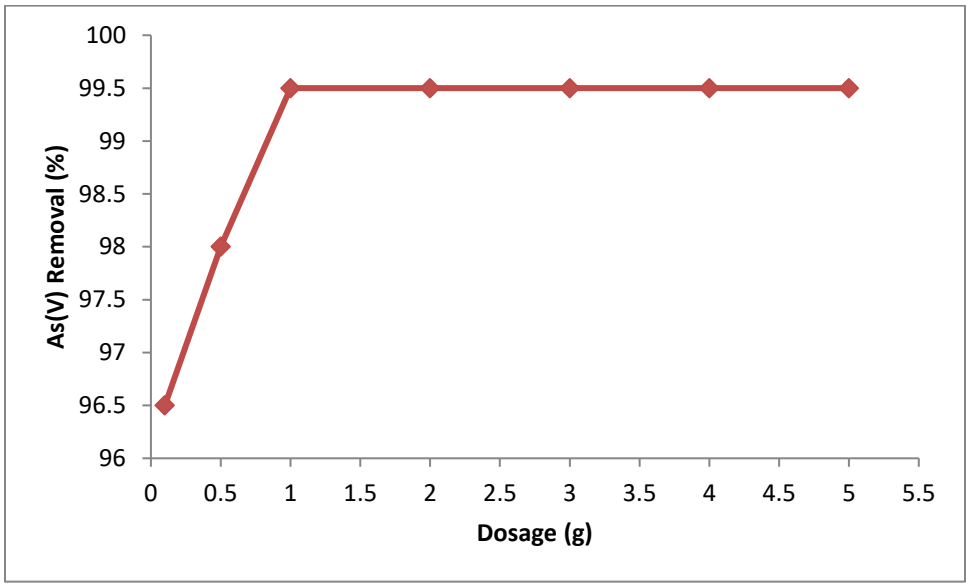

Figure 5.2: Effect of PDFe/Al nanocomposite dosage on the % removal of As(V) from water

Figure 5.3 illustrates the effect of adsorbent (PDFe/Al nanocomposite) on the adsorption capacity (q_e).

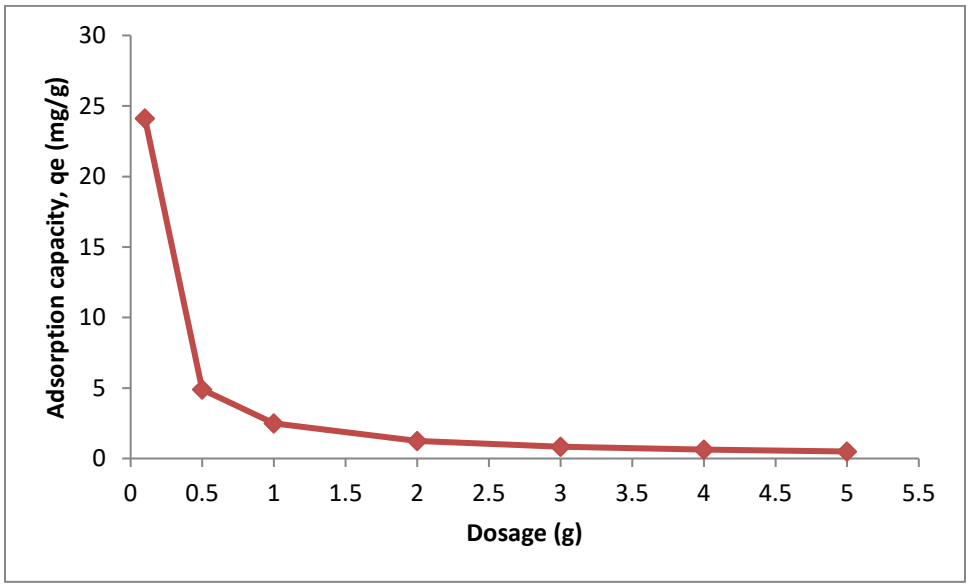

Figure 5.3: Relationship between the adsorption capacity (**q**) and the dosage

From figure 5.2 and figure 5.3, it can be noted that a dosage of adsorbent in excess of 1 g is sufficient to ensure complete removal of As(V) from the system. The % removal of As(V) from water remains constant between 1 g – 5 g, which means that 1 g is sufficient to remove 10 mg/L As(V) ions from 250 mL of aqueous solution. This complete removal indicated by Figure 5.2 indicates that the surface of the adsorbent can accommodate more As(V) oxyanions. Figure 5.3 shows a rapid decrease of adsorption capacity of PDFe/Al nanocomposite between 0.1 g – 1 g. This is because the concentration of As (V) ions is less than the surface area of the adsorbent material can accommodate; the material has vacant pores or spaces not covered by As(V) ions. (Maji et al., 2011) reported a dosage of 15 g iron-oxide-coated natural rock which removed 75 % of a 10 mg/L As(V) solution.

5.1.3 Effect of initial pH

To determine the effect of the initial pH of As(V) solution on the adsorption of As(V) onto PDFe/Al nanocomposite, a range of pH values was considered while fixing the other system parameters listed in Table 6. The effect of initial pH of As(V) solution on the removal of As(V) from water is illustrated in Figure 5.4.

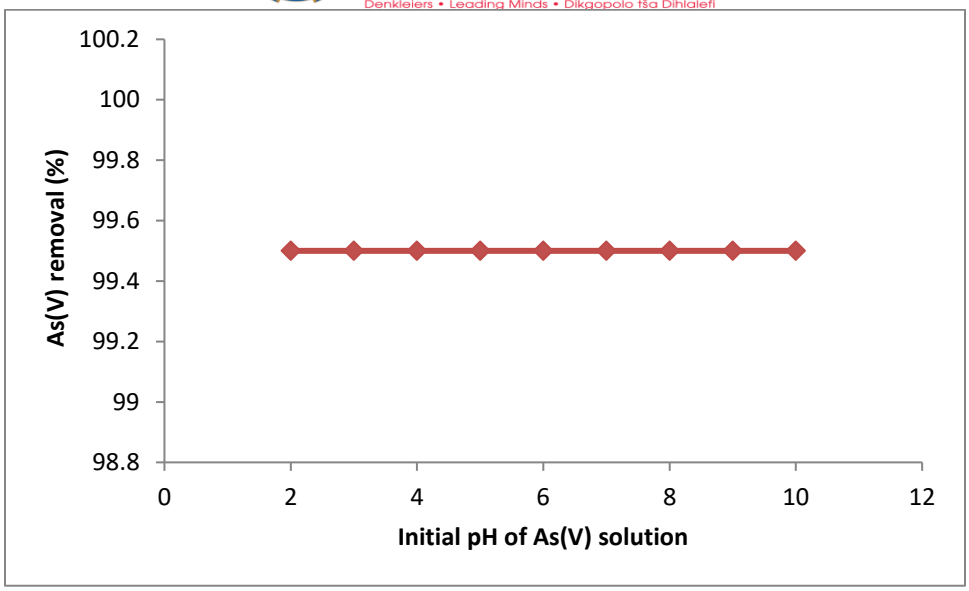

Figure 5.4: Effect of initial pH of As(V) solution on the removal of As(V)

From the results obtained, the pH of As(V) had no effect on the removal of As(V) from water. The adsorption of As(V) by PDFe/Al nanocomposite was the same at all pH levels of the solution. Figure 5.5 shows the Eh-pH diagram of arsenic.

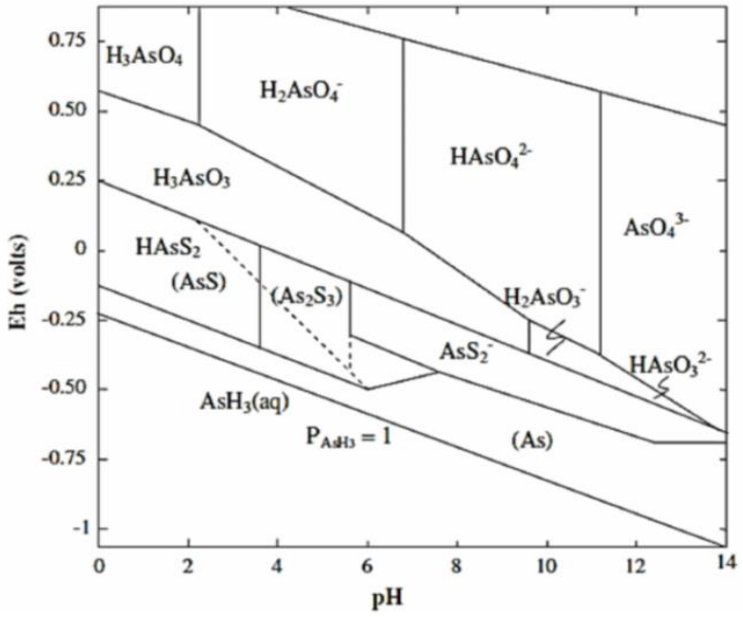

Figure 5.5: Eh – pH diagram of arsenic (Nicomel et al., 2016)

Oxyanions are more dominant between pH of 2 – 11 where the probability of removing them from water is high. This is when they are in solution as dihydrogen arsenate ($H_2AsO_4^-$) and

hydrogen arsenate ($HAsO_4^{2-}$). This zone accommodates the adsorption of As(V) onto PDFe/Al nanocomposite as adsorbent was also synthesised within that pH range. Moreover, ferric iron plays an important anionic exchange role in this pH range. Liu et al. (2012) also reported limited effect of pH on the removal of As(V) using iron and aluminum binary oxide. However, the point of zero charge of PDFe/Al nanocomposite was found to be pH = 3.02, but exhibited negligible effect on the adsorption of As(V).

Equations 5.1 and 5.2 illustrate the reaction between PDFe/Al nanocomposite and As (V) ions in an aqueous system (Nicomel et al., 2016):

Let Fe/Al be M

$$M(OH)_3 + 3H_2AsO_4^- + 3H^+ \rightarrow M(H_2AsO_4)_3 + 3H_2O \quad [5.1]$$

$$2M(OH)_3 + 3HAsO_4^{2-} + 6H^+ \rightarrow M_2(HAsO_4)_3 + 6H_2O \quad [5.2]$$

From equation 5.1, the exchange of OH^- ions from the adsorbent $[M(OH)_3]$ with H^+ ion to form adsorbent – adsorbate solid $[M_2(HAsO_4)_3]$ and liquid water is outlined. This behaviour is more likely to occur between pH 2 – 7.

From equation 5.2, the exchange of OH^- ions from the adsorbent $[M(OH)_3]$ with H^+ ions to form adsorbent – adsorbate solid $[M(HAsO_4)_3]$ and liquid water is outlined. This behaviour is more likely to occur between pH 7 – 11.

When the pH was measured after As(V) adsorption, it was observed that all the pH levels were between 2 – 3 after adsorption. The effect on the adsorption behaviour as a result of initial pH of As(V) by PDFe/Al may be attributed to the buffering effect of the As(V) oxyanion which releases a hydrogen ion in an alkaline aqueous solution and accepts a hydrogen ion in acidic aqueous solution. The fact that the point of zero charge of PDFe/Al nanocomposite was found to be pH = 3.02 and the lack of significant effect of the pH on the removal of As(V) can be explained by this abovementioned buffering effect of the As(V) solution.

5.1.4 Effect of agitation time

The effect of agitation time on the removal of As(V) from water is illustrated in Figure 5.6.

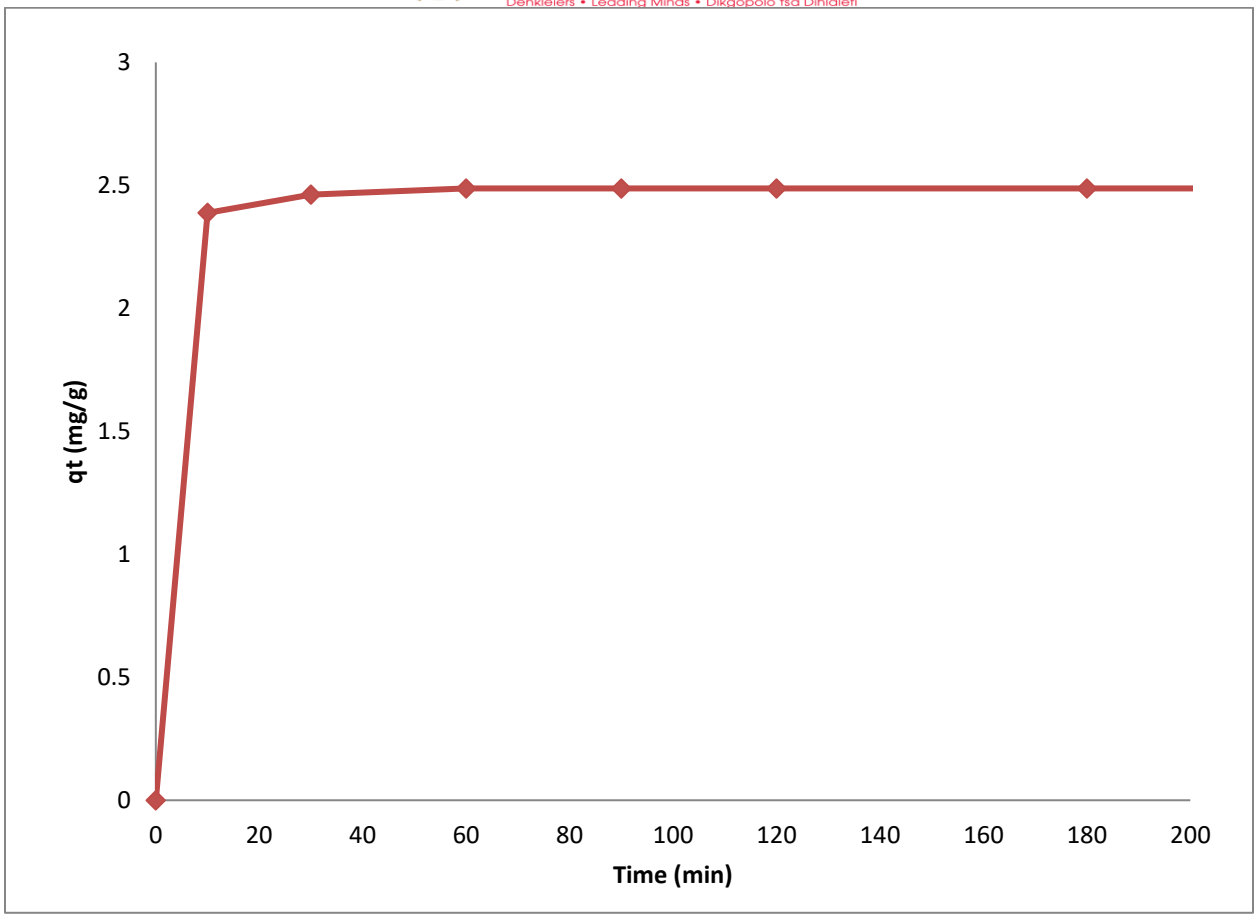

Figure 5.6: Effect of agitation time on the % removal of As(V) from water

Figure 5.6 demonstrates the adsorption capacity of As(V) onto PDFe/Al nanocomposite as a function of experimental time. The adsorption rapidly proceeds with anagitation time with more than 95% of the adsorption taking place within the initial 60 minutes. A study by Nekhunguni et al. (2017) reported that 90 minutes was optimum for removal of As(V) using an iron-based material, in comparison this study demonstrated that a significantly reduced time of 60 minutes is sufficient for equilibration.

5.1.5 Effect of temperature

Adsorption thermodynamics were studied by evaluating the effect of temperature on the adsorption of As(V) onto PDFe/Al nanocomposite. The percentage removal of As (V) from water is illustrated in Figure 5.7.

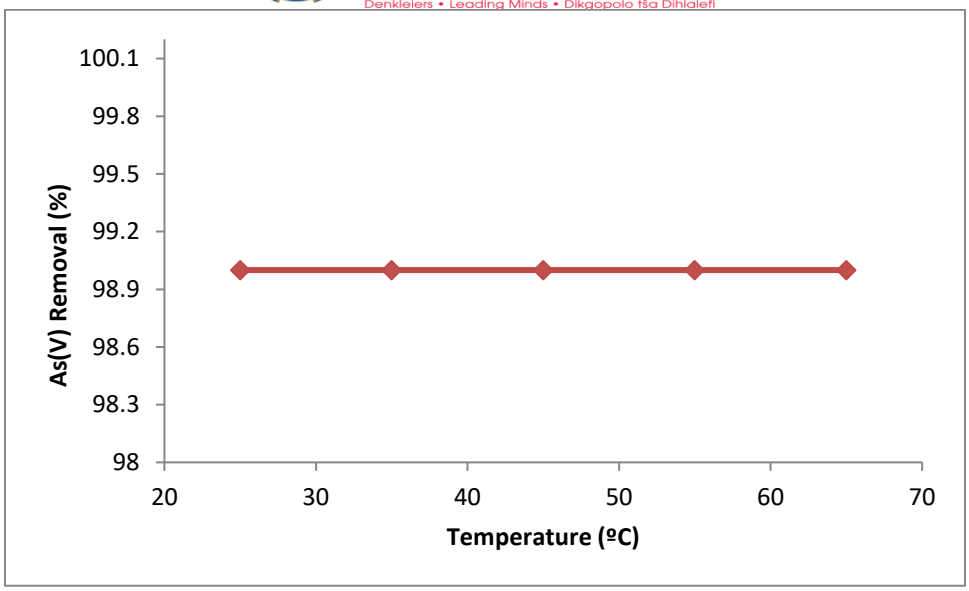

Figure 5.7: Effect of temperature on the removal of As(V) from water

From Figure 5.7 it can be observed that temperature has a negligible effect on the adsorption of As(V) onto PDFe/Al nanocomposite. However, it should be noted that an increase in temperature led to an increase in EC, TDS and Salinity. This behaviour is in agreement with a decrease in the pH i.e. the low pH is as a result of acidity contributed by PDFe/Al nanocomposite to the aqueous system, as it was synthesised from AMD at between pH 3 – 4. Nekhunguni et al. (2017) reported the optimum temperature of 53 ºC, while Vieira et al. (2017) also reported that 20 ºC is optimum for removal of As(V), which is still closer to standard or room temperature. In comparison, this adsorbent has the potential to efficiently adsorb As(V) at room temperature with consequent potential economic benefits.

5.2 Adsorption kinetics

Adsorption kinetics for the current study was determined to study the mechanism and rates of adsorption by the PDFe/Al nanocomposite. Figures 5.8, 5.9 and 5.10 show the results.

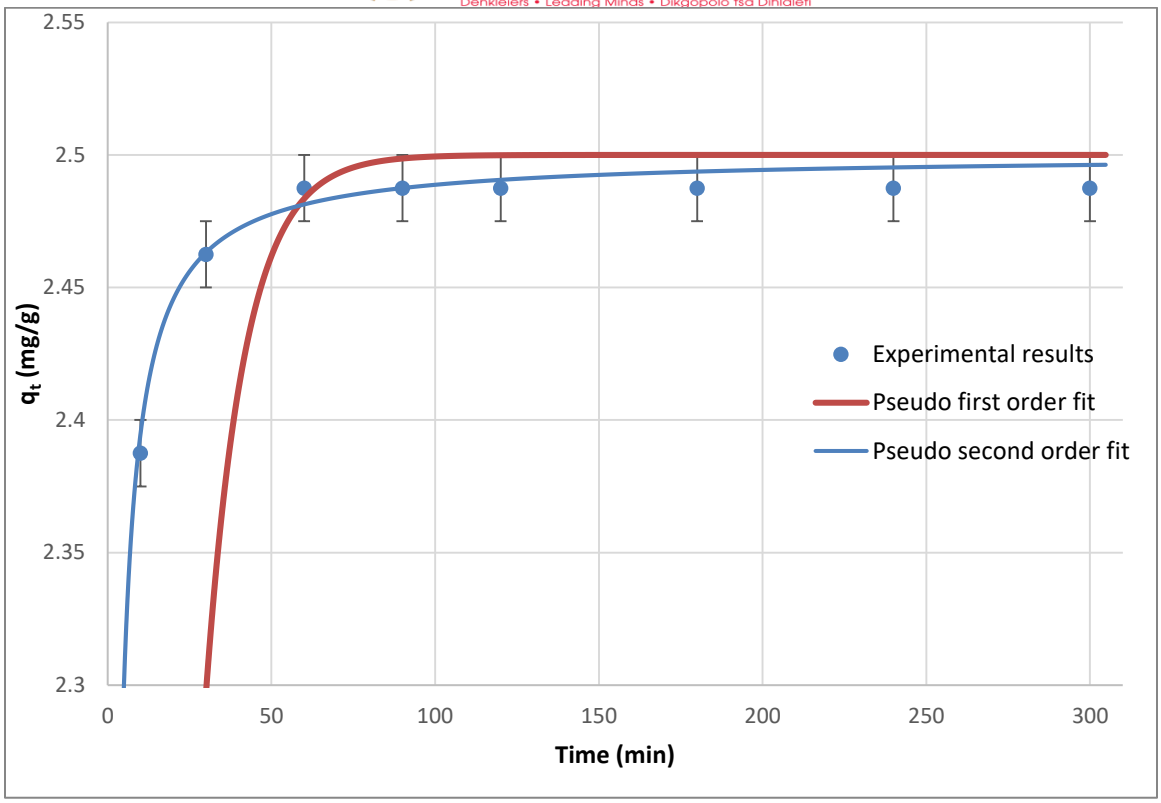

Figure 5.8: Pseudo-first order and pseudo second order graphs

Figure 5.8 was derived from figures 5.9 and 5.10

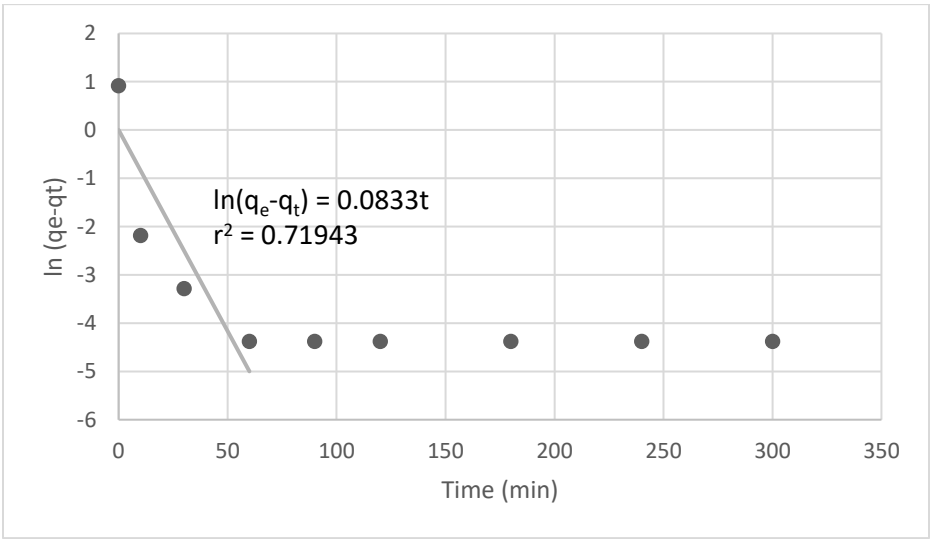

Figure 5.9: Pseudo-first-order graph: relationship between As(V) removal and time

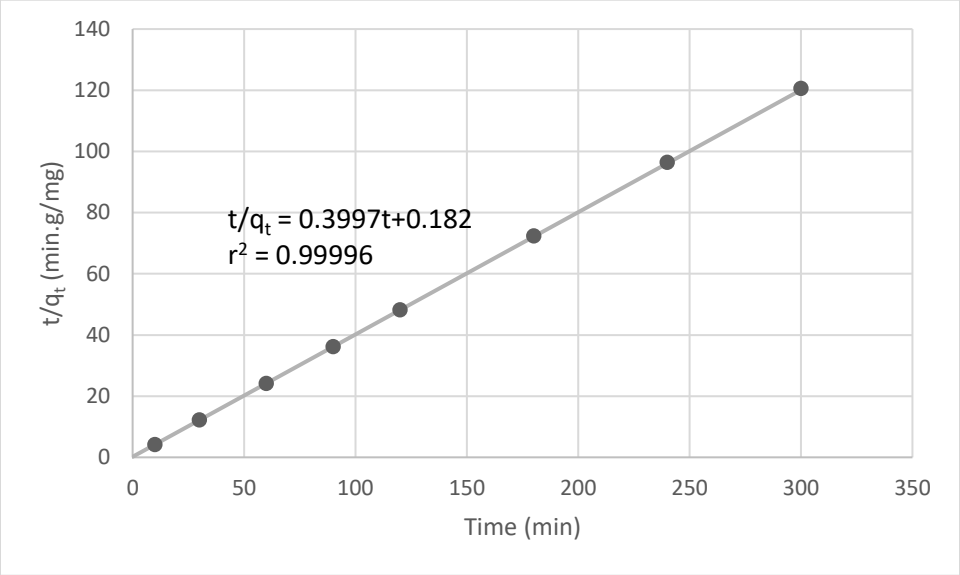

Figure 5.10: Pseudo-second order graph: relationship between As(V) removal and time

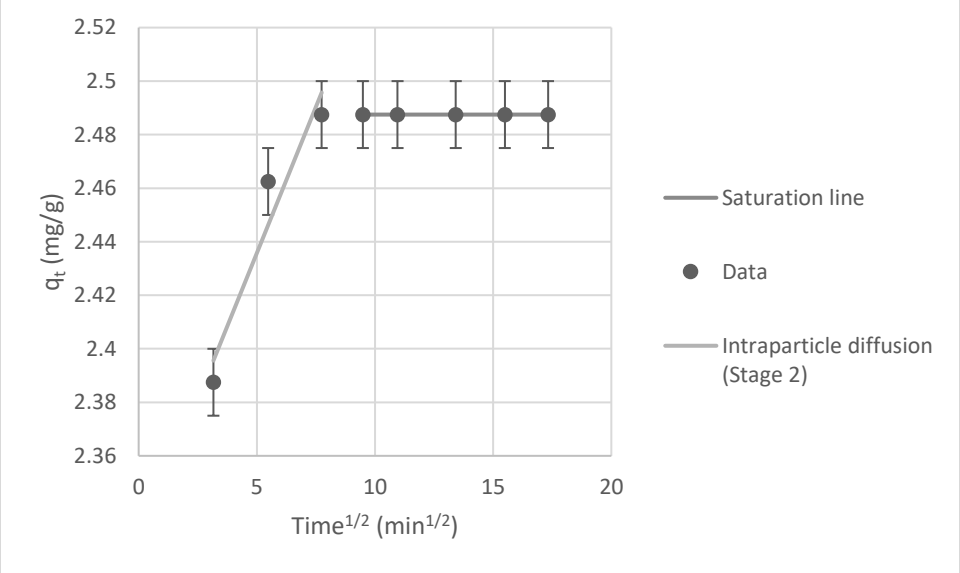

Figure 5.11 : Intra-particle diffusion graph: relationship between As(V) removal and time

Figure 5.9 shows the relationship between adsorption capacity and time as pseudo-first order. However, the data produces a correlation coefficient of $R^2 = 0.79$. This value is too low, and therefore the study did not follow pseudo-first order.

Figure 5.10 shows the relationship between adsorption capacity and time as pseudo-second order. The results show that the data corresponds to pseudo-second order since the correlation coefficient $R^2 > 0.99$. This best fits the data; hence the reaction followed a second-order reaction.

Other studies that reported pseudo-second order asserted that a chemisorption mechanism was present in the process (Ren et al., 2014, Zhang et al., 2010).

Figure 5.11 shows the relationship between adsorption capacity and time as intra-particle diffusion. The steep slope indicates the resistance in the internal mass transfer. Step 1 of the graph illustrates the diffusion of arsenate ions (AsO_4^{3-}) into the particle volume. Step 2 is rate-limiting where it is the gradual adsorption stage, hence the slowest step. This step determines the overall rate of other reactions in the system (Din et al., 2017).

5.3 Adsorption isotherms

The relationship between the removal of As(V) from water and the initial As(V) concentration was evaluated at different temperatures. The removal of As(V) is observed to be reversible and follows Langmuir isotherm.

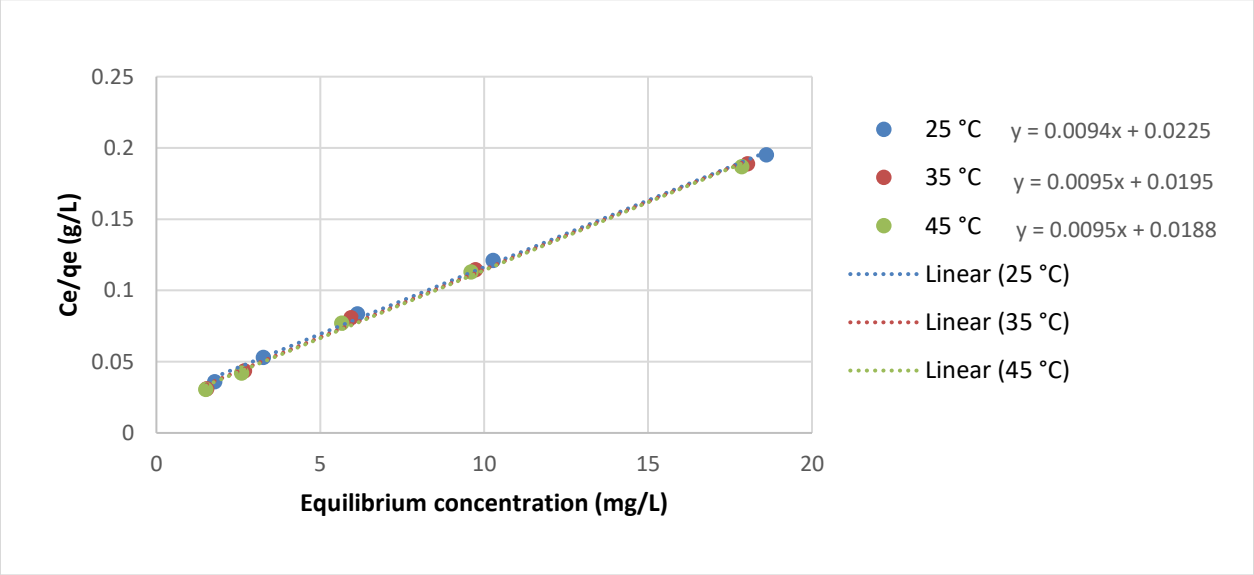

Figure 5.12: Relationship between Ce and Ce/qe

Table 10: Summary of parameters

Temperature (K)	b	Qo (mg/g)
298.15 (25 ºC)	0.416917	106.5973
308.15 (35 ºC)	0.488486	105.0539
318.15 (45 ºC)	0.505895	104.9082

5.4 Thermodynamics

Thermodynamics is an important component of any study. This is because studies should be cost effective; hence the need to determine how much energy is absorbed or released during experimental work. The results obtained in figure 5.7 showed that the system can be operated at room temperature. This implies that the system is non-spontaneous and endergonic (Koles-nikov, 2001).

However, when temperature is varied against variation of concentration, the results illustrated in Figures 5.13 are obtained. Figure 5.13 shows the relationship between adsorption capacity and equilibrium temperature at different temperatures.

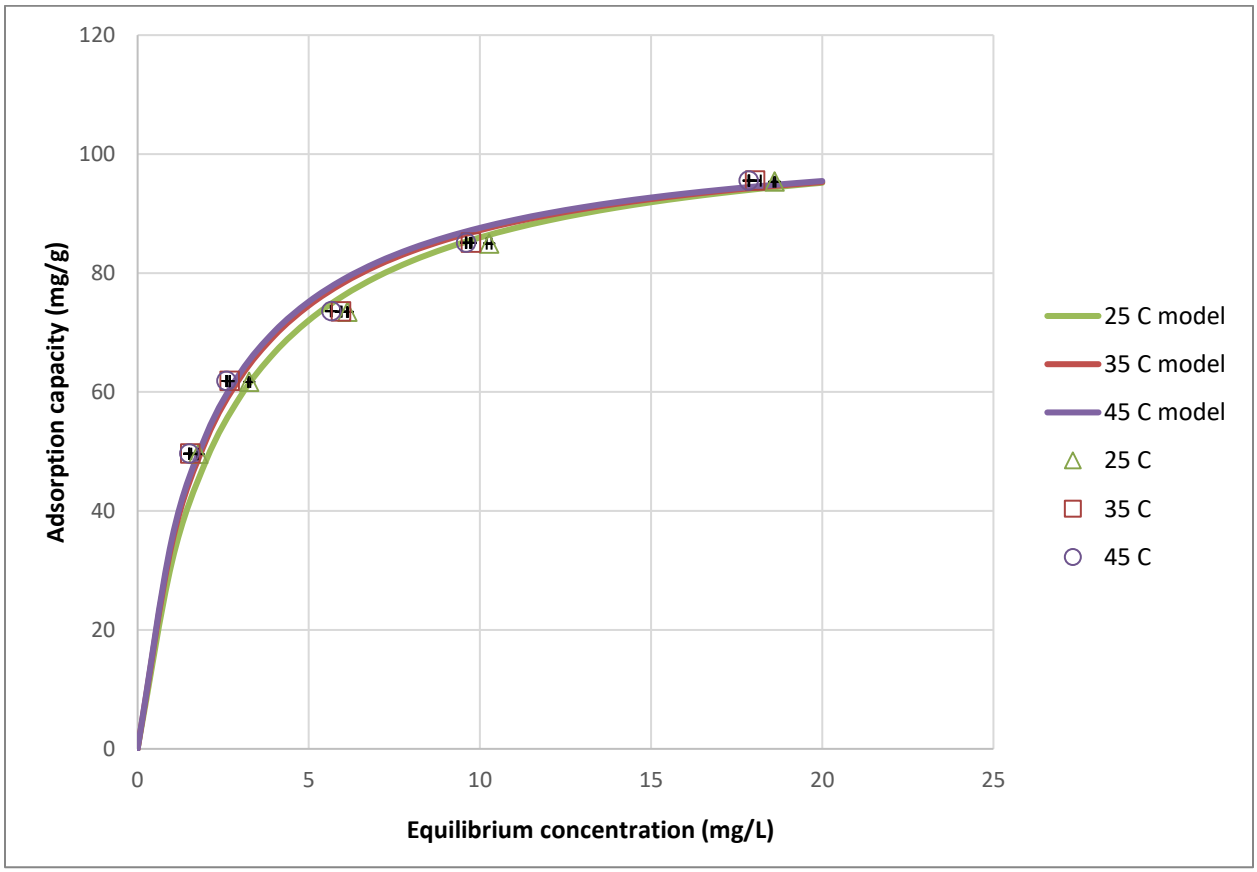

Figure 5.13: Relationship between equilibrium concentration and adsorption capacity at different temperatures

As illustrated in Figure 5.13, concentration was varied under different temperatures, namely 25, 35 and 45 degree Celsius. The trends for 35 and 45 degrees Celsius are more the same, as

compared to 25 degree Celsius which is slightly lower or different from the two. This could be due to the increase in energy of the system, hence increasing the adsorption capacity of the adsorbent material at 35 and 45º C.

The value of ΔG° is positive (1802 to 2168 J/mol), while the values of ΔH° = - 63 kJ/mol and ΔS° = 152 J/mol.K.

5.5 Characterisation of solid samples

5.5.1 Functional groups

Fourier Transform Infrared Spectrometer (FTIR) was used to determine the functional groups of PDFe/Al nanocomposite after adsorption and this was shown in Figure 5.14.

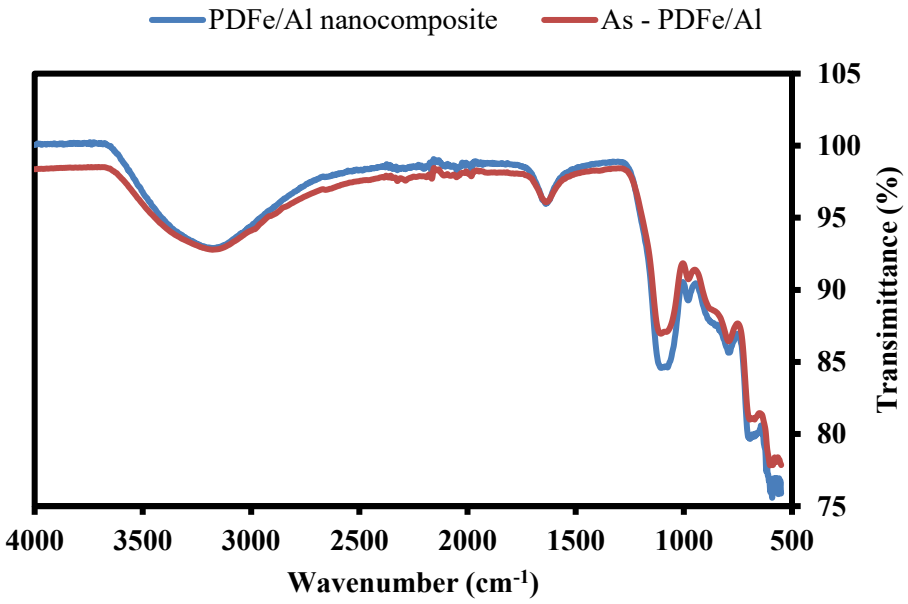

Figure 5.14: Functional groups of nanocomposite and As(V)-reacted nanocomposite.

From figure 5.14, the bands of As(V)-unreacted and reacted PDFe/Al nanocomposite are shown. The bands between 4000 –3500 cm^{-1} can be an illustration of the high stretching of O-H for the two bands. The adsorption band at 1668 cm^{-1} could be an indication of the stretching of HOH which further increased at 1113 cm^{-1} due to an increase in the HOH from arsenate in the product. The small band at 839cm^{-1} which curves upwards could be an indication of the stretching of As-

O (Bordoloi et al., 2013). Table 11 provides a summary of the functional groups and their respective wavenumbers.

The exact mechanism of adsorption is uncertain, however the FTIR results as presented in Figure 5.14 indicates a change in the surface morphology of the adsorbent.

Table 11: Functional groups and their respective wavenumbers in PDFe/Al nanocomposite after As-adsorption

Functional group	**Wavenumbers (cm^{-1})**	**Reference**
O-H	4000 –3500	(Bordoloi, Nath, Gogoi, & Dutta, 2013)
HOH	1668	(Bordoloi, Nath, Gogoi, & Dutta, 2013)
	1113	(Bordoloi, Nath, Gogoi, & Dutta, 2013)
As-O	839	(Bordoloi, Nath, Gogoi, & Dutta, 2013)

5.5.2 Mineralogical composition

X-ray diffraction (XRD) patterns and diffractogram for the As-PDFe/Al nanocomposite is shown in Figure 5.15.

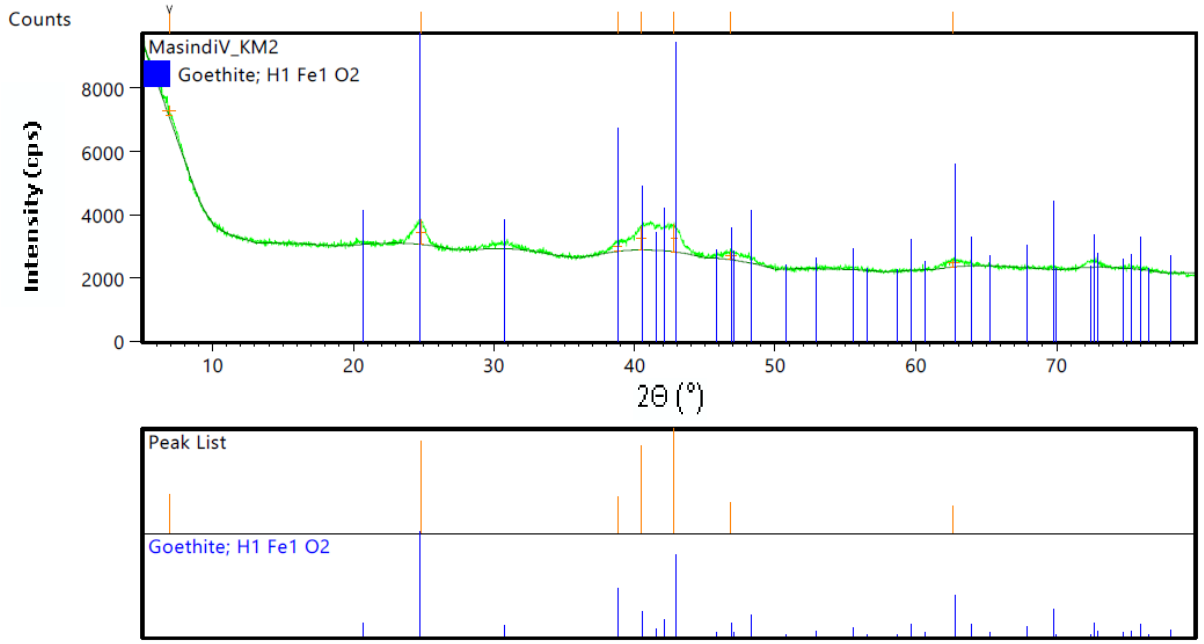

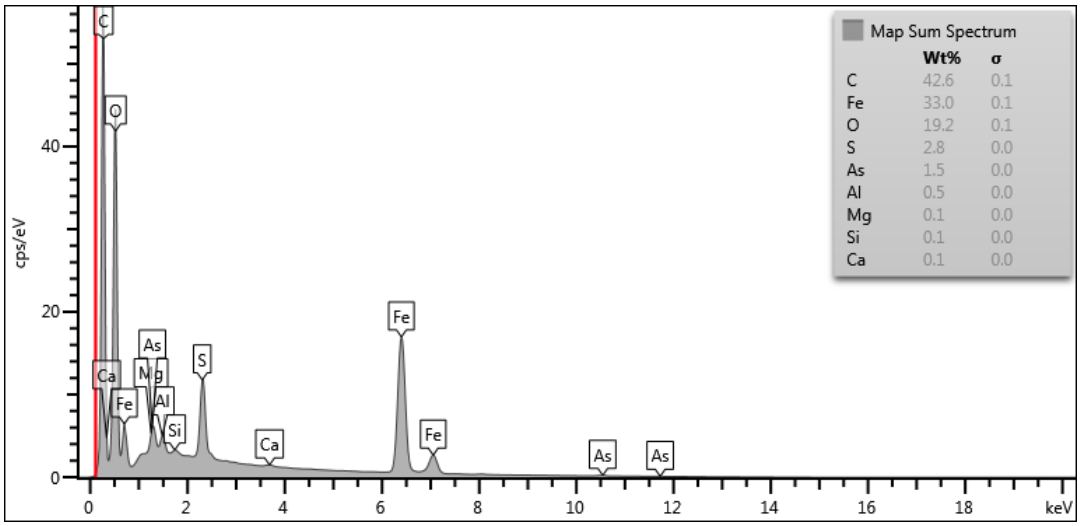

Figure 5.15: X-ray diffraction (XRD) patterns and diffractogram for the As-PDFe/Al nanocomposite.

From figure 5.15, it can be noted that the material shows a crystalline nature with some amorphousness in it. Moreover, the diffractogram only shows the presence of ferric iron (Fe^{3+}). This is because ferric iron is dominant compared to aluminium, hence the absence of Al^{3+} in the diffractogram as its concentration was below detection limit of the equipment. As compared to the raw material which depicted FeO(OH) as the dominant species, the As-reacted material also contains goethite. Moreover, arsenic was detected to be present in the material after As(V) adsorption. The diffractogram shows the presence of hydroxyl groups in the nanocomposite which could have highly influenced the high adsorption of As(V). The adsorption of As(V) showed no change in the structure of the adsorbent, and this shows the adsorption of arsenic on the surface of the nanocomposite without changing its crystalline structure (Yu et al., 2018). Table 10 of compound composition shows the presence of Al_2O_3 in the synthesised PDFE/Al nanocomposite.

5.5.3 Compound composition

X-ray fluorescence (XRF) was used to determine the compound composition of PDFe/Al nanocomposite after adsorption is shown in Table 12.

Table 12: Compound composition of PDFe/Al nanocomposite after adsorption

Compound	Certified	Analysed	Composite	As/composite
SiO_2	**99.6**	99.70	0.16	0.19
TiO_2	**0.01**	0.00	<0,01	<0,01
Al_2O_3	**0.05**	0.01	1.15	0.88
Fe_2O_3	**0.05**	0.01	58.80	65.30
MnO	**0.01**	0.00	0.05	0.03
MgO	**0.05**	0.01	0.23	<0,01
CaO	**0.01**	0.01	0.17	<0,01
Na_2O	**0.05**	0.02	0.38	<0,01
K_2O	**0.01**	0.01	<0,01	<0,01
P_2O_5	**0**	0.03	<0,01	0.05
Cr_2O_3	**0**	0.00	<0,01	0.01
NiO	**0**	0.01	<0,01	<0,01
ZrO_2	**0**	0.01	<0,01	<0,01
SO_3	**0**	0.00	0.38	<0,01
WO_3	**0**	0.00	0.03	0.16
CuO	**0**	0.00	<0,01	<0,01
Co_3O_4	**0**	0.00	0.03	0.13
SrO	**0**	0.00	<0,01	<0,01
LOI	**0**	0.10	38.60	33.30
Total	**100**	**99.94**	**99.98**	**100.04**

As shown in table 12, iron is the most dominant species in the synthesised PDFe/Al nanocomposite, followed by aluminium. The other components, such as Si and SO_3 are impurities which resulted from the co-precipitation and co-adsorption process from acid mine drainage (Masindi et al., 2018). The relative attenuation of the Al signal in the post adsorption spectra suggests that the surface concentration of Al decreased which was possibly a result of AsO_4^{3-} adsorption on the surface.

5.5.4 Morphology

Scanning Electron Micrographs (SEM-EDX) was used to determine the morphology of PDFe/Al nanocomposite after As-adsorption is shown in Figure 5.16.

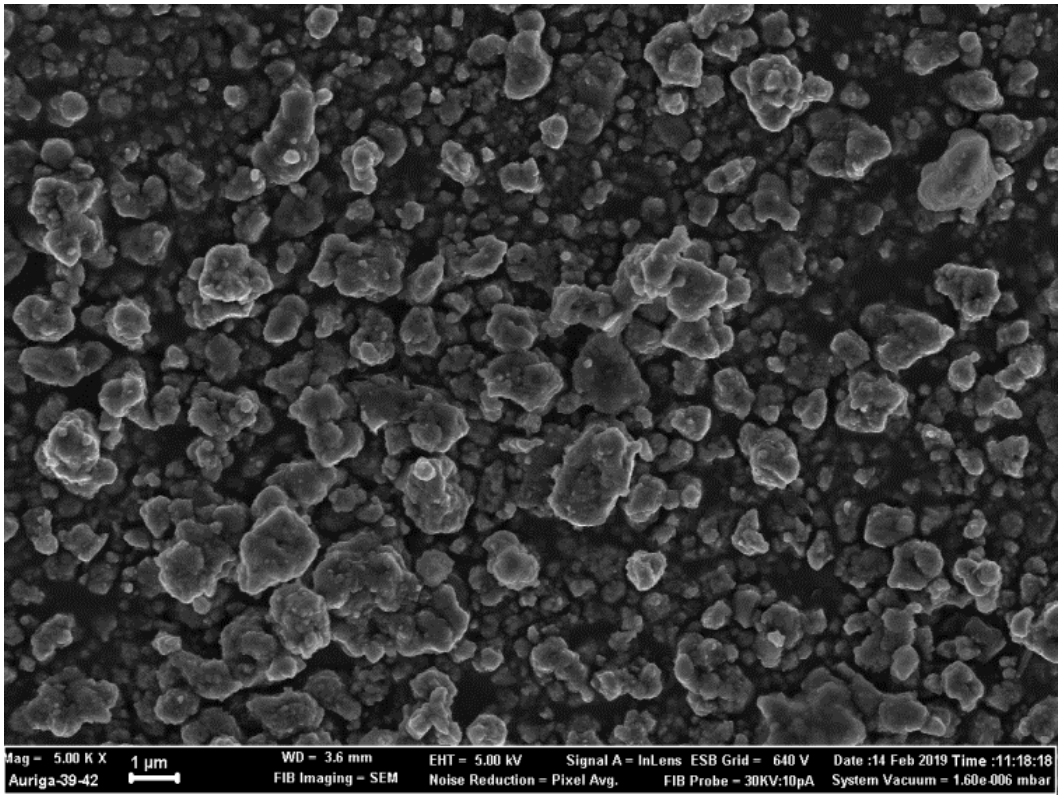

Figure 5.16: SEM images for As-reacted PDFe/Al nanocomposite

Figure 5.16 shows the visual structure of PDFe/Al nanocomposite after As(V) adsorption . After reacting with As(V), the material has pressed-like surface which could be an indication of arsenic presence. (Jiménez-Cedillo et al., 2009) and (Nekhunguni et al., 2017) reported that no clear change was observed after adsorption using their studies' pollutants.

5.5.5 EDX Mapping

The mapping of As-reacted PDFe/Al nanocomposite was done to determine the relative distribution of elements on the adsorbent surface as show in Figure 5.17.

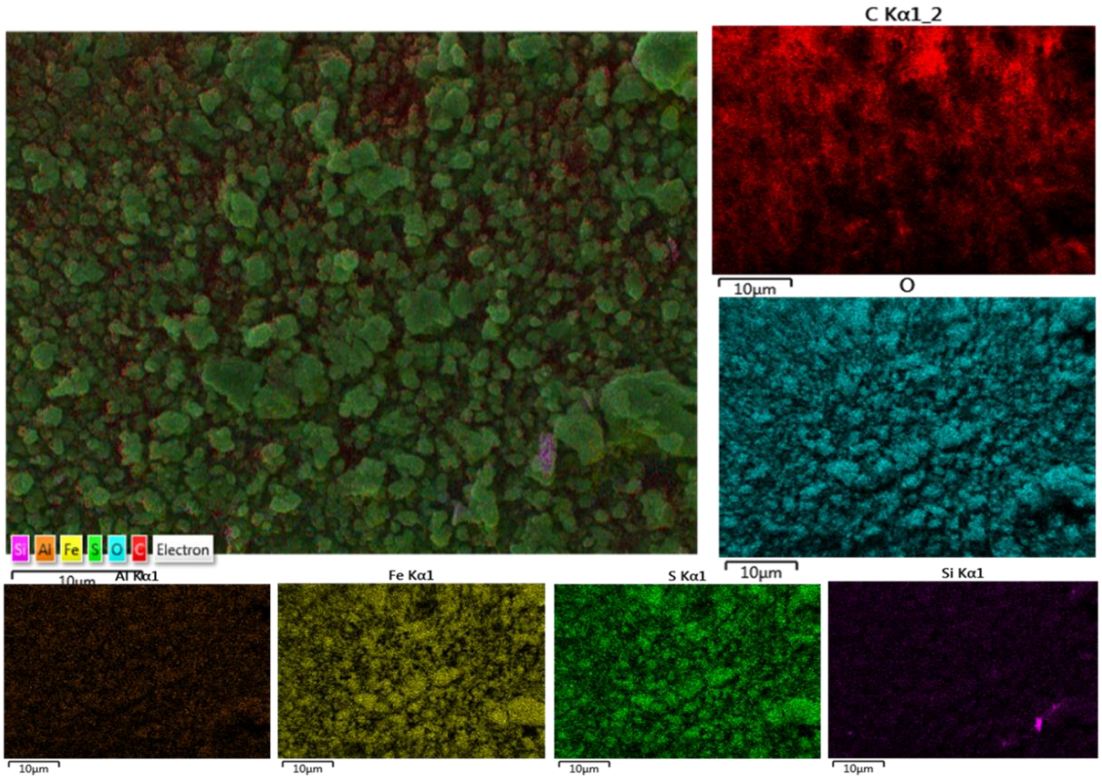

Figure 5.17: Mapping of As-reacted PDFe/Al nanocomposite

From figure 5.17, the presence of Fe, Al, O and S is observed. The mother structure has plate-like structures which indicate the adsorption of As onto the adsorbent. The presence of Si in the material is from AMD as impurities (Akinwekomi et al., 2017). Due to limitation of the equipment the EDX was not capable of confirming the presence of As(V), however Figure 5.15 detected and consequently confirmed the presence of As(V) on the spent adsorbent.

5.5.6 Thermal analysis

Thermogravimetric Analyser (TGA) was used to evaluate the thermal stability of PDFe/Al nanocomposite after adsorption. Figure 5.18 shows the thermal stability of the adsorbent after adsorption.

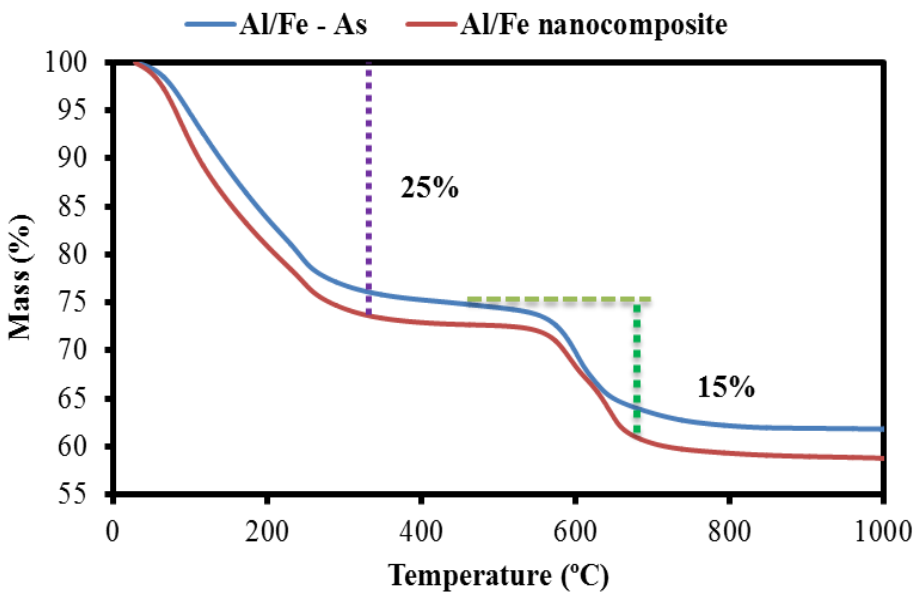

Figure 5.18: Thermal stability of PDFe/Al nanocomposite after adsorption

From figure 5.18, the thermal stability of PDFe/Al nanocomposite is observed. After 100 ºC, the compound starts losing a lot of moisture. This can mean that the OH group is removed from the material thus leaving it as $(Fe/Al)_2O_3$. (Wei et al., 2016) also reported a temperature of 150 ºC as being the maximum temperature before the state of Fe/Al interface could change as further heating changes the chemical structure of the material. Significant change was observed between thermal stabilities of PDFe/Al nanocomposite and As-reacted PDFe/Al nanocomposite. It is observed that As(V) adsorption stabilises the adsorbent material, but the cause is not certain.

5.5.7 Surface area and porosity

Brunauer-Emmet-Teller (BET) was used to characterise for surface area, pore size and pore volume of PDFe/Al nanocomposite after adsorption. A summary of the characteristics is provided in Table 13.

Table 13: BET characterisation of PDFe/Al nanocomposite after adsorption of As(V)

Sample	BET surface area (m^2/g)	Pore volume (cm^3/g)	Pore size (nm)
PDFe/Al nanocomposite	24.6275	0.042334	8.58545
$(PDFe/Al)_2(HAsO_4)_3$	48.8347	0.043656	8.70508

Table 13 shows that there is a significant and clear increase in the surface area of PDFe/Al nanocomposite of after adsorption if As(V). This is because when As(V) attaches to the amorphous surface of PDFe/Al nanocomposite, it creates a rough surface texture as arsenic is metallic and crystalline, hence producing a product (adsorbent – adsorbate) with a higher surface area. The synthesised PDFe/Al nanocomposite has pore size of 8.58545 nm which can be proof that the material is a mesoporous nanocomposite material as its pore size falls within the range of 2 – 50 nm (IUPAC, 1997). Some studies (Jeong et al., 2007, Han et al., 2016) have reported on low surface areas for Fe_2O_3 and Al_2O_3 to be 5.05 and 0.50 m^2/g, and 0.55 and 2.35 m^2/g, respectively. The materials were also reported to be mesoporous (Jeong et al., 2007). However, some studies (He et al., 2017, Chitrakar et al., 2011) reported high surface areas of Fe-Al materials of 47 – 134 m^2/g.

5.6 Regeneration and reusability study

Although researchers, scientists and environmentalists are in a continuous search to find an affordable and effective technology for water purification, it is important to avoid creating another environmental problem after using toxic chemical species. To prevent further pollution of the environment, regeneration/desorption study was done in order to evaluate the probability of recovering the used PDFe/Al nanocomposite. A procedure stated in 2.2.7 was followed. Figure 5.19 shows the % recovery of the adsorbent (PDFe/Al nanocomposite).

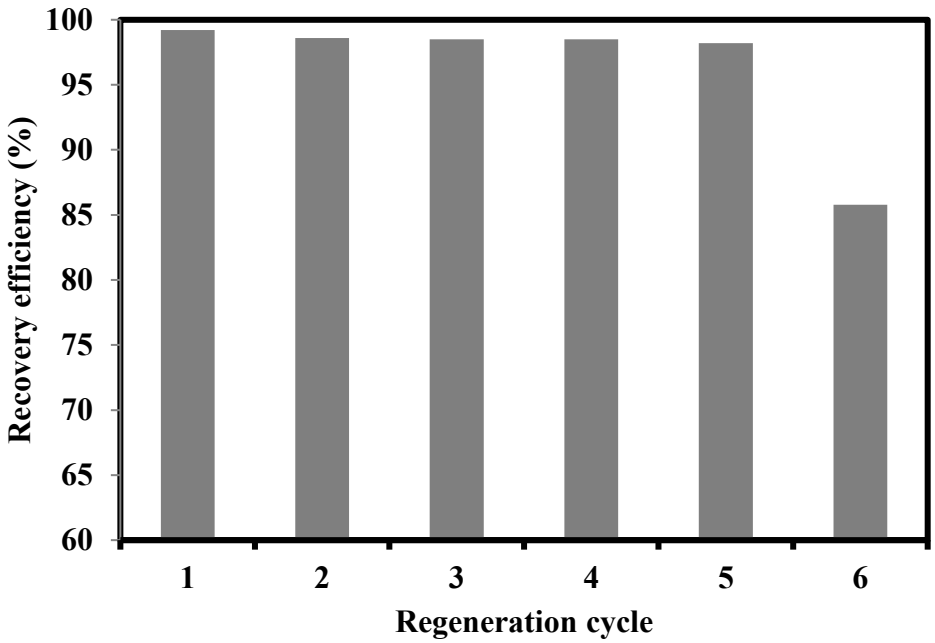

Figure 5.19: Recovery efficiency of PDFe/Al nanocomposite

As illustrated in figure 5.19, the first 5 cycles show outstanding recovery of the adsorbent (PDFe/Al nanocomposite). After the 5th cycle, a significant decline in the recovery is noted. This could be due to the strong ionic bond between oxygen (from arsenate) and metal (iron/aluminium) which still binds them together, thus making it difficult to separate the atoms (Satinder, 2014).

5.7 Comparison with other studies

The efficiency of PDFe/Al nanocomposite is shown in table 14, wherein a comparison of maximum adsorption capacities (q_e) between PDFe/Al nanocomposite and other Fe and/or Al-based adsorbents is provided.

Table 14: Comparison of PDFe/Al nanocomposite with other adsorbents

Adsorbent	**q_e (mg /g)**	**References**
PDFe/Al nanocomposite	105	This study
Iron (hydr) oxide modified zeolite	1.69	(Nekhunguni et al., 2017)
Magnetite	7.69	(Shahid et al., 2018)

Iron-coated seaweeds	7.3	(Vieira et al., 2017)
FeOOH/γ-Al_2O_3 granules	4.264	(Wang et al., 2018)
Goethite	7.740	(Jacobson and Fan, 2018)
Modified montmorillorite	16.89	(Ren et al., 2014)
Aluminium (hydr) oxide coated red scoria and pumice	2.68	(Asere et al., 2017)
Nano aluminium doped manganese copper ferrite polymer	0.053	(Malana et al., 2011)
Fe_3O_4@SiO_2@TiO_2 nanoabsorbent	21.3	(Feng et al., 2017)
Manganese ferrite nanoparticles	27.65	(Martinez–Vargas et al., 2018)

From table 14, the efficiency of PDFe/Al nanocomposite can be observed when it is compared with other materials. This is very notable because the other adsorbents were synthetically synthesized whereas PDFe/Al nanocomposite was recovered from authentic AMD, hence the importance of this study. The comparison shows the importance of recovery and synthesis of adsorbents from natural AMD as the adsorption capacity is higher than most of the synthetic materials. This also demonstrates synergistic effect of Fe/Al enhanced by mode of milling.

References

AKINWEKOMI, V., MAREE, J. P., ZVINOWANDA, C. & MASINDI, V. 2017. Synthesis of magnetite from iron-rich mine water using sodium carbonate. *Journal of Environmental Chemical Engineering,* 5**,** 2699-2707.

ASERE, T. G., DE CLERCQ, J., VERBEKEN, K., TESSEMA, D. A., FUFA, F., STEVENS, C. V. & DU LAING, G. 2017. Uptake of arsenate by aluminum (hydr)oxide coated red scoria and pumice. *Applied Geochemistry,* 78**,** 83-95.

BORDOLOI, S., NATH, S. K., GOGOI, S. & DUTTA, R. K. 2013. Arsenic and iron removal from groundwater by oxidation–coagulation at optimized pH: Laboratory and field studies. *Journal of Hazardous Materials,* 260**,** 618-626.

CHITRAKAR, R., MAKITA, Y., SONODA, A. & HIROTSU, T. 2011. Fe–Al layered double hydroxides in bromate reduction: Synthesis and reactivity. *Journal of Colloid and Interface Science,* 354**,** 798-803.

DIN, S. U., MAHMOOD, T., NAEEM, A., HAMAYUN, M. & SHAH, N. S. 2017. Detailed kinetics study of arsenate adsorption by a sequentially precipitated binary oxide of iron and silicon. *Environmental Technology***,** 1-9.

FENG, C., ALDRICH, C., EKSTEEN, J. J. & ARRIGAN, D. W. M. 2017. Removal of arsenic from alkaline process waters of gold cyanidation by use of Fe3O4@SiO2@TiO2 nanosorbents. *Minerals Engineering,* 110**,** 40-46.

HAN, W., FU, F., CHENG, Z., TANG, B. & WU, S. 2016. Studies on the optimum conditions using acid-washed zero-valent iron/aluminum mixtures in permeable reactive barriers for the removal of different heavy metal ions from wastewater. *Journal of Hazardous Materials,* 302**,** 437-446.

HE, X., QIU, X. & CHEN, J. 2017. Preparation of Fe(II)–Al layered double hydroxides: Application to the adsorption/reduction of chromium. *Colloids and Surfaces A: Physicochemical and Engineering Aspects,* 516**,** 362-374.

IUPAC. 1997. *Compendium of Chemical Terminology, 2nd ed.* [Online]. Oxford: Blackwell Scientific Publications. Available: http://goldbook.iupac.org [Accessed 2018-03-19].

JACOBSON, A. T. & FAN, M. 2018. Evaluation of natural goethite on the removal of arsenate and selenite from water. *Journal of Environmental Sciences*.

JEONG, Y., FAN, M., SINGH, S., CHUANG, C.-L., SAHA, B. & HANS VAN LEEUWEN, J. 2007. Evaluation of iron oxide and aluminum oxide as potential arsenic(V) adsorbents. *Chemical Engineering and Processing: Process Intensification,* 46**,** 1030-1039.

JIMÉNEZ-CEDILLO, M. J., OLGUÍN, M. T. & FALL, C. 2009. Adsorption kinetic of arsenates as water pollutant on iron, manganese and iron–manganese-modified clinoptilolite-rich tuffs. *Journal of Hazardous Materials,* 163**,** 939-945.

LIU, R., GONG, W., LAN, H., YANG, T., LIU, H. & QU, J. 2012. Simultaneous removal of arsenate and fluoride by iron and aluminum binary oxide: Competitive adsorption effects. *Separation and Purification Technology,* 92**,** 100-105.

MAJI, S. K., KAO, Y. H. & LIU, C. W. 2011. Arsenic removal from real arsenic-bearing groundwater by adsorption on iron-oxide-coated natural rock (IOCNR). *Desalination,* 280**,** 72-79.

MALANA, M. A., QURESHI, R. B. & ASHIQ, M. N. 2011. Adsorption studies of arsenic on nano aluminium doped manganese copper ferrite polymer (MA, VA, AA) composite: Kinetics and mechanism. *Chemical Engineering Journal,* 172**,** 721-727.

MARTINEZ–VARGAS, S., MARTÍNEZ, A. I., HERNÁNDEZ–BETETA, E. E., MIJANGOS–RICARDEZ, O. F., VÁZQUEZ–HIPÓLITO, V., PATIÑO-CARACHURE, C. & LÓPEZ–LUNA, J. 2018. As(III) and As(V) adsorption on manganese ferrite nanoparticles. *Journal of Molecular Structure,* 1154**,** 524-534.

MOSTAFA, M. G., CHEN, Y.-H., JEAN, J.-S., LIU, C.-C. & LEE, Y.-C. 2011. Kinetics and mechanism of arsenate removal by nanosized iron oxide-coated perlite. *Journal of Hazardous Materials,* 187**,** 89-95.

NEKHUNGUNI, P. M., TAVENGWA, N. T. & TUTU, H. 2017. Investigation of As(V) removal from acid mine drainage by iron (hydr) oxide modified zeolite. *Journal of Environmental Management,* 197**,** 550-558.

NICOMEL, N. R., LEUS, K., FOLENS, K., VAN DER VOORT, P., DU LAING, G., NAIDU, R. & MAHMUDUR RAHMAN, M. 2016. *Technologies for Arsenic Removal from Water: Current Status and Future Perspectives*.

REN, X., ZHANG, Z., LUO, H., HU, B., DANG, Z., YANG, C. & LI, L. 2014. Adsorption of arsenic on modified montmorillonite. *Applied Clay Science,* 97-98**,** 17-23.

SHAHID, M. K., PHEAROM, S. & CHOI, Y.-G. 2018. Synthesis of magnetite from raw mill scale and its application for arsenate adsorption from contaminated water. *Chemosphere,* 203**,** 90-95.

VIEIRA, B. R. C., PINTOR, A. M. A., BOAVENTURA, R. A. R., BOTELHO, C. M. S. & SANTOS, S. C. R. 2017. Arsenic removal from water using iron-coated seaweeds. *Journal of Environmental Management,* 192**,** 224-233.

WANG, Z., SHEN, X., JING, M. & LI, C. 2018. Enhanced arsenic removal from drinking water by FeOOH/γ-Al2O3 granules. *Journal of Alloys and Compounds,* 735**,** 1620-1628.

WEI, Y., SHAO, W., MA, Z., CHEN, Z. & LU, W. 2016. Preparation and thermal stability of an atomically sharp Fe/Al interface. *Materials Letters,* 185**,** 537-540.

YU, Y., YU, L., SHIH, K. & CHEN, J. P. 2018. Yttrium-doped iron oxide magnetic adsorbent for enhancement in arsenic removal and ease in separation after applications. *Journal of Colloid and Interface Science,* 521**,** 252-260.

ZHANG, S., NIU, H., CAI, Y., ZHAO, X. & SHI, Y. 2010. Arsenite and arsenate adsorption on coprecipitated bimetal oxide magnetic nanomaterials: MnFe2O4 and CoFe2O4. *Chemical Engineering Journal,* 158**,** 599-607.

CHAPTER SIX

Cr(VI) ADSORPTION STUDY: RESULTS AND DISCUSSION

6.0 Introduction

This chapter focuses on the evaluation of the efficiency of recovered and synthesised poly-cationic dimetallic Fe/Al nanocomposite on the removal of chromium (Cr(VI)) from industrial effluents: Evaluation of adsorption kinetics, reaction equilibrium and mechanisms.

6.1 Optimization of adsorption parameters

6.1.1 Effect of initial concentration

The effect of initial concentrations of Cr(VI) on the adsorption onto PDFe/Al nanocomposite is shown in Figure 6.1, where the relationship between residual Cr(VI) and the studied initial concentrations of Cr(VI) is illustrated.

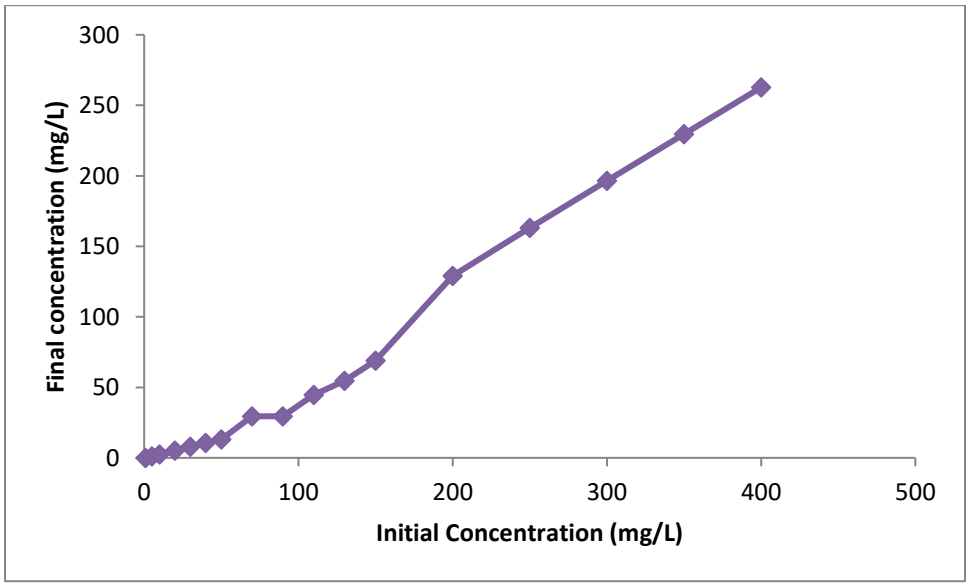

Figure 6.1: Effect of initial concentration on the removal of Cr(VI)

As shown in figure 6.1, an effective removal of Cr(VI) from solution by the PDFe/Al nanocomposite was observed for concentrations up to 50 mg/L. A consistent increase in the final concentration is observed between 1 – 50 mg L^{-1} of concentration. After 50 mg/L, a steep increase is observed, thus indicating super saturation of the adsorbent. This indicates that 50 mg/L and 70 mg/L. Therefore, it can be concluded that 50 mg/L is the optimum concentration of Cr(VI) solution for adsorption of hexavalent chromium ions by PDFe/Al nanocomposite. (Enniya et al., 2018) also reported an optimum initial Cr(VI) concentration of 50 mg/L.

6.1.2 Effect of adsorbent dosage

The effect of PDFe/Al nanocomposite dosage on the adsorption of Cr(VI) is shown in Figure 6.2, where the relationship between % removal and the dosage is illustrated.

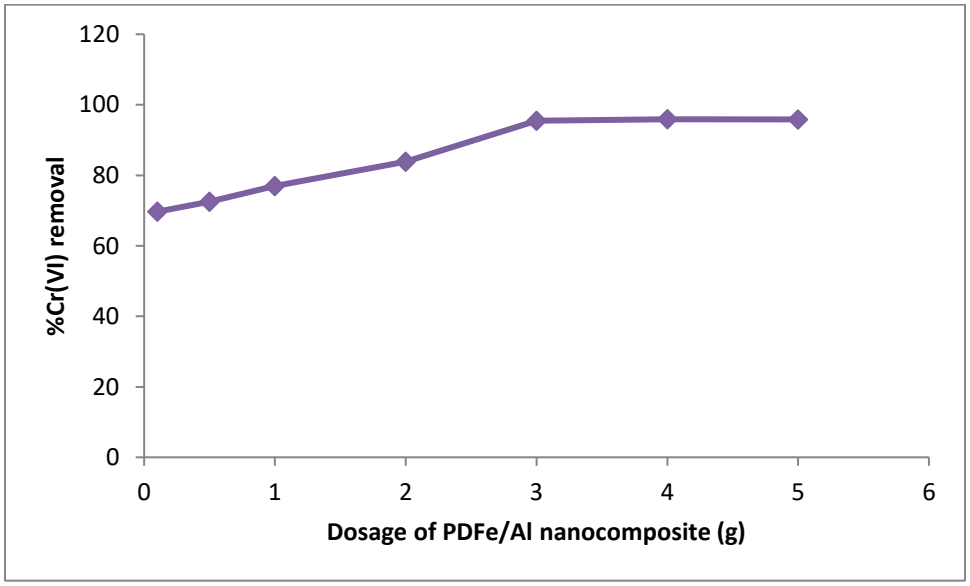

Figure 6.2: Effect of PDFe/Al nanocomposite dosage on the % removal of Cr(VI) from water

Figure 6.3 illustrates the relationship between dosage and adsorption capacity

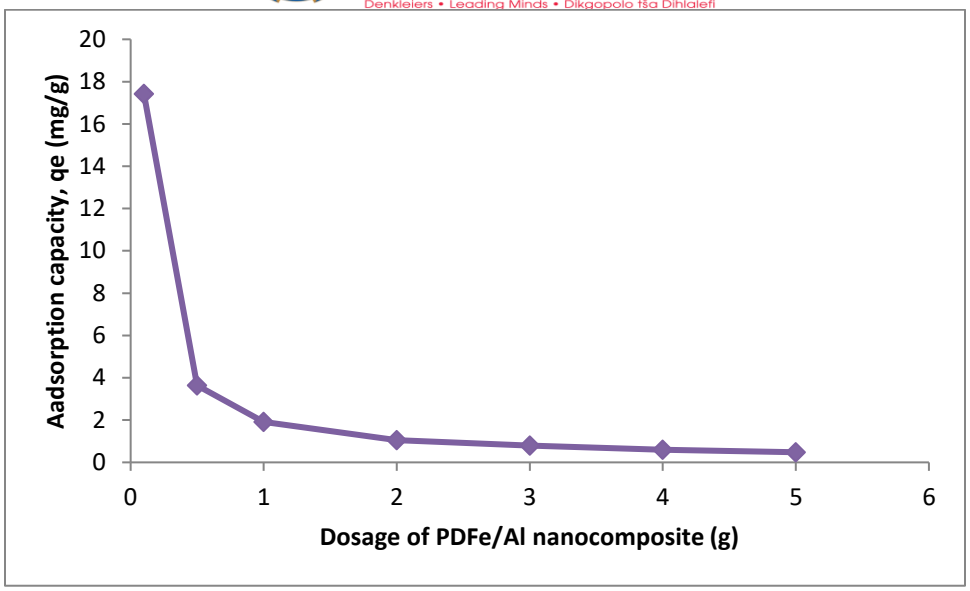

Figure 6.3: Relationship between the adsorption capacity (q_e) and the dosage of PDFe/Al nanocomposite

An even increase in percentage removal of Cr(VI) is observed from 0.1 – 3 g of PDFe/Al dosage. After 3g, the graph takes a gentle slope. This could indicate saturation of the adsorbent; hence it could not take any more of Cr(VI) ions. This behaviour is also seen in figure 6.3, where the maximum adsorption capacity of 1g PDFe/Al nanocomposite in 250 mL of 10 mg/L Cr(VI) solution was observed to be approximately 1 mg/g. The obtained results show that 3g of PDFe/Al nanocomposite is optimum dosage in this study. Optimum dosage of 3 g was also reported by (Gürü et al., 2008) whose study used diatomite for the removal of chromium from water.

6.1.3 Effect of initial pH

The effect of solution initial pH on the adsorption of Cr(VI) is shown in Figure 6.4, where the relationship between % removal and initial pH is illustrated.

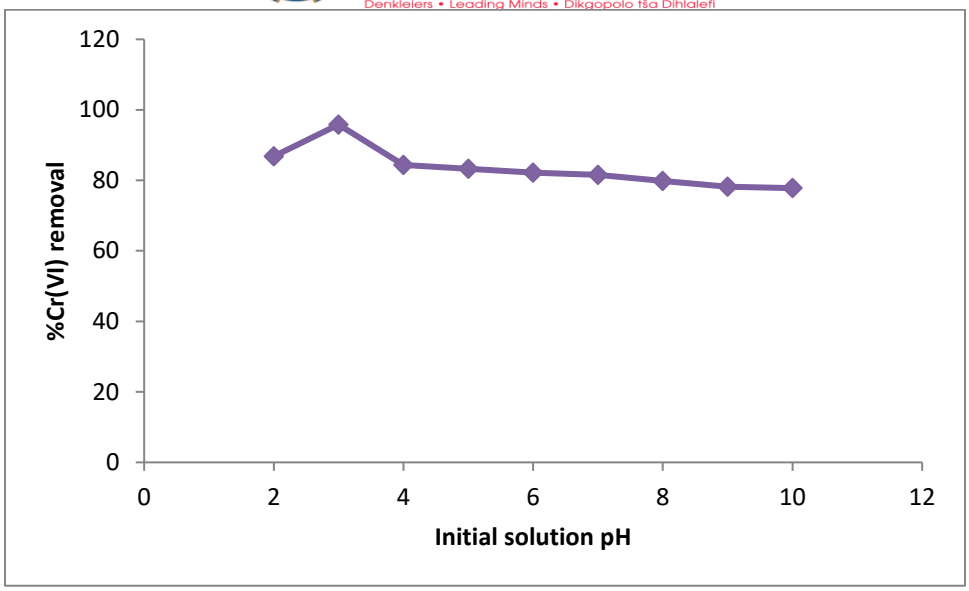

Figure 6.4: Effect of initial pH of Cr(VI) solution on the removal of Cr(VI)

Figure 6.4 shows that a lot of Cr(VI) ions were removed from water at a pH of 3. This corroborates the value of point of zero charge of the adsorbent which was found to be pH_{PZC} = 3.02, which is also within the pH range 3 – 4 at which the adsorbent (PDFe/Al) was synthesised. (Gallios and Vaclavikova, 2008) also reported that the adsorption of Cr(VI) on magnetite (Fe_3O_4) decreases with an increase of pH after level 3. An optimal pH of 3 was also obtained by (Yang et al., 2015).

6.1.4 Effect of agitation time

The effect of agitation time on the adsorption Cr(VI) is shown in figure 6.5, where the relationship between % removal and agitation time is illustrated.

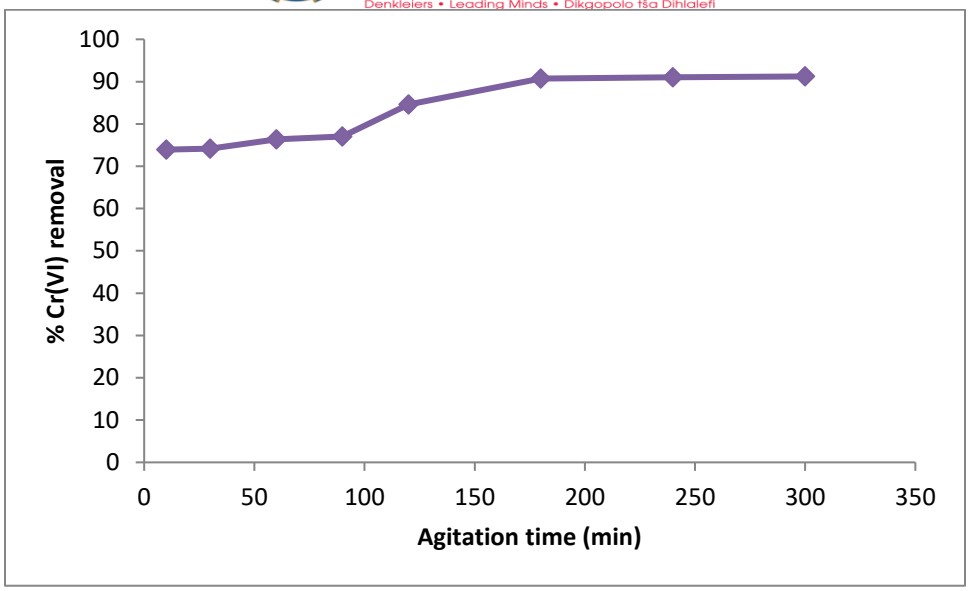

Figure 6.5: Effect of agitation time on the % removal of Cr(VI) from water

From figure 6.5, it can be seen that removal of Cr(VI) from water continues and increases with time. When the mixture is agitated for 180 minutes, no significant percentage removal takes place. After 3 hours (180 minutes) of agitation, the graph takes a gentle slope. This can indicate that the optimum equilibration time for the current study is 180 minutes. Most studies reported 4 hours as the optimal time for removal of Cr(VI) from water (Hu et al., 2010, Gaffer et al., 2017).

6.1.5 Effect of temperature

The effect of temperature on the adsorption of Cr(VI) is shown in figure 6.6, where the relationship between % removal and temperature is illustrated.

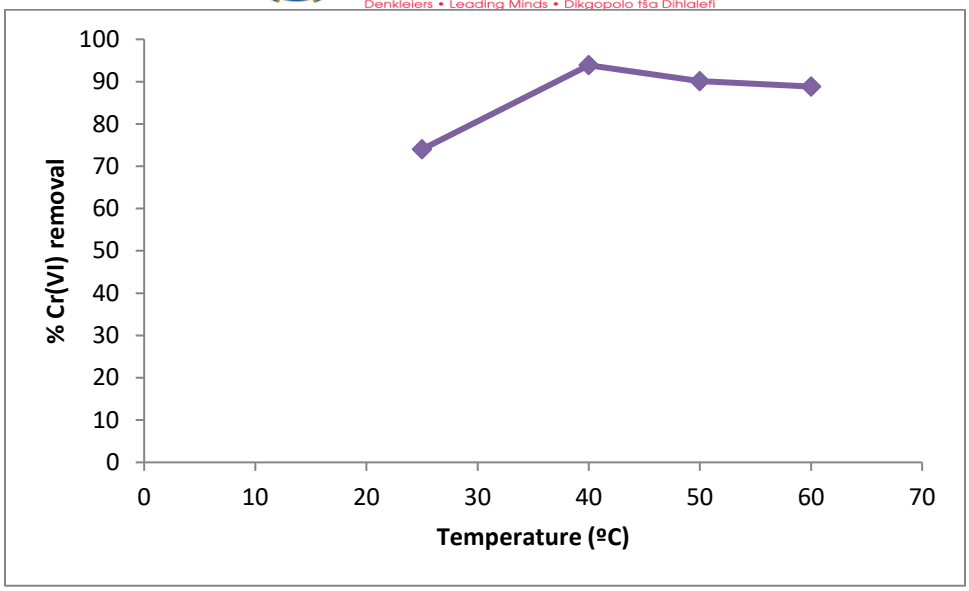

Figure 6.6: Effect of temperature on the removal of Cr(VI) from water

From figure 6.6, it can be noted that the percentage removal of hexavalent chromium from water using PDFe/Al increases as temperature increases, but within a range 25 – 40 ºC. Temperatures higher than 40 make Cr(VI) go back into solution, therefore making 40 ºC optimum for this study. An optimal temperature of 40 ºC for Cr(VI) removal was also obtained by (Enniya et al., 2018)

6.2 Adsorption kinetics

Adsorption kinetics for the current study was determined to study the mechanism and rates of adsorption by the PDFe/Al nanocomposite. Figures 6.7, 6.8 and 6.9 show the results.

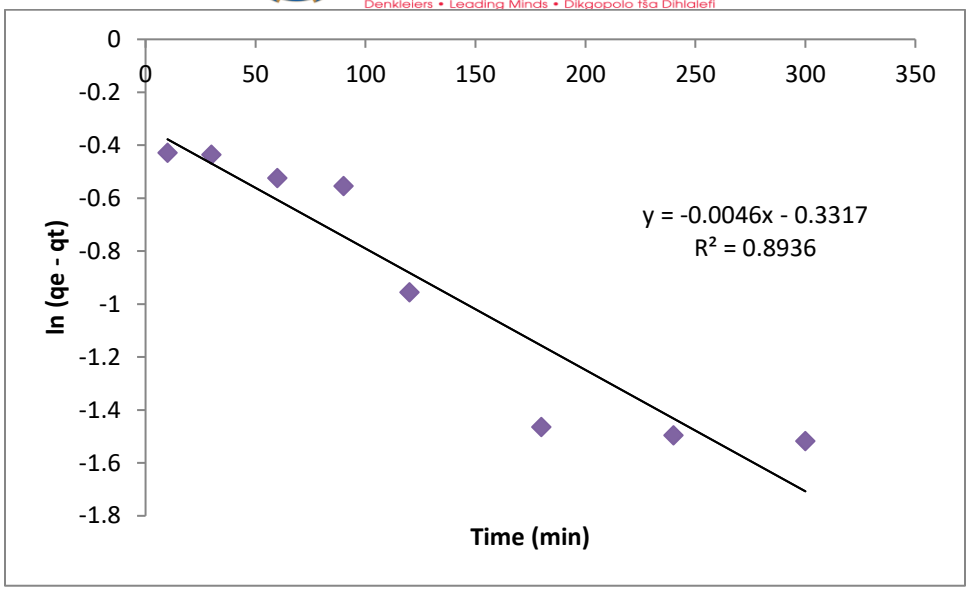

Figure 6.7: Pseudo-first-order graph: relationship between Cr(VI) removal and time

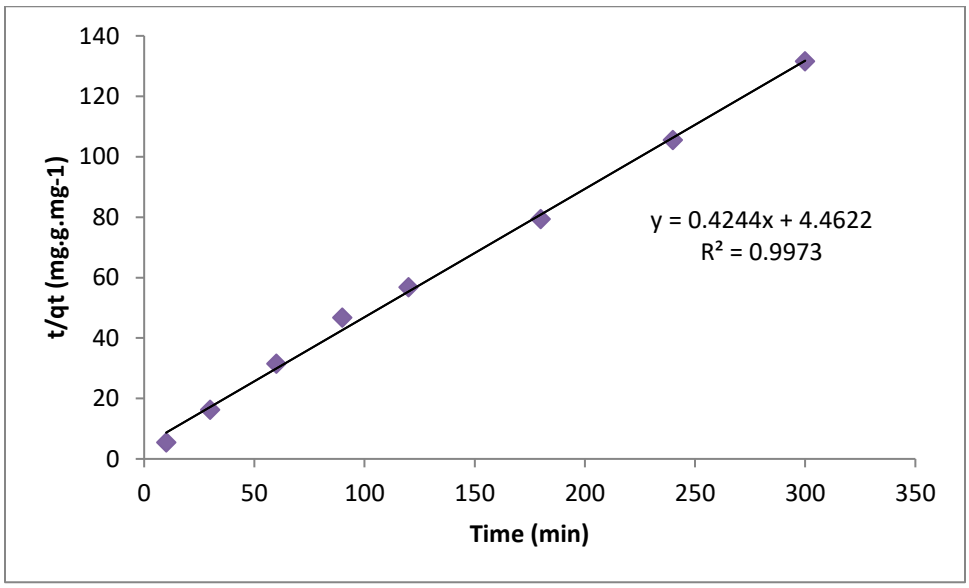

Figure 6.8: Pseudo-second order graph: relationship between Cr(VI) removal and time

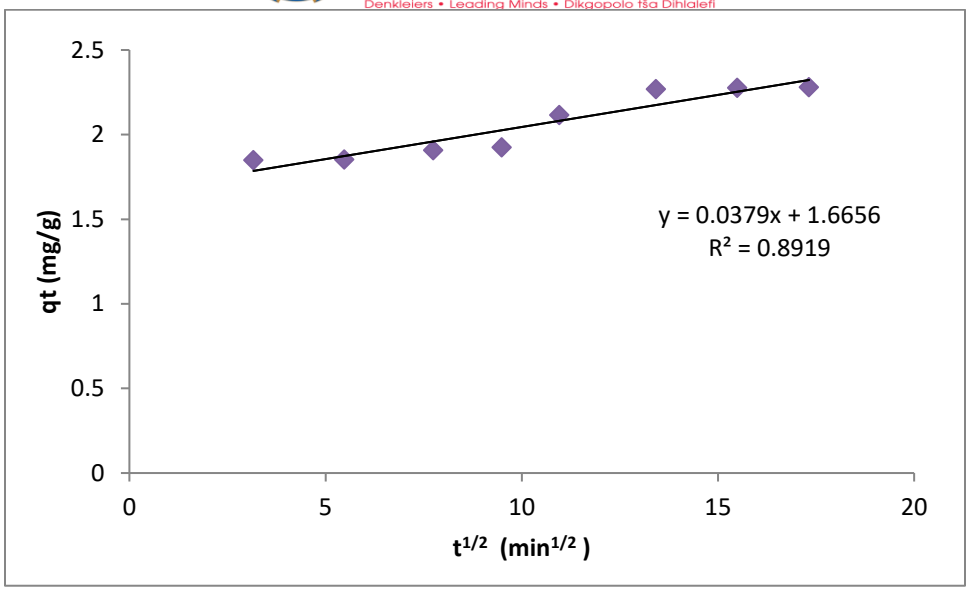

Figure 6.9: Intra-particle diffusion graph: relationship between Cr(VI) removal and time

From figures 6.7, 6.8 and 6.9, the relationship between adsorption capacity and time is observed illustrating pseudo-first order, pseudo-second order and intra-particle diffusion, respectively. Experimental data best fitted pseudo-second order kinetics compared to pseudo-first order and intra-particle diffusion as the correlation coefficient is $R^2 > 0.99$, which relates to the availability of adsorption sites on the adsorbent (Liu, 2008). A number of studies also reported the adsorption of Cr(VI) following a pseudo-second order process (Zhang et al., 2018b, Gürü et al., 2008).

6.3 Adsorption isotherms

Adsorption isotherms were evaluated for Cr(VI), as illustrated in Figures 6.10 and 6.11.

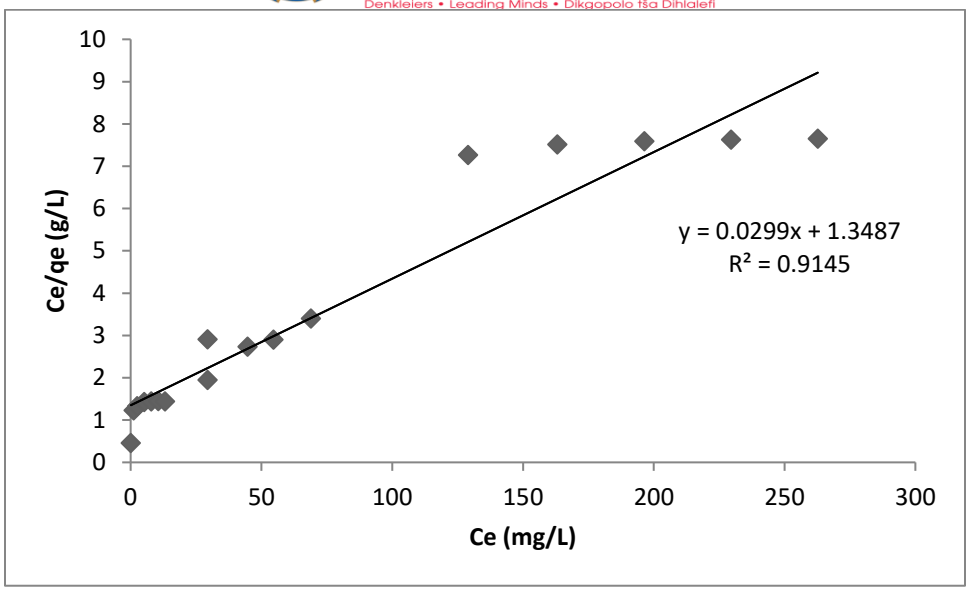

Figure 6.10: Langmuir adsorption isotherm: relationship between removal and initial concentration of Cr(VI)

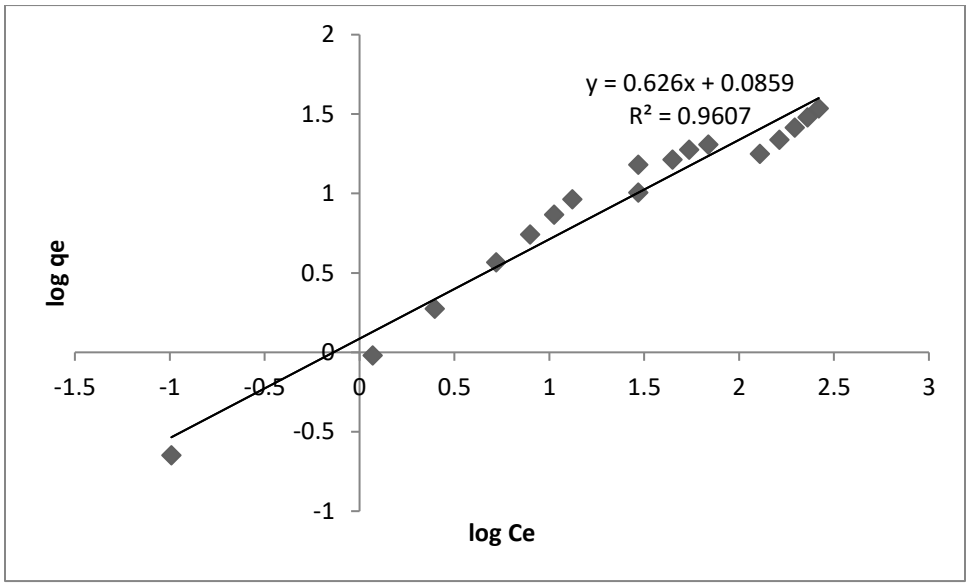

Figure 6.11: Freundlich adsorption isotherm: relationship between removal and initial concentration of Cr(VI)

From figures 6.10 and 6.11, the relationship between the adsorption capacity of the adsorbent and equilibrium concentration of Cr(VI) is depicted. From the plots, the data best fitted Freundlich adsorption, which is based on the multilayer adsorption of pollutant onto a heterogeneous surface. This is the same for this study because the material is heterogeneous (Zhang et al., 2010).

6.4 Thermodynamics

Thermodynamics is illustrated by figure 6.12 and 6.13.

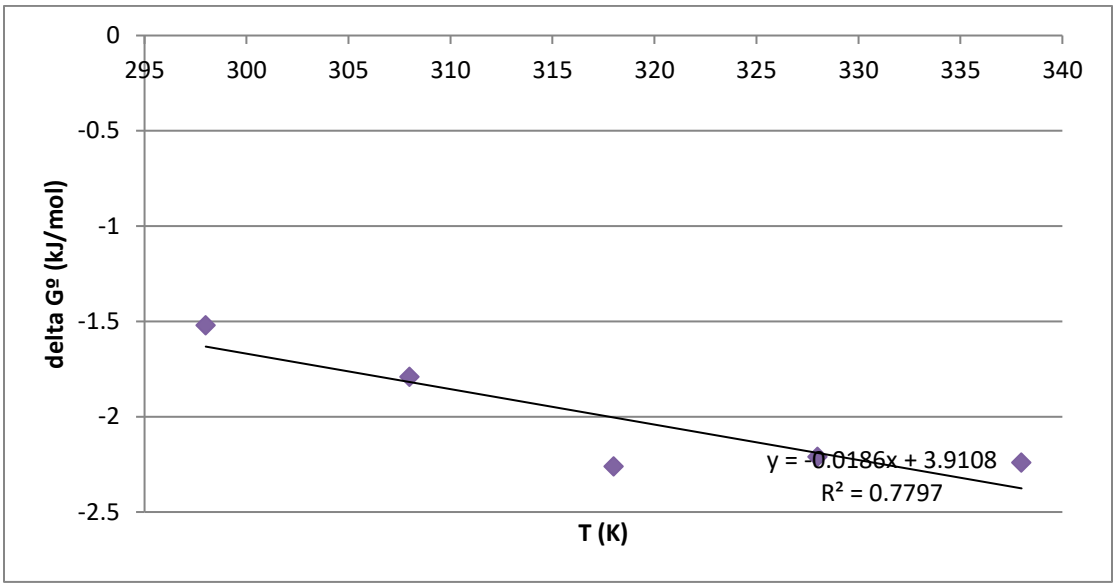

Figure 6.12: Relationship between temperature and Gibbs free energy

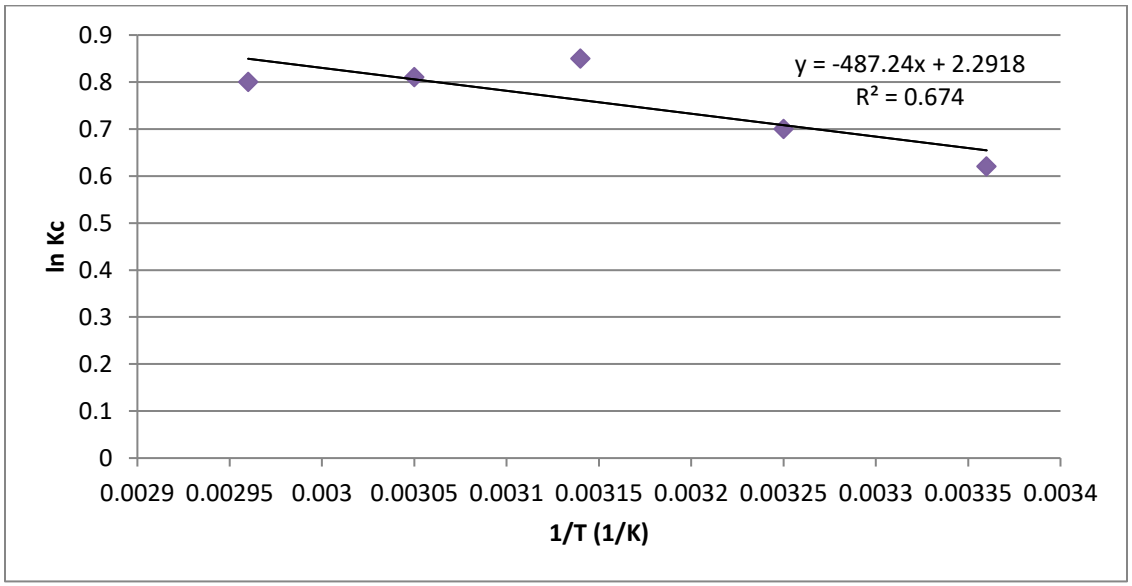

Figure 6.13: Relationship between 1/T and ln Kc

According to the rule of Gibbs free energy with relation to enthalpy change and entropy change, adsorption of Cr(VI) by PDFe/Al nanocomposite is spontaneous. This is because a negative ΔG°, negative $\Delta H^{\circ} = -4050.9$ J/mol and positive $\Delta S^{\circ} = 19.05$ J/mol were obtained.

6.5 Characterization of solid samples

6.5.1 Functional groups

Fourier Transform Infrared Spectrometer (FTIR) was used to determine the functional groups of PDFe/Al nanocomposite after adsorption and this was shown in Figure 6.14.

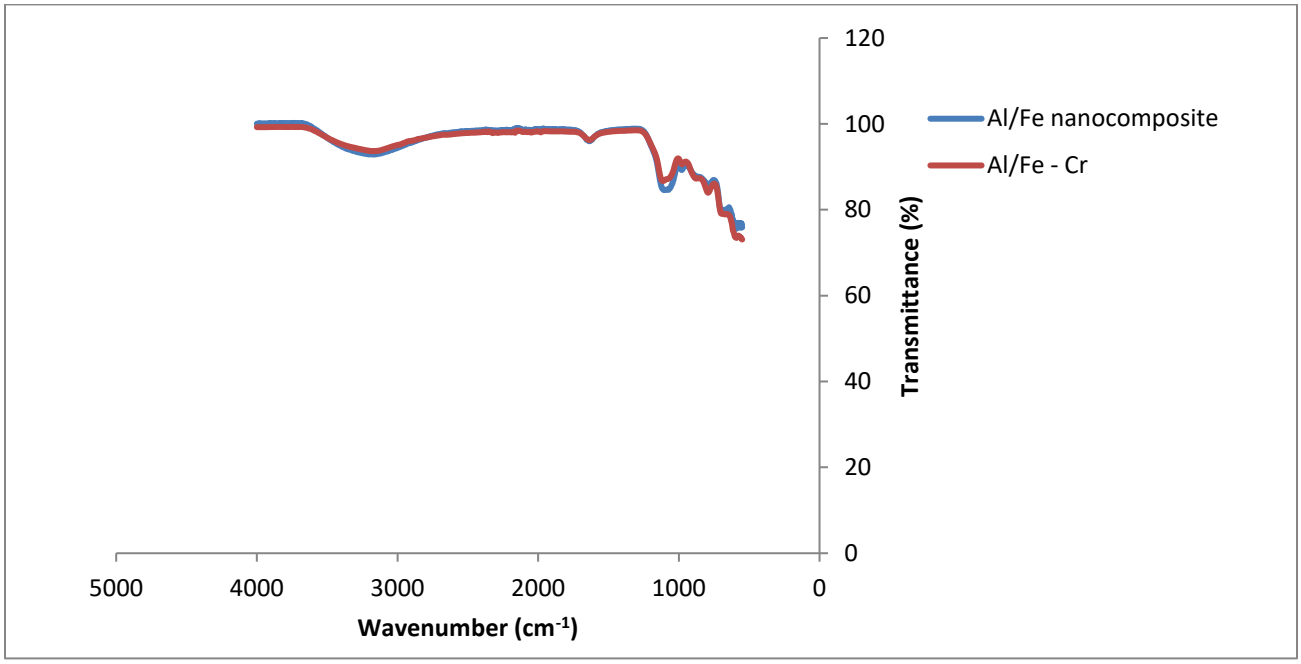

Figure 6.14: Functional groups of nanocomposite and Cr(VI)-reacted nanocomposite

From figure 6.14, bands of raw nanocomposite and Cr(VI)-reacted nanocomposite. A shift of wave band 1138 to 1151 cm^{-1} is observed which could be an indication that – OH group at the surface of the material is responsible for the change (Tarun Kumar Naiya et al., 2011). However, no major shift is observed in the bands before and after Cr(VI) adsorption.

6.5.2 Mineralogical composition

X-ray diffraction (XRD) patterns and diffractogram for the Cr-PDFe/Al nanocomposite is shown in Figure 6.15.

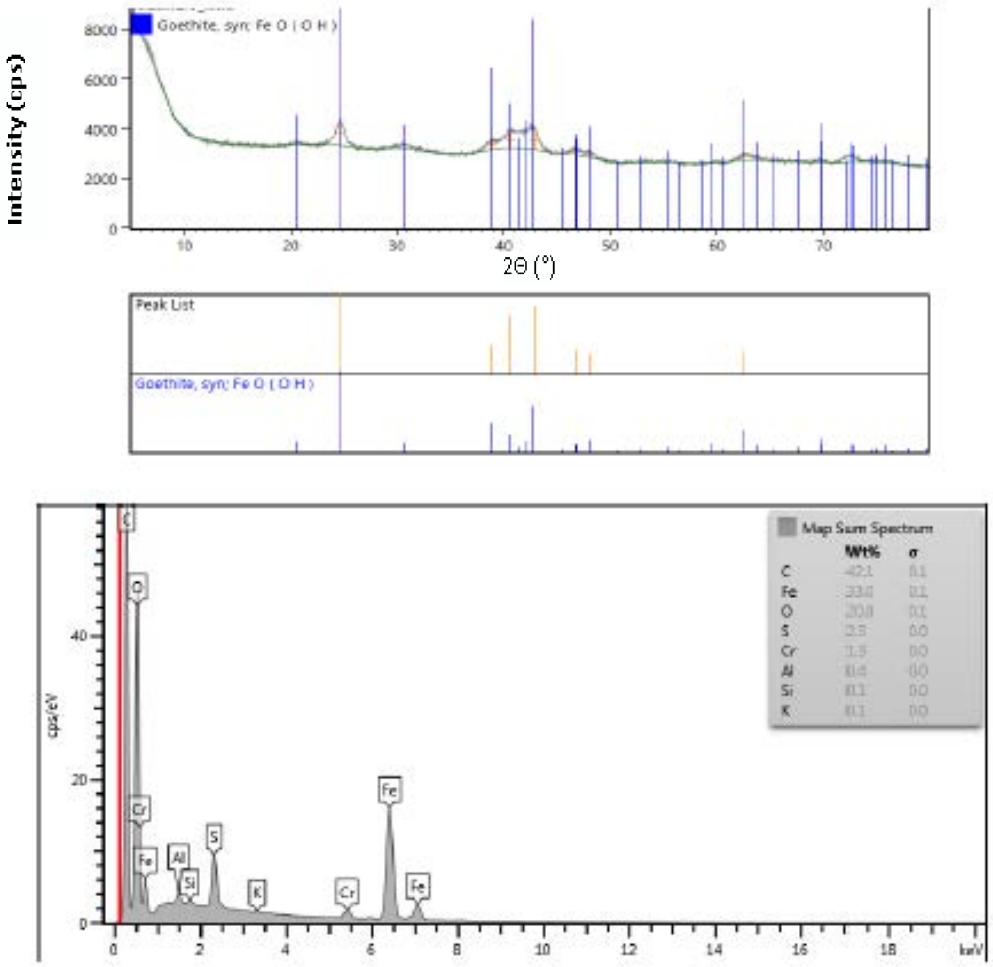

Figure 6.15: X-ray diffraction (XRD) patterns and diffractogram for the Cr-PDFe/Al nanocomposite.

As compared to the raw material which depicted FeO(OH) as the dominant species, no significant change is observed on the Cr-reacted material. Though the material is a bit amorphous, Al and Cr were detected even after Cr(VI) adsorption.

6.5.3 Compound composition

X-ray fluorescence (XRF) was used to determine the compound composition of PDFe/Al nanocomposite after adsorption is shown in Table 15.

Table 15: Compound composition of PDFe/Al nanocomposite after adsorption

	SARM49			
Compound	**Certified**	**Analysed**	**PDFe/Al**	**Cr-PDFe/Al**
SiO_2	**99.6**	99.70	0.16	0.17
TiO_2	**0.01**	0.00	*<0,01*	*<0,01*
Al_2O_3	**0.05**	0.01	1.15	0.67
Fe_2O_3	**0.05**	0.01	58.80	66.20
MnO	**0.01**	0.00	0.05	0.03
MgO	**0.05**	0.01	0.23	*<0,01*
CaO	**0.01**	0.01	0.17	*<0,01*
Na_2O	**0.05**	0.02	0.38	*<0,01*
K_2O	**0.01**	0.01	*<0,01*	*<0,01*
P_2O_5	**0**	0.03	*<0,01*	*<0,01*
Cr_2O_3	**0**	0.00	*<0,01*	0.13
NiO	**0**	0.01	*<0,01*	0.02
ZrO_2	**0**	0.01	*<0,01*	*<0,01*
SO_3	**0**	0.00	0.38	0.12
WO_3	**0**	0.00	0.03	0.11
CuO	**0**	0.00	*<0,01*	*<0,01*
Co_3O_4	**0**	0.00	0.03	0.10
SrO	**0**	0.00	*<0,01*	*<0,01*
LOI	**0**	0.10	38.60	32.50
Total	**100**	**99.94**	**99.98**	**100.05**

Table 15 shows the compound composition of PDFe/Al nanocomposite before and after Cr(VI) adsorption. As shown in table 14, Fe is the most dominant species in the synthesised PDFe/Al nanocomposite, followed by Al. Silica and SO_3 are impurities which precipitated from AMD. Post reacting with chromium, the concentration of chromium was detected in the nanocomposite.

6.5.4 Morphology

Scanning Electron Micrographs (SEM-EDX) was used to determine the morphology of PDFe/Al nanocomposite after Cr-adsorption is shown in Figure 6.16.

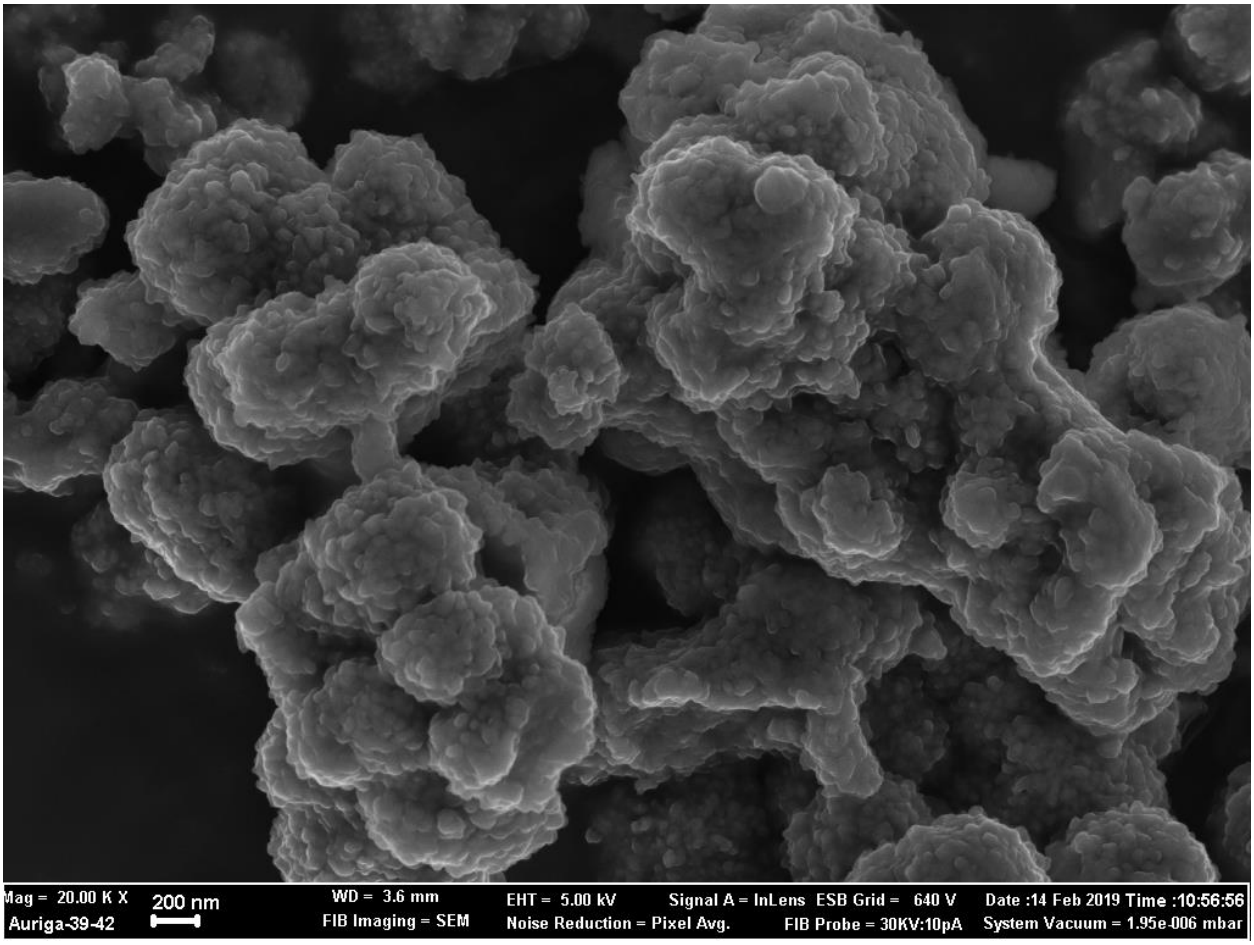

Figure 6.16: SEM images for Cr-reacted PDFe/Al nanocomposite

Figure 6.16 shows the visual structure of PDFe/Al nanocomposite after Cr(VI) adsorption. After contacting Cr(VI), the material possess flower-like structures with bright shading. The light structures could be chromium adsorbed by PDFe/Al nanocomposite as a result of varying electron penetrability (Mthombeni et al., 2018)

6.5.5 EDX Mapping

The mapping of Cr(VI)-reacted PDFe/Al nanocomposite was done to determine the relative distribution of elements on the adsorbent surface as show in Figure 6.17.

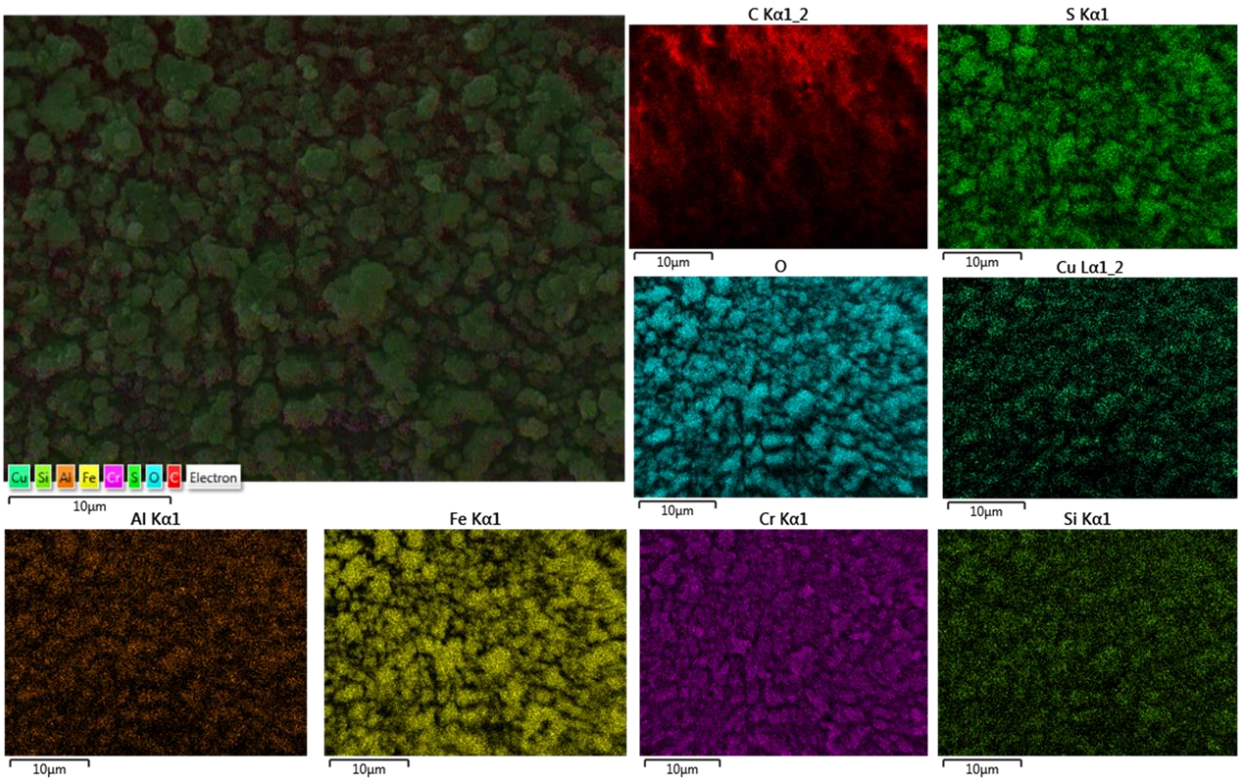

Figure 6.17: Mapping of Cr-PDFe/Al nanocomposite

Figure 6.17 shows elements present in the Cr-reacted nanocomposite. The presence of Cr proves the adsorption of chromium by the adsorbent. The presence of O is due to the material containing oxygen. Si and S are some of the impurities from AMD. The presence of Cu in the material is due to the material coating during analysis.

6.5.6 Thermal analysis

Thermo Gravimetric Analyser (TGA) was used to evaluate the thermal stability of PDFe/Al nanocomposite after adsorption. Figure 6.18 shows the thermal stability of the adsorbent after adsorption.

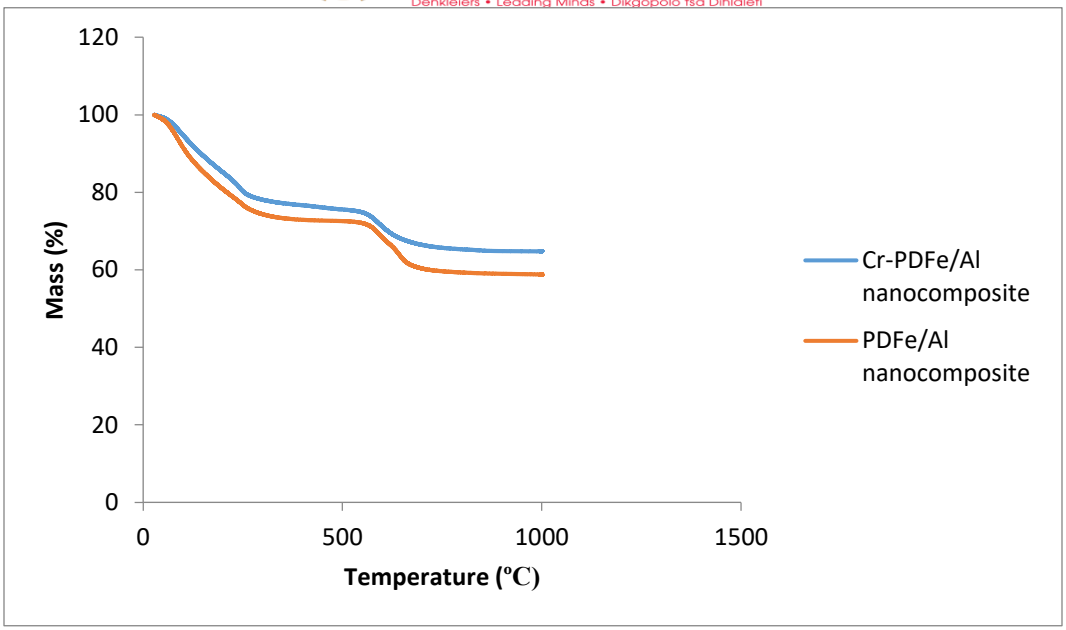

Figure 6.18: Thermal stability of PDFe/Al nanocomposite after Cr(VI)-adsorption

Figure 6.18 shows thermal stability plots of PDFe/Al nanocomposite after reacting with Cr. Cr-reacted plot appears in similar stability. The first decomposition phases for the plot could be an indication of the decrease in mass after 28 ºC due to the loss of moisture. The steep mass decrease of mass for Cr-reacted nanocomposite could be due to the loss of oxygen as carbon dioxide which contributed to the structure of chromate (CrO_4^{2-}). The declining trends indicate decomposition of the both materials. Both plots showed degradation from 28 to 1000 °C (Liu et al., 2016).

6.5.7 Surface area and porosity

Brunauer-Emmet-Teller (BET) was used to characterise for surface area, pore size and pore volume of PDFe/Al nanocomposite after adsorption as summarised in Table 16.

Table 16: BET characterisation of PDFe/Al nanocomposite after adsorption of Cr(VI)

Sample	BET surface area (m^2/g)	Pore volume (cm^3/g)	Pore size (nm)
PDFe/Al nanocomposite	24.6275	0.042334	8.58545
Cr-PDFe/Al nanocomposite	58.4070	0.067933	4.65237

Table 16 shows that there is a significant and clear increase in the surface area of PDFe/Al nanocomposite of after adsorption if Cr(VI). This is because when Cr(VI) attaches to the amorphous surface of PDFe/Al nanocomposite, it creates a rough surface texture as chromium is metallic and crystalline, hence producing a product (adsorbent – adsorbate) with a higher surface area. The synthesised PDFe/Al nanocomposite has pore size of 4.65237 nm which can be proof that the material is a mesoporous nanocomposite material as its pore size falls within the range of 2 – 50 nm (IUPAC, 1997).

6.6 Regeneration and reusability study

Regeneration/desorption study was done in order to evaluate the probability of recovering the used PDFe/Al nanocomposite. Figure 6.19 shows the % removal of Cr(VI) from the adsorbent (PDFe/Al nanocomposite).

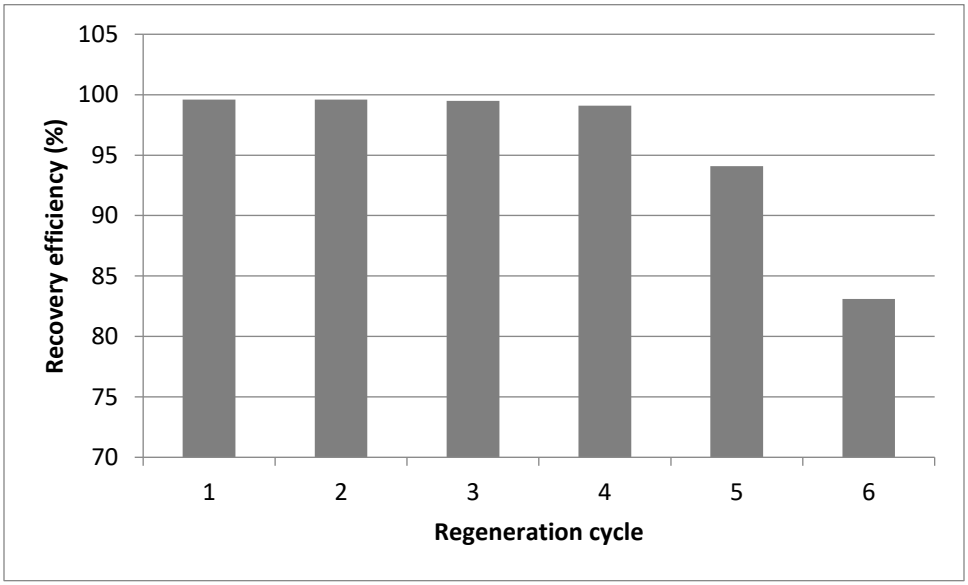

Figure 6.19: Recovery efficiency of PDFe/Al nanocomposite

From figure 6.19, it can be seen how the adsorbent is recovered throughout the first four (4) regeneration cycles. At the 5th cycle, there was significant decrease in the regeneration of the material. The decrease in the adsorption of hexavalent chromium could have been due to the destruction of the structure of the adsorbent which could no longer hold the pollutant, hence affecting its efficiency. In addition, the decrease in the recovery of the adsorbent (PDFe/Al nanocomposite) could have been due to the strong ionic bond between oxygen (from chromate)

and metal (iron/aluminium) which still binds them together, thus making it difficult to separate the atoms.

References

ENNIYA, I., RGHIOUI, L. & JOURANI, A. 2018. Adsorption of hexavalent chromium in aqueous solution on activated carbon prepared from apple peels. *Sustainable Chemistry and Pharmacy,* 7**,** 9-16.

GAFFER, A., AL KAHLAWY, A. A. & AMAN, D. 2017. Magnetic zeolite-natural polymer composite for adsorption of chromium (VI). *Egyptian Journal of Petroleum,* 26**,** 995-999.

GALLIOS, G. P. & VACLAVIKOVA, M. 2008. Removal of chromium (VI) from water streams: a thermodynamic study. *Environmental Chemistry Letters,* 6**,** 235-240.

GÜRÜ, M., VENEDIK, D. & MURATHAN, A. 2008. Removal of trivalent chromium from water using low-cost natural diatomite. *Journal of Hazardous Materials,* 160**,** 318-323.

HU, C.-Y., LO, S.-L., LIOU, Y.-H., HSU, Y.-W., SHIH, K. & LIN, C.-J. 2010. Hexavalent chromium removal from near natural water by copper–iron bimetallic particles. *Water Research,* 44**,** 3101-3108.

IUPAC. 1997. *Compendium of Chemical Terminology, 2nd ed.* [Online]. Oxford: Blackwell Scientific Publications. Available: http://goldbook.iupac.org [Accessed 2018-03-19].

LIU, Y. 2008. New insights into pseudo-second-order kinetic equation for adsorption. *Colloids and Surfaces A: Physicochemical and Engineering Aspects,* 320**,** 275-278.

LIU, Y., WANG, J.-S., ZHU, P., ZHAO, J.-C., ZHANG, C.-J., GUO, Y. & CUI, L. 2016. Thermal degradation properties of biobased iron alginate film. *Journal of Analytical and Applied Pyrolysis,* 119**,** 87-96.

MTHOMBENI, N. H., MBAKOP, S., RAY, S. C., LESWIFI, T., OCHIENG, A. & ONYANGO, M. S. 2018. Highly efficient removal of chromium (VI) through adsorption and reduction: A column dynamic study using magnetized natural zeolite-polypyrrole composite. *Journal of Environmental Chemical Engineering,* 6**,** 4008-4017.

TARUN KUMAR NAIYA, BISWAJIT SINGHA & DAS, S. K. 2011. FTIR Study for the Cr(VI) Removal from Aqueous Solution Using Rice Waste. *International Conference on Chemistry and Chemical Process.* Singapore: IPCBEE.

YANG, J., YU, M. & CHEN, W. 2015. Adsorption of hexavalent chromium from aqueous solution by activated carbon prepared from longan seed: Kinetics, equilibrium and thermodynamics. *Journal of Industrial and Engineering Chemistry,* 21**,** 414-422.

ZHANG, S., NIU, H., CAI, Y., ZHAO, X. & SHI, Y. 2010. Arsenite and arsenate adsorption on coprecipitated bimetal oxide magnetic nanomaterials: MnFe2O4 and CoFe2O4. *Chemical Engineering Journal,* 158**,** 599-607.

ZHANG, W., ZHANG, S., WANG, J., WANG, M., HE, Q., SONG, J., WANG, H. & ZHOU, J. 2018. Hybrid functionalized chitosan-Al2O3@SiO2 composite for enhanced Cr(VI) adsorption. *Chemosphere,* 203**,** 188-198.

CHAPTER SEVEN

CONGO RED DYE ADSORPTION STUDY: RESULTS AND DISCUSSION

7.0 Introduction

This chapter focuses on the evaluation of the efficiency of recovered and synthesised poly-cationic dimetallic Fe/Al nanocomposite on the removal of Congo Red dye (CR) from industrial effluents: Evaluation of adsorption kinetics, reaction equilibrium and mechanisms.

7.1 Optimization of adsorption parameters

7.1.1 Effect of initial concentration

The effect of initial concentrations of CR on the adsorption onto PDFe/Al nanocomposite is shown in Figure 7.1, where the relationship between final concentration and the studied initial concentrations is illustrated.

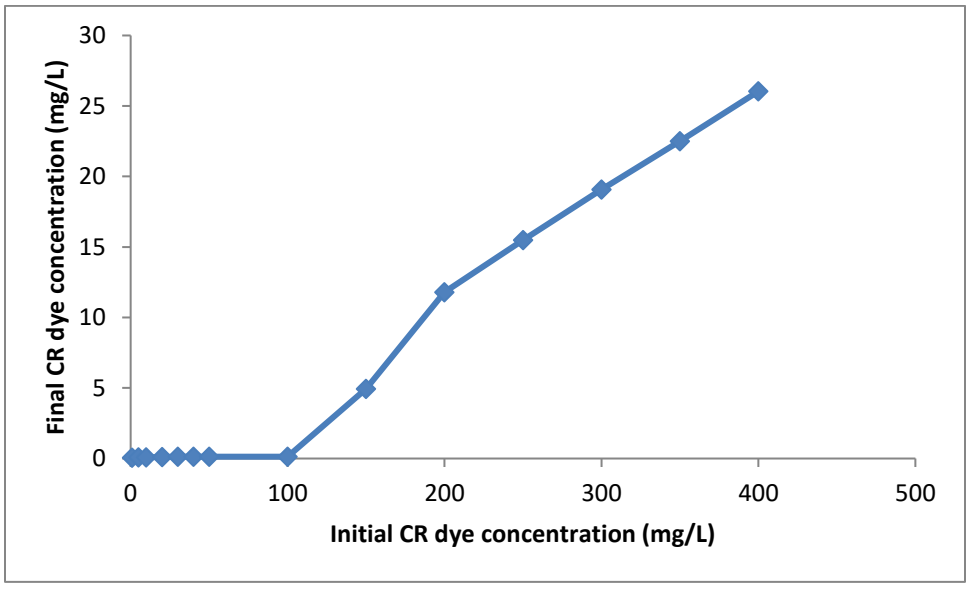

Figure 7.1: Effect of initial concentration on the removal of CR

As shown in figure 7.1, an effective removal of CR by the PDFe/Al nanocomposite was observed concentrations up to 100 mg/L. After 100 mg/L, a rapid increase in the residual

concentration is observed, thus indicating super saturation of the adsorbent. Therefore, it can be concluded that 100 mg/L is the optimum concentration of CR solution for adsorption of Congo red dye.

7.1.2 Effect of adsorbent dosage

The effect of PDFe/Al nanocomposite dosage on the adsorption of CR is shown in Figure 7.2, where the relationship between % removal and the dosage is illustrated.

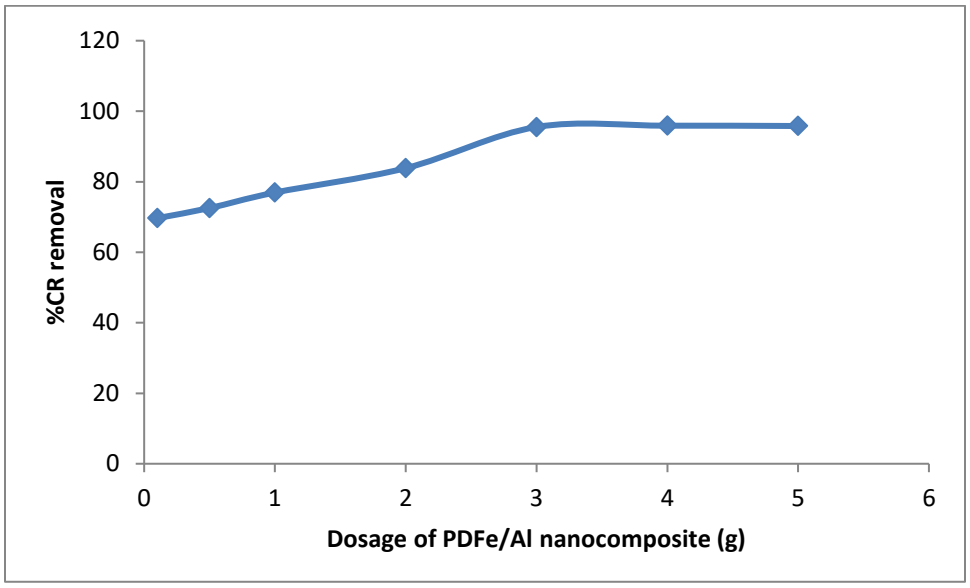

Figure 7.2: Effect of PDFe/Al nanocomposite dosage on the % removal of CR from water

Figure 7.3 illustrates the relationship between dosage and adsorption capacity

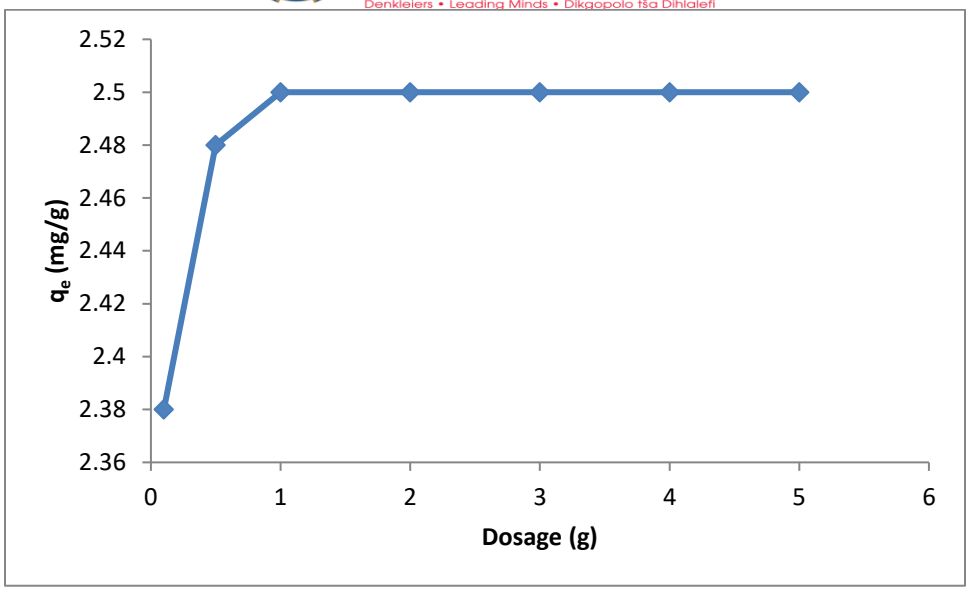

Figure 7.3: Relationship between the adsorption capacity (q_e) and the dosage of PDFe/Al nanocomposite

From figure 7.3, a stable equilibrium removal of CR from water is observed after 1.0 g. This shows a great efficiency of the synthesised adsorbent (PTFe/Al nanocomposite). The gentle slope shows saturation of the adsorbent by CR, hence cannot take more of the dye. A dosage of 1.0 g was observed to be optimum for this study.

7.1.3 Effect of initial pH

The effect of solution initial pH on the adsorption of CR is shown in Figure 7.4, where the relationship between % removal and initial pH is illustrated.

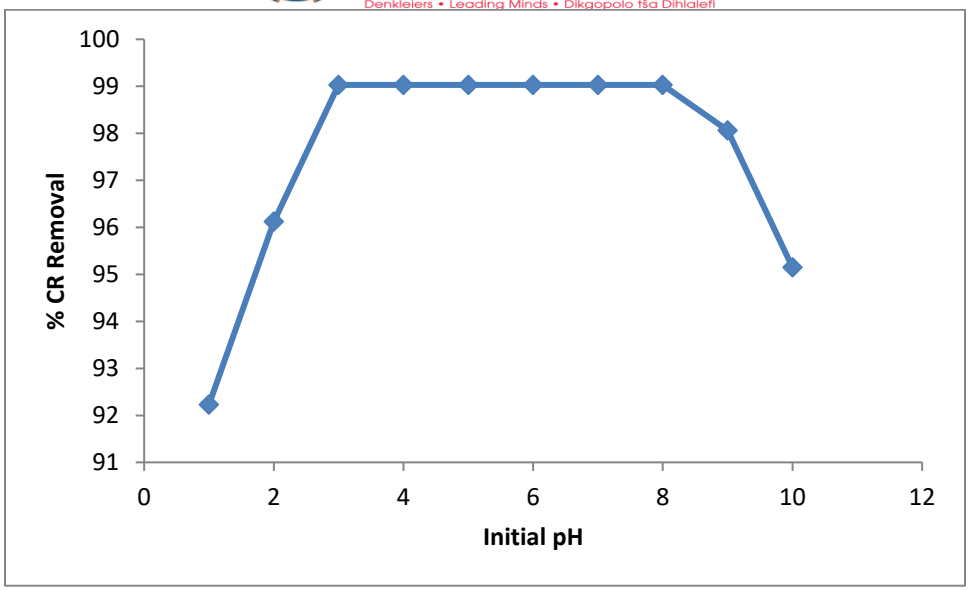

Figure 7.4: Effect of initial solution pH on the removal of CR

Figure 7.4 shows that a lot of CR ions were removed from water within pH of 3 – 8. This corroborates the value of point of zero charge of the adsorbent which was found to be pH_{PZC} = 3.02, which is also within the pH range 3 – 4 at which the adsorbent was synthesised.

7.1.4 Effect of agitation time

The effect of agitation time on the adsorption of CR is shown in figure 7.5, where the relationship between % removal and agitation time is illustrated.

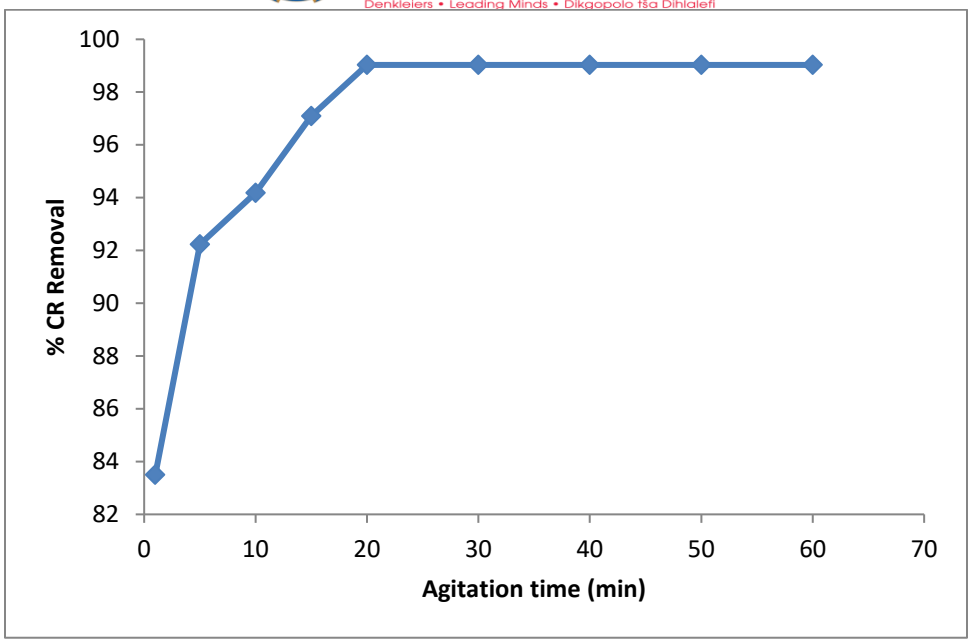

Figure 7.5: Effect of agitation time on the % removal of CR from water

Figure 7.5 shows the removal of CR from water, where a stable removal of the dye is observed between 20 – 60 minutes of agitation i.e. there is no change in the percentage removal of CR after 20 minutes. This can be an indication that 20 minutes is the optimum time for removal of CR in this study.

7.1.5 Effect of temperature

The effect of temperature on the adsorption of CR is shown in figure 7.6, where the relationship between % removal and temperature is illustrated.

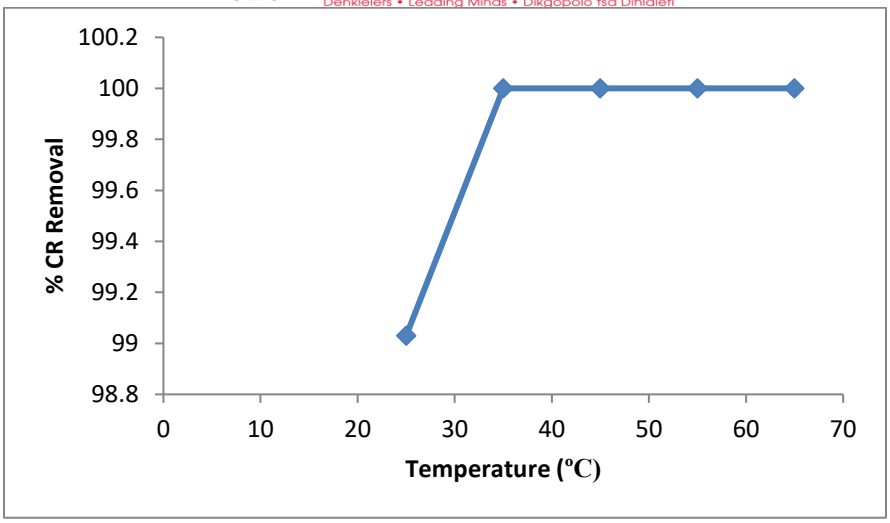

Figure 7.6: Effect of temperature on the removal of CR from water

From figure 7.6, it can be noted that the percentage removal of CR from water using PTFe/Al increases as temperature increases. After 35 ºC, complete removal of CR is observed. This give an indication that 35 ºC is optimum for this study.

7.2 Adsorption kinetics

Adsorption kinetics for the current study was determined to study the mechanism and rates of adsorption by the PDFe/Al nanocomposite. Figures 7.7, 7.8 and 7.9 show the results.

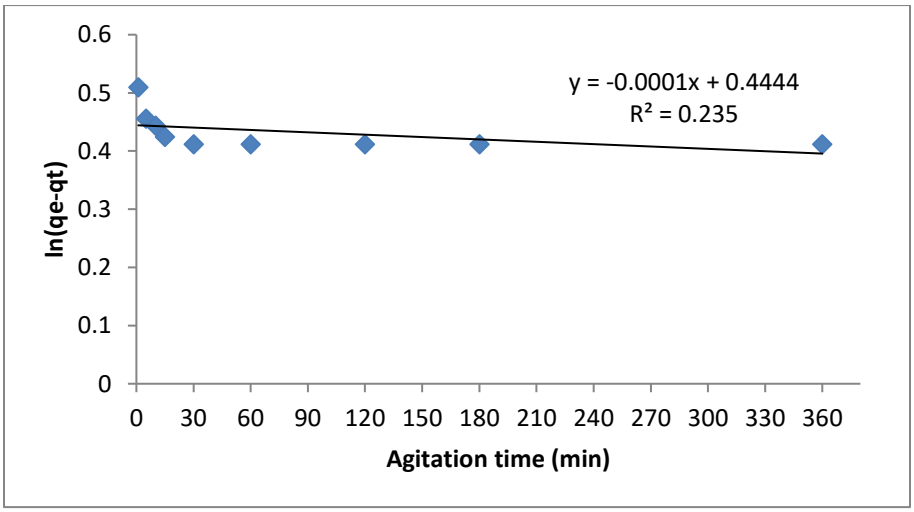

Figure 7.7: Pseudo-first-order graph: relationship between CR removal and time

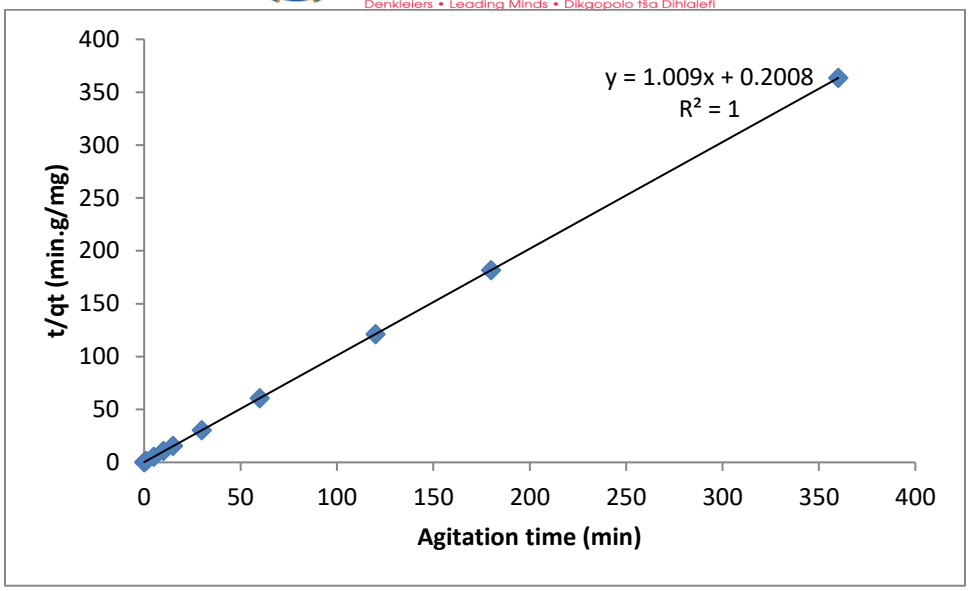

Figure 7.8: Pseudo-second order graph: relationship between CR removal and time

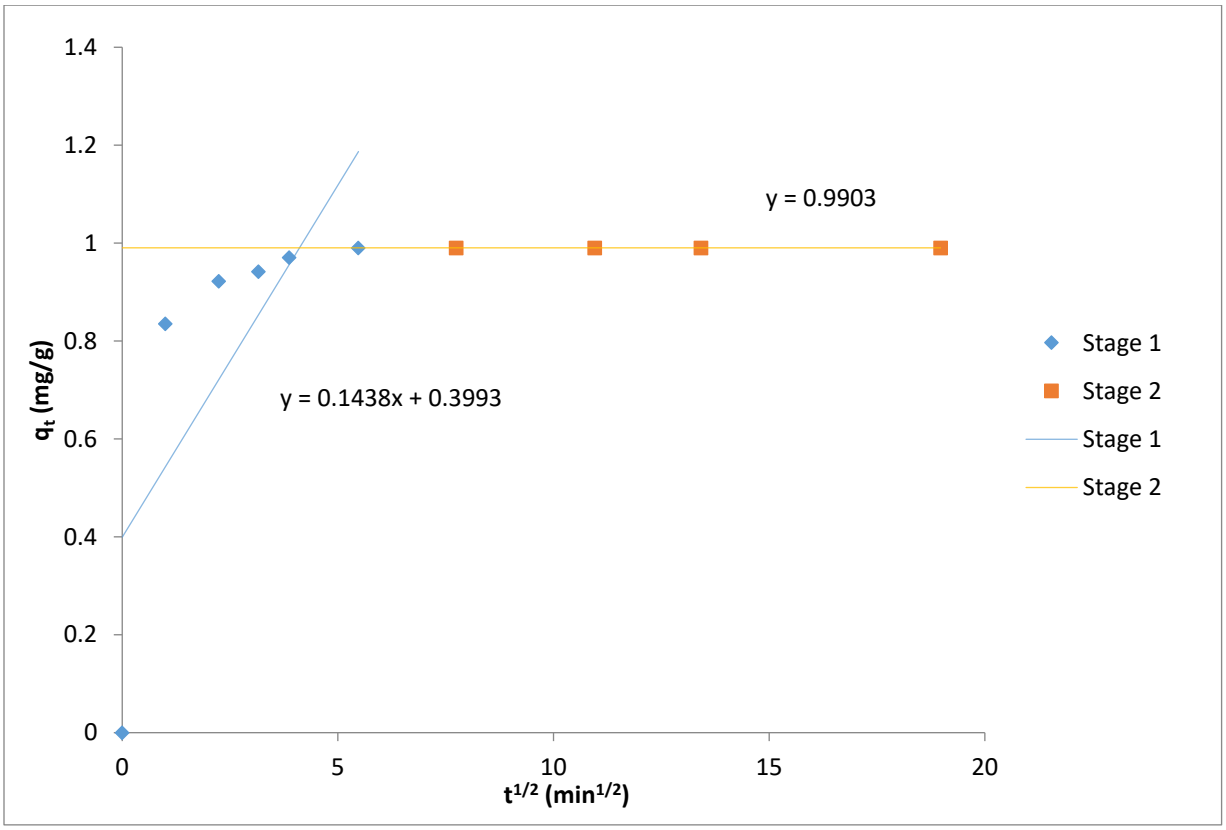

Figure 7.9: Intra-particle diffusion graph: relationship between CR removal and time

From figures 7.7, 7.8 and 7.9, the relationship between adsorption capacity and time is observed illustrating pseudo-first order, pseudo-second order and intra-particle diffusion, respectively. Experimental data best fitted pseudo-second order kinetics compared to pseudo-first order as the correlation coefficient is R^2 =1, which relates to the availability of adsorption sites on the adsorbent (Liu, 2008). From this study, it was observed that the removal of CR favoured the mechanism of chemisorption. Figure 7.9 illustrates the intra-particle diffusion, where during the first 1 minute; a very steeper region is observed indicating instant adsorption and then slower adsorption which could be due to CR molecules having to penetrate the adsorbent matrices. The second region is the equilibrium where further slowdown of the adsorption is observed due to saturation of the adsorbent.

7.3 Adsorption isotherms

Adsorption isotherms were evaluated for CR as illustrated in Figures 7.10 and 7.11.

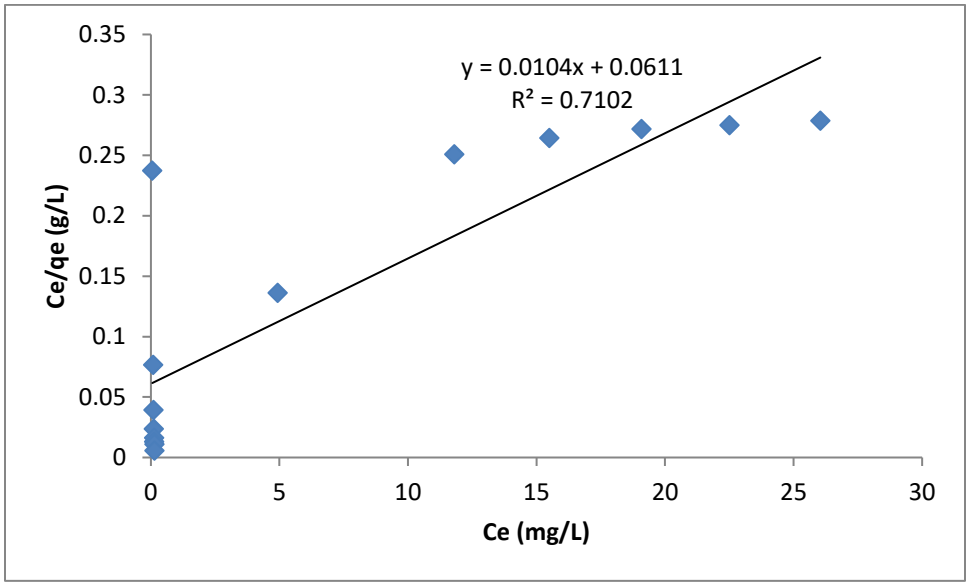

Figure 7.10: Langmuir adsorption isotherm: relationship between removal and initial concentration of CR

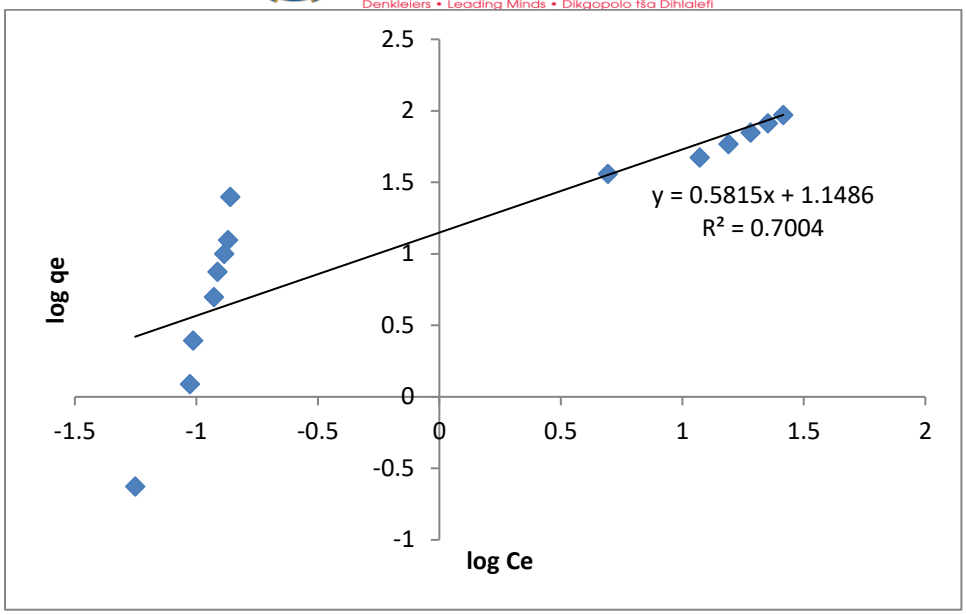

Figure 7.11: Freundlich adsorption isotherm: relationship between removal and initial concentration of CR

From figures 7.10 and 7.11, the relationship between the adsorption capacity of the adsorbent and equilibrium concentration of CR is depicted. From the plots, the data best fitted Langmuir-adsorption, which is based on the single layer adsorption of pollutant onto a homogeneous surface.

7.4 Thermodynamics

Equilibrium concentrations were observed to have reached zero for temperatures ≥ 35 ºC. The Gibbs free energy was negative based on the residual concentration obtained at 25ºC.

7.5 Characterisation of solid samples

7.5.1 Functional groups

Fourier Transform Infrared Spectrometer (FTIR) was used to determine the functional groups of PDFe/Al nanocomposite after adsorption and this was shown in Figure 7.12.

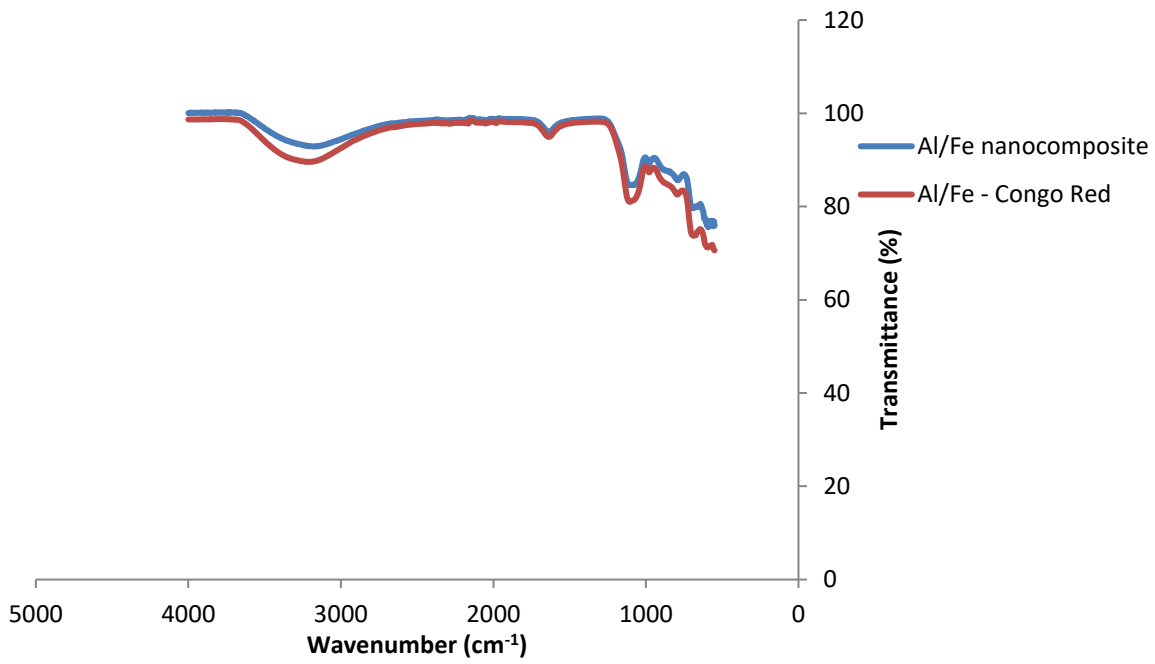

Figure 7.12: Functional groups of nanocomposite and CR-reacted nanocomposite.

From figure 7.12, bands of raw nanocomposite and CR-reacted nanocomposite are compared. A sharp peak is observed at 1134 cm^{-1} which could be an indication of Si-O-Si stretching (Masindi et al., 2017). The presence of silica in the material was demonstrated by XRD results. A small curve at 866 cm^{-1} could be an indication of sulphonate stretching present in CR (Kataria and Garg, 2017). The stretching or shift of –OH group band between 3740 and 2966 cm^{-1} is observed (Hu et al., 2018, Zhang et al., 2018a). These results confirm the adsorption of CR by PDFe/Al nanocomposite.

7.5.2 Mineralogical composition

X-ray diffraction (XRD) patterns and diffractogram for the CR-PDFe/Al nanocomposite is shown in Figure 7.13.

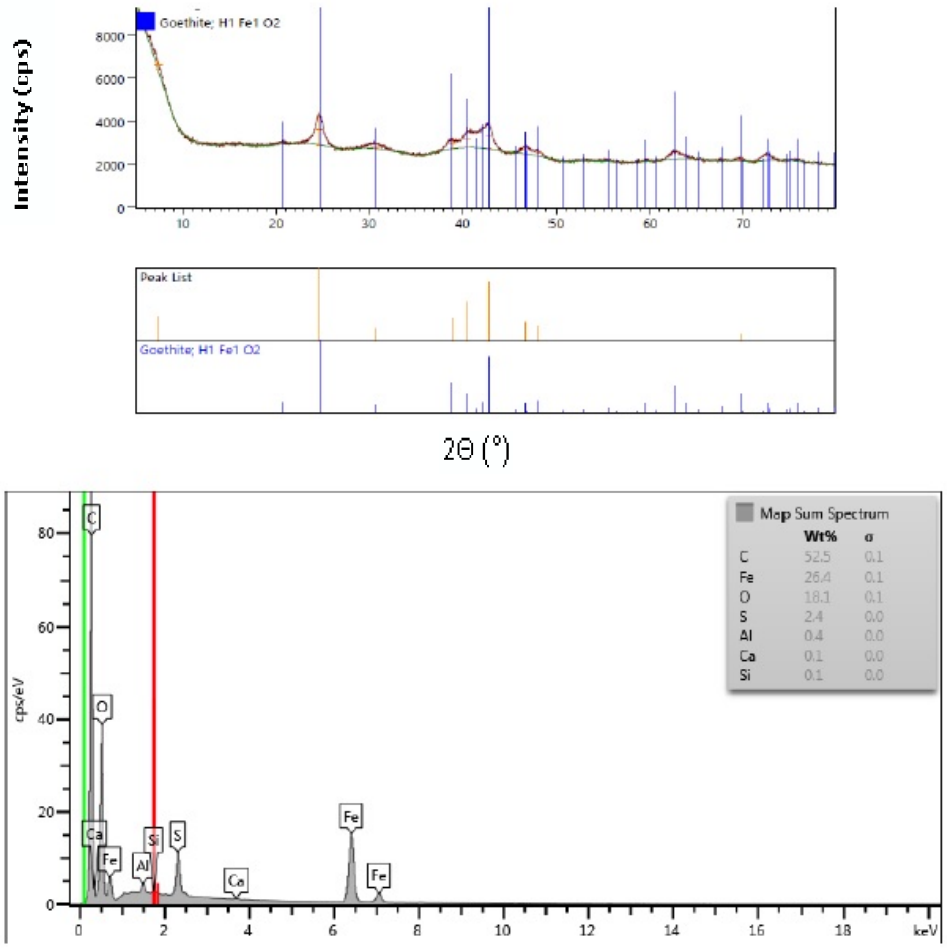

Figure 7.13: X-ray diffraction (XRD) patterns and diffractogram for the CR-PDFe/Al nanocomposite.

As compared to the raw material which depicted FeO(OH) as the dominant species, the CR-reacted material is observed to have elevated concentration of sulphur (S). This could be due to the presence of sulfonate group which is present in Congo red dye. The presence of SO_3 is also shown by XRF results in table 17.

7.5.3 Compound composition

X-ray fluorescence (XRF) was used to determine the compound composition of PDFe/Al nanocomposite after adsorption is shown in Table 17.

Table 17: Compound composition of PDFe/Al nanocomposite after adsorption

	SARM49			
	Certified	**Analysed**	**Raw PDFe/Al**	**CR-PDFe/Al**
SiO_2	**99.6**	99.70	0.16	0.24
TiO_2	**0.01**	0.00	*<0,01*	0.39
Al_2O_3	**0.05**	0.01	1.15	1.38
Fe_2O_3	**0.05**	0.01	58.80	61.80
MnO	**0.01**	0.00	0.05	0.07
MgO	**0.05**	0.01	0.23	*<0,01*
CaO	**0.01**	0.01	0.17	0.02
Na_2O	**0.05**	0.02	0.38	*<0,01*
K_2O	**0.01**	0.01	*<0,01*	*<0,01*
P_2O_5	**0**	0.03	*<0,01*	*<0,01*
Cr_2O_3	**0**	0.00	*<0,01*	*<0,01*
NiO	**0**	0.01	*<0,01*	*<0,01*
ZrO_2	**0**	0.01	*<0,01*	*<0,01*
SO_3	**0**	0.00	0.38	0.06
WO_3	**0**	0.00	0.03	0.08
CuO	**0**	0.00	*<0,01*	*<0,01*
Co_3O_4	**0**	0.00	0.03	0.09
SrO	**0**	0.00	*<0,01*	*<0,01*
LOI	**0**	0.10	38.60	35.90
Total	**100**	**99.94**	**99.98**	**100.02**

Table 17 shows the compound composition of PDFe/Al nanocomposite before and after CR adsorption. As shown in table 4, Fe is the most dominant species in the synthesised PDFe/Al nanocomposite, followed by Al. Silica and SO_3 are impurities which precipitated from AMD.

Post contact with CR, the concentration of Fe_2O_3 and Al_2O_3 increased, this could be due to possible ion exchange with CR.

7.5.4 Morphology

Scanning Electron Micrographs (SEM-EDX) was used to determine the morphology of PDFe/Al nanocomposite after CR-adsorption is shown in Figure 7.14.

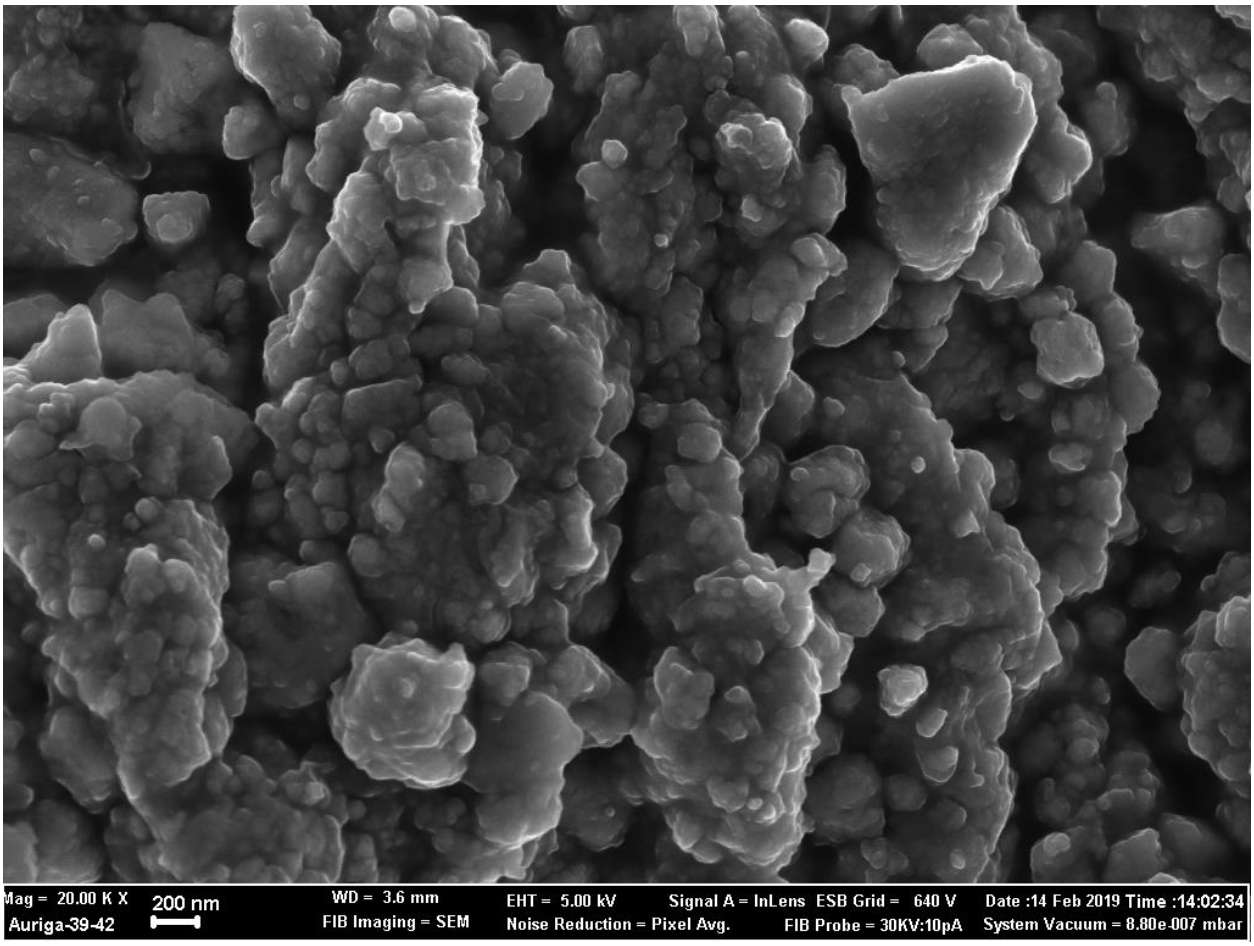

Figure 7.14: SEM images for CR-reacted PDFe/Al nanocomposite

As shown in Figure 7.14, the morphology of synthesised PDFe/Al nanocomposite and CR-reacted PDFe/Al nanocomposite was investigated. After contacting CR-rich water, the morphology changed to spherical structures connecting together, which could be indication of adsorption of CR by the material.

7.5.5 EDX Mapping

The mapping of CR-reacted PDFe/Al nanocomposite was done to determine the relative distribution of elements on the adsorbent surface as show in Figure 7.15.

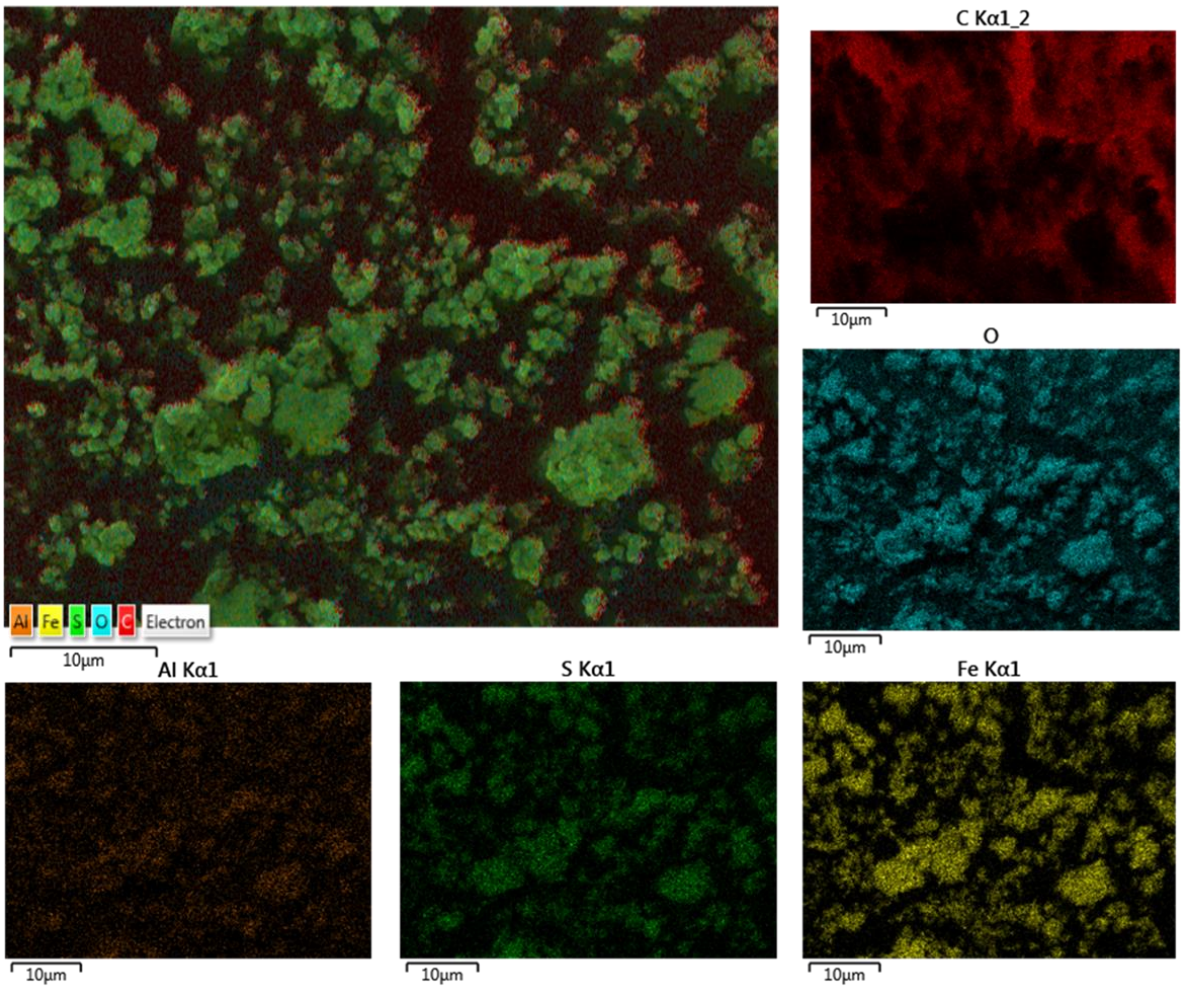

Figure 7.15: Mapping of CR-PDFe/Al nanocomposite

As shown in Figure 7.15, the synthesised PDFe/Al nanocomposite was observed to contain C, Fe, O, Al, Sulphur and Ca. The dominating element is shown to be Sulphur, and this is due to its presence in CR. Carbon is also revealed to be in significant concentration due to its high concentration in CR. The amount of sulphur increased due to its presence in CR.

7.5.6 Thermal analysis

Thermo Gravimetric Analyser (TGA) was used to evaluate the thermal stability of PDFe/Al nanocomposite after adsorption. Figure 7.16 shows the thermal stability of the adsorbent after adsorption.

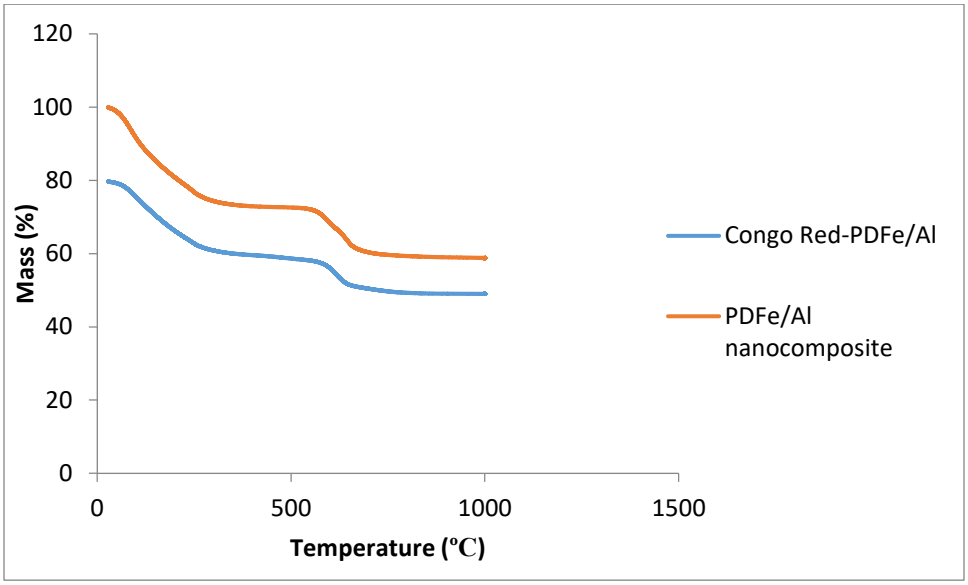

Figure 7.16: Thermal stability of PDFe/Al nanocomposite after CR-adsorption

From figure 7.16, the thermal stability of PDFe/Al nanocomposite before and after CR adsorption is observed. There is a descending steep slope between 40 - 250 ºC which indicates the decrease in mass percentage of raw and CR-reacted nanocomposite due to temperature. The loss in mass percentage is an indication that moisture is lost from the materials. The slope becomes gentle towards 600 ºC, after which the graph drops, which could indicate further removal of water from the materials.

7.5.7 Surface area and porosity

Brunauer-Emmet-Teller (BET) was used to characterise for surface area, pore size and pore volume of PDFe/Al nanocomposite after adsorption. Table 18 provides a summary of the characteristics.

Table 18: BET characterisation of PDFe/Al nanocomposite after adsorption of CR

Sample	BET surface area (m^2/g)	Pore volume (cm^3/g)	Pore size (nm)
PDFe/Al nanocomposite	24.6275	0.042334	8.58545
CR – reacted PDFe/Al	29.5432	0.046754	6.76554

Table 18 shows that there is an increase in the surface area of PDFe/Al nanocomposite after adsorption of CR. The synthesised PDFe/Al nanocomposite has a pore size of 4.65237 nm, hence a mesoporous nanocomposite. After CR-adsorption, the surface area increases and this corroborates the XRF results which showed an increase in the amounts of Fe_2O_3 and Al_2O_3 due to adsorption of oxygen molecules on the matrices of the adsorbent.

7.6 Regeneration and reusability study

Regeneration/desorption study was done in order to evaluate the probability of recovering the used PDFe/Al nanocomposite. Figure 7.17 shows the % removal of CR from the adsorbent (PDFe/Al nanocomposite).

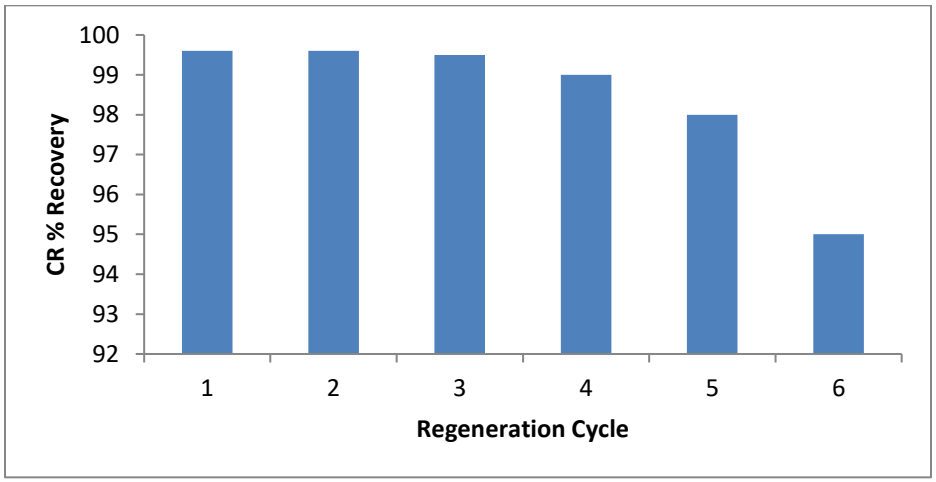

Figure 7.17: Recovery efficiency of PDFe/Al nanocomposite from CR-reacted nanocomposite

From figure 7.17, it can be seen how the adsorbent is recovered throughout the first three (3) regeneration cycles. A clear decrease in the recovery of PDFe/Al nanocomposite at cycles 4, 5 and 6 is observed. The decrease in the recovery efficiency could be due to the depletion of cationic species (Fe^{3+}/Al^{3+}) and/or OH^- in the inter layers of PDFe/Al since an acid is used for the desorption process.

References

HU, M., YAN, X., HU, X., ZHANG, J., FENG, R. & ZHOU, M. 2018. Ultra-high adsorption capacity of MgO/SiO2 composites with rough surfaces for Congo red removal from water. *Journal of Colloid and Interface Science,* 510**,** 111-117.

KATARIA, N. & GARG, V. K. 2017. Removal of Congo red and Brilliant green dyes from aqueous solution using flower shaped ZnO nanoparticles. *Journal of Environmental Chemical Engineering,* 5**,** 5420-5428.

LIU, Y. 2008. New insights into pseudo-second-order kinetic equation for adsorption. *Colloids and Surfaces A: Physicochemical and Engineering Aspects,* 320**,** 275-278.

MASINDI, V., GITARI, M. W., TUTU, H. & DEBEER, M. 2017. Synthesis of cryptocrystalline magnesite–bentonite clay composite and its application for neutralization and attenuation of inorganic contaminants in acidic and metalliferous mine drainage. *Journal of Water Process Engineering,* 15**,** 2-17.

ZHANG, J., YAN, X., HU, M., HU, X. & ZHOU, M. 2018. Adsorption of Congo red from aqueous solution using ZnO-modified SiO2 nanospheres with rough surfaces. *Journal of Molecular Liquids,* 249**,** 772-778.

CHAPTER EIGHT

CONCLUSIONS AND RECOMMENDATION

The synthesis of polycationic dimetal iron/aluminium nanocomposite (PDFe/Al nanocomposite) was executed through fractional precipitation followed by and processed through calcination and vibratory ball milling. The material was successfully recovered and synthesised with outstanding properties. PDFe/Al nanocomposite was observed to have possessed a surface area of 24.6275 m^2/g, pore size of 8.58545 nm and pore volume of 0.042334 cm^3/g. The efficiency of the material was tested through adsorption of arsenic (As(V)), chromium (Cr(VI)) and Congo red dye (CR) on a batch experimental set-up. Parameters optimised include: agitation time, adsorbent dosage, temperature, pH, and initial adsorbate concentration.

Experimental results revealed that optimum conditions that are suitable for the removal of As(V) from an aqueous system are: 150 mg/L of As(V) concentration, 1 g adsorbent and 60 min equilibration time, where an adsorption capacity of $q_e = 105\ mg/g$ was observed with >99% As(V) removal. As(V) removal was independent of pH and temperature.

Cr(VI) was effectively removed at 50 mg/L initial Cr(VI) concentration, 3 g nanocomposite dosage, initial pH = 3 of solution, 180 min equilibration time and temperature = 45 ºC, where an adsorption capacity of $q_e = 4.166\ mg/g$ was observed with >95% Cr(VI) removal.

Optimum conditions for removal for CR adsorption are: 100 mg/L initial CR concentration; 0.5 g PDFe/Al nanocomposite; 20 minutes agitation time; 3 – 8 initial CR pH; and temperature of 35 ºC, where an adsorption capacity of $q_e = 25\ mg/g$ was observed with >99% Cr(VI) removal.

Adsorption kinetics followed the pseudo-second-order as opposed to pseudo-first-order behaviour, therefore confirming chemisorption for all chemical species. Regeneration study of the material showed that the adsorbent can be reused more than four times on the adsorption of As(V), Cr(VI) and CR.

This study demonstrated that valorisation of waste material by recovering valuable di-metals and employing them to curtail the impact of problematic pollutants is feasible. As such, this double-

edged study demonstrated the exceptional potential of the synthesised material to remove As(V), Cr(VI) and CR from aqueous system.

This study recommends the use of materials recovered from natural AMD due to their composition and ability to work effectively. Moreover, this would reduce cost spent on purchasing synthetic materials or adsorbents.